A new Approach to Aerodynamic Performance of Aircraft under Turbulent Atmospheric Conditions

Vom Fachbereich Maschinenbau
an der Technischen Universität Darmstadt
zur
Erlangung des Grades eines Doktor-Ingenieurs (Dr.-Ing.)
genehmigte

D i s s e r t a t i o n

vorgelegt von

Dipl.-Ing. Michael Weismüller

aus Limburg

Berichterstatter:	Prof. Dr.-Ing. C. Tropea
Mitberichterstatter:	Prof. Dr.-Ing. R. Radespiel
Tag der Einreichung:	26.04.2011
Tag der mündlichen Prüfung:	15.06.2011

Darmstadt 2012
D17

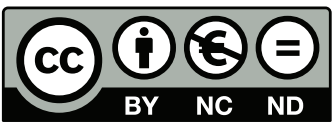

Hiermit versichere ich, die vorliegende Doktorarbeit unter der Betreuung von Prof. Dr.-Ing. C. Tropea nur mit den angegebenen Hilfsmitteln selbständig angefertigt zu haben.

Darmstadt, den 26.04.2011

Preface

The present study was prepared during my employment as a doctoral researcher at the Institute of Fluid Mechanics and Aerodynamics of the Technische Universität Darmstadt.

First of all I want to thank my doctoral adviser Prof. Dr.-Ing. C. Tropea. He provided the opportunity to work in the fascinating environment of in-flight experiments. The unique infrastructure and scientific environment provided by Prof. Tropea, along with the support he provided in me over the years greatly helped to further develop myself.

I would also like to thank Prof. Dr.-Ing. R. Radespiel for his ongoing interest in my work and for reviewing this thesis.

The financial support from the Deutsche Forschungsgemeinschaft (German Research Foundation) under contract TR 194/48-1 is gratefully acknowledged.

I want to thank my colleagues Andreas Reeh, Alexander Duchmann, Andreas Güttler and Martin Stenger for their extraordinary dedication helping me to build the wing glove and the measurement system as well as their ongoing support.

I am truly thankful to the students Vasco Arnold, Katrin Barckmann, Otto Böpple, Christoph Dienel, Wilm Friedrichs, Felix Loosmann, Simon Miller and Jonas Schulze who added fundamental contributions to every section of my research. Without exception they dedicated themselves fully to their task and I believe they enjoyed it at least a bit.

No experimental research can be conducted successfully without a cooperative and helpful machine shop. Therefore I want to thank Ilona Kaufhold and her team of machinists who always helped in a spontaneous and friendly manner. I am truly thankful to Tim Geelhaar for his support to manufacture the mold for the wing glove.

Last but not least I want to express my gratefulness to my family for the ongoing support over the years. Without their appreciation and support of my education as well as flying activities, this work had not been possible.

Darmstadt, April 2011 Michael Weismüller

Abstract

In the present study the influence of atmospheric turbulence on aircraft performance has been investigated and a relation between flight physics and meteorology has been established. Special attention was paid on aircraft with natural laminar flow airfoils because they exhibit an additional possibility of performance loss due to increased drag caused by a premature laminar-turbulent transition.

A theoretical analysis was performed and the aerodynamic problem was extracted from the performance problem. A new wing glove for the G109b measurement aircraft as well as measurement equipment capable of detecting unsteady aerodynamic effects were developed. In-flight measurements for the validation of performance loss theories were carried out resulting in a new approach to aircraft performance under turbulent atmospheric conditions.

Generally, a loss of flight performance can be the result of decreased lift, increased drag or a combination of both. The aerodynamic state and therefore the possible influencing mechanisms of atmospheric turbulence vary with the flight condition. Based on aircraft performance considerations, three principal flight conditions were determined for an in-depth study of the aerodynamic state related to these flight conditions. The flight conditions are slow flight, best glide and cruise flight.

A new wing glove with favorable characteristics for aerodynamic in-flight experiments, retaining the flying qualities of the aircraft besides the asymmetric configuration, has been designed. A survey of the base flow on the glove in non-turbulent conditions by means of flight tests, wind tunnel tests and numerical simulations was conducted prior to the investigations under turbulent conditions. The results were essential as baseline data and showed that the numerous design requirements for the new wing glove were fulfilled.

The flight test results show that the assumption of steady inflow conditions is incorrect for flight in atmospheric turbulence. An elevated level of micro-scale turbulence in the atmosphere is related to increased angle of attack variations. Therefore, unsteady changes in the airfoil pressure distribution are prevalent when an elevated turbulence level is

encountered. Turbulence levels of 0.5% and more, which lead to different transition scenarios according to the results from flat plate experiments in transition research, do not occur in only light atmospheric turbulence, which is in turn the prerequisite for almost steady pressure distributions.

The unsteady lift variations related to the angle of attack variations due to gusts are well predicted by unsteady thin-airfoil theory. A quasi-stationary approach does not cover the entire unsteady lift effects but in the case of laminar airfoils it predicts when the laminar drag bucket is left and airfoil drag increases. Especially in slow flight very close to the upper limit of the laminar drag bucket, angle of attack variations lead to increased airfoil drag. Flying at a lower angle of attack simply solves this problem. Only a slight increase in velocity is required to lower that angle of attack sufficiently.

Kurzfassung

In der vorliegenden Arbeit wurde der Einfluss von atmosphärischer Turbulenz auf die Flugleistungen von Flugzeugen untersucht und ein Zusammenhang zwischen Flugphysik und Meteorologie hergestellt. Ein besonderes Augenmerk lag auf Flugzeugen mit Profilen mit natürlicher Laminarhaltung, weil bei diesen eine zusätzliche Möglichkeit des Flugleistungsverlusts besteht, nämlich ein erhöhter Widerstand durch einen vorzeitigen laminar-turbulenten Umschlag.

Eine theoretische Untersuchung wurde durchgeführt und das aerodynamische Problem aus dem Flugleistungsproblem extrahiert. Es wurde ein neuer Flügelhandschuh für das G109b Messflugzeug sowie eine Messanlage entwickelt, die in der Lage ist, auch instationäre aerodynamische Effekte zu erfassen. Zur Überprüfung von verschiedenen Theorien zum Flugleistungsverlust wurden Flugmessungen durchgeführt, aus denen ein neuer Ansatz zur Flugleistungsbetrachtung herrührt.

Grundsätzlich kann ein Flugleistungsverlust aufgrund eines verminderten Auftriebs, eines erhöhten Widerstands oder einer Kombination aus beidem entstehen. Der aerodynamische Grundzustand und damit die Einflussmöglichkeiten ändern sich mit dem Flugzustand. Die aerodynamischen Grundzustände für drei exemplarische Flugzustände wurden eingehend untersucht. Die Flugzustände sind Langsamflug, bestes Gleiten und Reiseflug.

Ein neuer Flügelhandschuh mit vorteilhaften Eigenschaften für aerodynamische Freiflugexperimente wurde entwickelt. Dabei musste die Beibehaltung der Flugeigenschaften trotz der asymmetrischen Flugzeugkonfiguration gewährleistet werden. Eine Untersuchung des Strömungszustandes wurde vor den Versuchen in atmosphärischer Turbulenz durchgeführt. Dafür wurden Flugversuche, Windkanalexperimente und numerische Simulationen durchgeführt. Diese Versuche stellten eine notwendige Datenbasis bereit und zeigten, dass die zahlreichen Anforderungen an den Handschuh erfüllt werden konnten.

Die Flugversuche zeigen, dass die Annahme von konstanten Anströmbedingungen im Flug durch atmosphärische Turbulenz nicht gerechtfertigt ist. Ein erhöhtes Turbulenzniveau im Bereich kleiner Skalen ist

immer mit Anstellwinkelschwankungen verbunden, was wiederum eine zeitlich nicht konstante Druckverteilung am Profil hervorruft. Turbulenzgrade von 0,5% und mehr, die laut Ergebnissen von Transitionsversuchen an ebenen Platten zu einer Veränderung des Transitionsmechanismus führen, treten nicht in nur leichter Turbulenz auf, was jedoch eine Voraussetzung für annähernd konstante Profildruckverteilungen ist.

Instationäre Auftriebsschwankungen aufgrund von Anstellwinkelschwankungen durch Böen werden mit Hilfe der Theorie dünner Profile gut vorhergesagt. Ein quasi-stationärer Ansatz gibt die instationären Vorgänge nicht vollständig wieder, erlaubt aber die Vorhersage, wann im Fall von Laminarprofilen die Laminardelle verlassen wird und Anstellwinkelschwankungen zu einen erhöhten Widerstand führen. Der Flug bei vermindertem Anstellwinkel stellt eine einfache Lösung des Problems dar. Die Fluggeschwindigkeit muss nur geringfügig erhöht werden, um den Anstellwinkel hinreichend zu vermindern.

Contents

Nomenclature

Latin Letters

Symbol	Dimension	Description
a	m/s	speed of sound of dry air
a	$-$	slope of lift curve per radian
b	m	wing span
C	$-$	global coefficient
c	$-$	local coefficient
c	m	chord length
D	m	Distance
D	N	drag force
d	m	diameter
E	kgm^2/s^2	energy
E	V	Voltage
e	$-$	Oswald factor
f	$1/s$	frequency
g	m/s^2	acceleration due to gravity
H	m	Height
k	$-$	gust alleviation factor
k	$1/m$	wave number
k_{red}	$-$	reduced frequency
L	N	lift force
L	m	characteristic length

l_m	m	mean chord length
M	$-$	Mach number
m	kg	mass
N	$-$	amplification factor
N	N	normal force
n	$-$	load factor
p	N/m^2	static pressure
q	N/m^2	dynamic pressure
R	N	aerodynamic force
R	m	flight range
R	$J/molK$	gas constant
Re	$-$	Reynolds number
S	m^2	wing area
T	K	temperature
T	N	thrust
Tu	$-$	turbulence level
t	t	time
U	m/s	vertical gust velocity
U_∞	m/s	free stream velocity
V	m/s	flight velocity
V	m^3	volume
W	N	weight force

Greek Letters

Symbol	Description	Unit
α	$^\circ$	angle of attack

β	$^\circ$	side slip angle
γ	$^\circ$	glide angle
δ	m	boundary layer thickness
ϵ	$m^2 s^{-3}$	energy dissipation rate
η	m	dissipative length scale
θ	$^\circ$	flow angle (hotwire)
μ	$kg/(ms)$	dynamic viscosity
μ	$-$	nondimensional airplane mass ratio
ν	m^2/s	kinematic viscosity
ρ	kg/m^3	density
τ	N/m^2	shear stress
φ	$-$	relative humidity
ω	$1/s$	circular velocity

Subscripts and Superscripts

Symbol	Description
avg	average
D	drag (3D-flow)
d	drag (2D-flow)
dyn	dynamic
f	friction
geo	geometric
hum	humid
i	induced
L	lift (3D-flow)
l	lift (2D-flow)

p	pressure
tr	transition
∞	free stream
$.'$	force per unit length
$.'$	turbulent fluctuation
$\bar{.}$	mean value

Abbreviations

Abbreviation	Description
ABL	Atmospheric Boundary Layer
AFM	Airplane Flight Manual
AoA	Angle of Attack
$\mathcal{AR}$	Aspect Ratio
BL	Boundary Layer
CBL	Convective Planetary Boundary Layer
CS	Certification Specification
CTA	Constant Temperature Anemometry
EFIS	Electronic Flight Information System
FAA	Federal Aviation Administration
FAR	Federal Aviation Regulations
FST	Free-Stream Turbulence
GPS	Global Positioning System
ISA	International Standard Atmosphere
LBA	Luftfahrt Bundesamt (German Civil Aviation Authorities)
LE	Leading Edge
NACA	National Advisory Committee for Aeronautics

NASA	National Aeronautics and Space Administration
NLF	Natural Laminar Flow
OAT	Outside Air Temperature
PBL	Planetary Boundary Layer (same as ABL)
SBL	Stably Stratified Planetary Boundary Layer
TE	Trailing Edge
UAV	Unmanned/Uninhabited/Unpiloted Aerial Vehicle

Speed Abbreviations

Abbreviation	Description
V_{CAS}	Calibrated Airspeed
V_c	Climb speed
V_g	Glide speed
V_{IAS}	Indicated Airspeed
V_S	Stall speed
V_s	Sink speed
V_{TAS}	True Airspeed

List of Figures

List of Tables

1. Introduction

Aircraft performance is an important aspect in aircraft design because it is a measure of the ability of the aircraft to carry out a specified task. Performance can refer to tasks relating to the flight path but also tasks involving stability, control or handling qualities.

In the beginning of aviation a major problem in aircraft performance was the attainment of sufficient lift, which was overcome using multi-wing configurations. Also the subject of stability and control wasn't understood yet and flying qualities were inadequate by today's standards. The lift problem was solved by the changeover from thin airfoils to thick airfoils and sufficient flight stability as well as controllability had been achieved by the time of WWI. Consequently, the improvement of aircraft performance moved into the focus of aircraft designers after these basic problems were solved. Advances in all fields of aircraft design - aerodynamics, propulsion and structures - led to considerable improvements of aircraft performance.

In the ongoing effort to improve aircraft performance, drag reduction is an important aspect. The reduction of airfoil drag is a major element in drag reduction. In the beginning of aviation, airfoil development was based primarily on trial and error. Systematic airfoil development started in the early 1920s primarily using experimental methods. This changed with the development of the stability theory in the early 1930s by Tollmien and Schlichting, showing a relationship between pressure gradient and the stability of the laminar boundary layer. This knowledge gave the theoretical background for the development of natural laminar flow (NLF) airfoils exhibiting a significantly reduced airfoil drag, for example is the pioneering NACA-6-series of 1939. With the development of the composite structures for sailplanes in the 1950s, the required smooth surfaces for NLF airfoils were producible. The great success of NLF airfoils in sailplane applications led to new efforts of NASA in the field of laminar flow research from the late 1970s until early 1990s. Due to the crises of General Aviation in the late 1980s only few aircraft were developed from a clean sheet and applying NLF principles. Nevertheless, the number of manned as well as unmanned aircraft using laminar airfoils has continued to increase.

Additionally, the application of laminar flow principles on commercial transport aircraft is a topic of current research because it promises considerable drag reductions. Drag reduction is an important component in the Clean Sky Joint Technology Initiative, which is a European aeronautical research programme launched in 2008. Its mission is to develop breakthrough technologies to significantly increase the environmental performances of airplanes and air transport, resulting in less noisy and more fuel efficient aircraft.

Laminar airfoils already proved their potential for drag reduction in many practical applications. However, the laminar boundary layer is sensitive to the effects of disturbances like noise, vibration and surface roughness as well as free-stream turbulence. A loss of glide performance has been reported for some modern gliders upon entering turbulent air within a thermal, whereas other gliders with similar airfoils do not show a performance loss. This finding calls for in-depth research since many GA aircraft and unmanned areal vehicles regularly operate under turbulent atmospheric conditions. Atmospheric turbulence is also found at high altitudes in or close to jetstreams. This means that also aircraft flying at high altitudes are affected.

Whereas the influence of severe atmospheric turbulence (gusts) on aircraft loads has been identified as an important issue and first theoretical models have been developed in the 1920s, much less research has been conducted on the influence of moderate turbulence on performance .

Flight in atmospheric turbulence with regard to aircraft performance has been addressed by different researchers with completely different approaches and is still far from being resolved. Using the lift-to-drag ratio L/D as measure of aerodynamic performance, the cause for a performance loss can either be a loss in lift, an increase in drag or a combination of both. An overview of the possible influencing factors is given in Figure 1.1.

Bertolotti [2] considers increased friction drag caused by premature transition. He investigates the effects of free-stream turbulence entering into the boundary layer of a laminar airfoil using a more simple flat plate model. He assumes a receptivity process of the laminar boundary layer to the microscopic scales of atmospheric turbulence. Temporal variations in the pressure distribution caused by angle of attack (AoA) variations are not considered.

Boermans [1] in contrast holds AoA variations responsible, which are caused by the macroscopic scales of atmospheric turbulence. He uses a

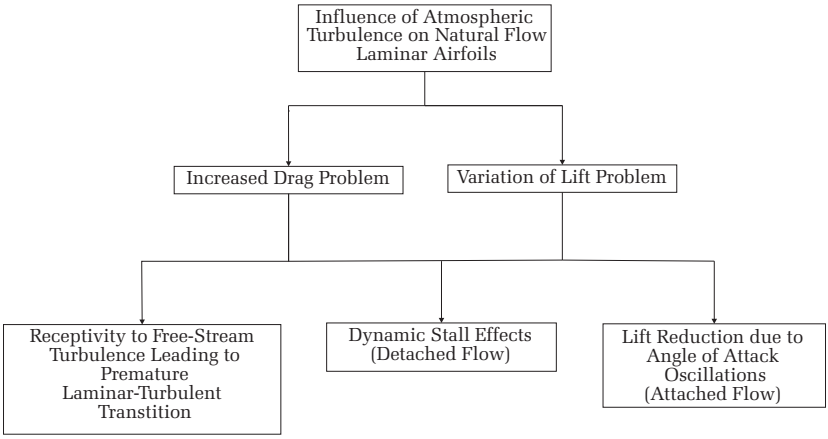

Figure 1.1.: Possible influences of atmospheric turbulence on aircraft performance.

quasi-stationary approach and neglects unsteady effects. Lift and drag variations are calculated from the static lift curve with AoA variations, measured on a sailplane in flight by Bernardy [3].

Another possibility is the occurrence of AoA variations which are fast enough to result in unsteady aerodynamic processes. In the worst case scenario this may lead to a dynamic stall.

The performance loss discovered on sailplanes in atmospheric turbulence is not solely a flight performance issue or a problem in the design and application of NLF airfoils. Much more it reveals a fundamental deficit in the design of aircraft. Different domains in aircraft design basically work next to each other but seldom altogether. On a number of occasions the simplifications in one domain cancel out the fundamental assumptions of another domain. Even in the field of aerodynamics separate research communities work on laminar-turbulent transition and unsteady aerodynamics with little interconnection and completely different approaches. Some simplifications may hold for well-controlled laboratory conditions but not for atmospheric turbulence. In many transition experiments a steady pressure distribution is assumed for example. This assumption does not hold in flight because microscale turbulence is a product of the decomposition of large scale turbulence, which does influence the pressure distribution.

It is obvious that aircraft performance under realistic conditions can differ from the performance figures obtained under ideal conditions. The main scientific goal of the present study is to gain a deeper understanding of the aerodynamic processes in flight under the influence of atmospheric turbulence. This influence can only be investigated under realistic conditions; hence in-flight experiments are required.

The influences of atmospheric turbulence on aircraft performance is a far reaching topic. Besides aerodynamics it also involves flight mechanics and meteorology. Therefore, an in-depth look into the latter topics is necessary to identify and isolate the aerodynamic problem. In this work the influence of turbulence on different aerodynamic quantities is investigated, interactions and prevailing mechanisms are identified and the influence on flight performance is quantified. In this context it is also investigated which mechanisms are universal for all types of aircraft and which mechanisms only apply to aircraft employing laminar flow airfoils.

This study is considered as the starting point for a larger project. The contributions include a theoretical analysis of the influence of atmospheric turbulence, and a review of relevant parts of aircraft performance theory and atmospheric turbulence in order to isolate the aerodynamic problem from the performance problem. Verification strategies are developed and requirements for an in-flight experiment are defined.

Another important part of this study is the development of a research aircraft with appropriate measurement equipment and its evaluation. Noteworthy is the design of a new wing glove with favorable aerodynamic characteristics and a completely new, cost-effective measurement system capable of measuring unsteady effects.

The last part of the study includes the development of flight test methods for unsteady conditions as well as the execution and the scientific analysis of the in-flight experiments.

2. State-of-the-Art and Objectives

2.1. Basic Considerations on Aircraft Performance

This work deals with aircraft performance under real atmospheric condition. The consideration of the complete aircraft is important because many quantities used in aerodynamics are coupled in flight and cannot be treated independently, as for example in theoretical or wind tunnel investigations. In addition, the influence of different aerodynamic quantities on aircraft performance varies with flight conditions. Therefore, an overview of classical performance theory to identify important aerodynamic quantities is given here before atmospheric turbulence is introduced as an additional factor on aircraft performance.

Aircraft performance can be defined as a measure of the ability of the aircraft to carry out a specified task. It can be used as a measure of the capability of the aircraft in many ways. Performance can refer to tasks relating to the flight path but also tasks involving stability, control or handling qualities. Therefore, it is an important aspect of airworthiness and can also be regarded as a measure of safety [4]. In the following the expression 'performance' will be taken to refer to tasks relating to the flight path of the aircraft. Other aspects like control and handling qualities are not a part of the scientific problem covered in this work. They will only be addressed in the development of a new wing glove for aerodynamic investigations since the resulting aircraft configuration is asymmetric.

The design of an aircraft starts from a statement of the flight-path-related performance that the aircraft is expected to achieve. The basic statement of performance will be concerned with the payload the aircraft will be required to carry and the mission profile it will be required to fly [4]. The mission profile divides the aircraft's typical mission into a sequence of characteristic flight conditions. For a civil transport aircraft the typical mission is to fly passengers and payload from the departure point to the destination. Exemplary mission profiles for civil and military applications are described more detailed in [4]. For sailplanes the typical mission is cross-country flight. The mission profile consists of two flight phases of almost identical duration, cross-country flight and climbing

in thermals. The design goal is to maximize the average cross-country speed. Thomas [5] gives an elaboration of cross-country theory and sailplane design optimization.

Following the definition of the mission profile, the next step in the design of a new aircraft or the modification of an existing aircraft is performance estimation, which is an iterative process. In each cycle the design is changed until estimated performance reaches the desired goals. Since performance estimation is based on simplified mathematical models, performance estimation must be validated. Performance measurement by means of flight testing is the only way to validate performance and demonstrate compliance with airworthiness standards. Flight tests for performance measurements are carried out by experienced test pilots with new aircraft in favorable atmospheric conditions. Performance data reduction is used to correlate performance to standard atmospheric conditions, which are defined in the International Standard Atmosphere (ISA) [6]. A comprehensive view on performance theory, flight testing and data reduction techniques is given among others by Eshelby [4] and Kimberlin [7].

Operational performance is the performance of an aircraft under real operational conditions. It can differ significantly from the performance values given for ISA conditions in the Airplane Flight Manual (AFM). Influences of air temperature and ambient pressure, that is air density, are well understood and can be taken adequately into account by means of performance planning. Performance planning with actual ambient conditions is basically the opposite of data reduction to ISA conditions during flight testing. Other influences in normal flight operations on aircraft performance include icing, insect contamination and atmospheric turbulence, the latter is the topic of this work. In the past atmospheric turbulence was studied with regard to gust loads. This work will also examine the effects on performance in particular aerodynamic performance of Natural Laminar Flow (NLF) airfoils.

2.2. Aircraft Performance under Ideal Conditions

2.2.1. Flight Mechanics of Relevant Flight Conditions

Classical performance theory for powered as well as non-powered aircraft uses simplified models assuming unaccelerated, trimmed flight conditions except for take-off, landing and maneuvering. Except for aircraft designed for maneuvering, e.g. aerobatic aircraft, transition phases be-

tween two steady flight conditions are neglected since they have no measurable influence on overall performance.

The most common flight condition for powered aircraft is the unaccelerated horizontal flight (Fig. 2.1(a)). The aerodynamic force acting on the aircraft R may be resolved into a component perpendicular to the flight path, the lift L, and a component parallel to the flight path, the drag D. To maintain level flight, weight W must equal lift L. This condition is referred to as horizontal flight condition.

$$L = W \tag{2.1}$$

To maintain a constant airspeed, thrust T must equal drag D.

$$D = T \tag{2.2}$$

It is readily identifiable that in the case of increased drag in horizontal flight, either the thrust must be increased accordingly or a deceleration is the result.

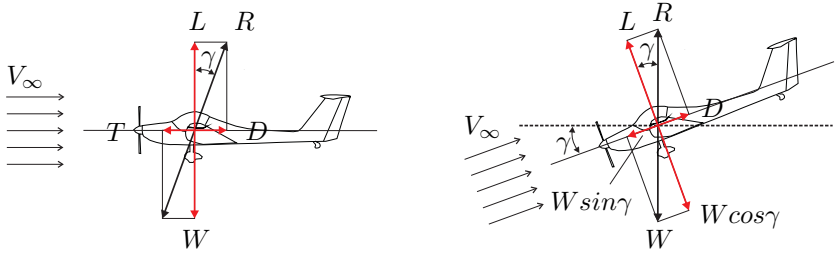

(a) horizontal flight (b) glide

Figure 2.1.: Balance of forces in trimmed flight.

By definition, a sailplane is not powered ($T = 0$). For this reason the only possibility to maintain a constant airspeed is a descending glide (Fig. 2.1(b)). The equilibrium of forces in glide can be expressed as follows:

$$L = W cos\gamma \tag{2.3}$$

$$D = W sin\gamma. \tag{2.4}$$

The flight path angle γ, that provides a steady state glide with equilibrium among acting forces, is called glide angle. It follows that the

tangent of the glide angle is the ratio of drag to lift:

$$tan\gamma = \frac{D}{L} = \frac{C_D}{C_L}. \tag{2.5}$$

The lift-to-drag ratio L/D is also known as the glide ratio:

$$L/D = \frac{C_L}{C_D} = \frac{1}{tan\gamma}. \tag{2.6}$$

The glide ratio is an important measure of performance for sailplanes as well as powered aircraft. Equation 2.6 shows that a performance decrease can result either from decreased lift, increased drag or a combination of both. Therefore, the influence of atmospheric turbulence on lift as well as on drag must be investigated, whether NLF airfoils are used or not.

2.2.2. Aerodynamic Performance

In the framework of flight mechanics aerodynamic forces are used in performance theory, equations of motion, stability and handling analysis with only a brief look into the underlying aerodynamic principles. It is the task of aerodynamics to provide the aerodynamic forces for the different aircraft components in terms of lift and drag polars, which are used in flight mechanics. Within this work it is assumed that the basic principles of fluid mechanics and aerodynamics are known. Therefore, only some basic definitions and equations relevant to this work are given for completeness here.

Generally, the aerodynamic force acting on an aircraft is the result of a three-dimensional flow field over the aircraft's surface. No matter how complex the body shape may be, the aerodynamic forces and moments have only two basic sources, the pressure distribution and the shear stress distribution on the surface (Fig. 2.2(a)). Resultant aerodynamic forces and moments (Fig. 2.2(b)) are calculated through integration of the local pressure and shear stress distribution along the body's surface. Detailed descriptions of the underlying aerodynamic principles (potential flow and boundary layer theory) can be found in many textbooks, e.g. Anderson [8], Schlichting and Truckenbrodt [9] or Schlichting and Gersten [10].

For a detailed consideration based on theoretical principles, dimensionless force and moment coefficients are used instead of aerodynamic forces and moments. With the density ρ_∞ and the velocity V_∞ in the freestream far ahead of the body, the dimensional quantity called the

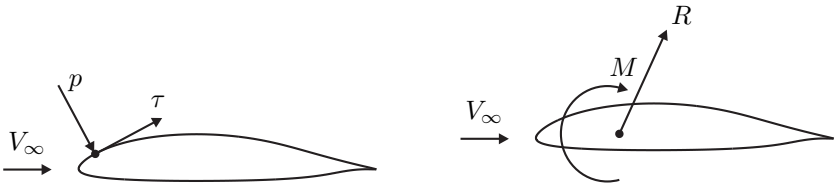

(a) Pressure and shear stress on an aerodynamic surface.

(b) Resultant aerodynamic force and moment on the body.

Figure 2.2.: Local and global aerodynamic forces on a body in a flow field.

freestream dynamic pressure q_∞ can be defined as:

$$q_\infty \equiv \frac{1}{2}\rho_\infty V_\infty^2. \tag{2.7}$$

With the reference area S the dimensionless lift and drag coefficients in case of a three-dimensional flow (e.g. aircraft or wing) are defined as follows:

$$C_L \equiv \frac{L}{q_\infty S} \tag{2.8}$$

$$C_D \equiv \frac{D}{q_\infty S}. \tag{2.9}$$

Symbols in capital letters denote force coefficients of a complete three-dimensional body such as an airplane or a finite wing. In this case the wing's planform area is taken as reference area S. In case of two-dimensional flows, forces and moments per unit span are used for the definition of the dimensionless coefficients, which are denoted by lower-case letters:

$$c_l \equiv \frac{L'}{q_\infty c} \tag{2.10}$$

$$c_d \equiv \frac{D'}{q_\infty c}. \tag{2.11}$$

The surface pressure p and the skin friction τ can be described by two additional dimensionless quantities, the pressure coefficient c_p

$$c_p \equiv \frac{p - p_\infty}{q_\infty} \tag{2.12}$$

and the skin friction coefficient c_f.

$$c_f \equiv \frac{\tau}{q_\infty} \tag{2.13}$$

where p_∞ is the freestream pressure.

Before performance can be calculated, the question which physical quantities determine the variation of aerodynamic forces must be answered first. From common physical knowledge it is expected that the aerodynamic force R of a body of given shape at a given angle of attack is a function of freestream density and velocity, viscosity and compressibility of the fluid and body size. With the dynamic viscosity μ and the freestream speed of sound a_∞ as a measure of compressibility, the aerodynamic force can be written as:

$$R = f(\rho_\infty, V_\infty, c, \mu_\infty, a_\infty). \tag{2.14}$$

The size of the body can be represented by some chosen reference length, the chord length c is chosen in case of an airfoil like the one in Figure 2.2. A set of dimensionless parameters governing the aerodynamic forces can be found using dimensional analysis:

$$f\left(\frac{R}{\frac{1}{2}\rho_\infty V_\infty^2 S}, \frac{\rho_\infty V_\infty c}{\mu_\infty}, \frac{V_\infty}{a_\infty}\right) = 0 \tag{2.15}$$

A description of the principles of dimensional analysis and the steps from Equation 2.14 to 2.15 can be found in [8] for example. The first term of Equation 2.15 is the dimensionless force coefficient C_R

$$C_R = \frac{R}{\frac{1}{2}\rho_\infty V_\infty^2}. \tag{2.16}$$

The second term in the parenthesis of Equation 2.15 is called the Reynolds number,

$$Re = \frac{\rho V c}{\mu} = \frac{V c}{\nu} \tag{2.17}$$

which is the ratio of inertial forces to viscous forces. Viscosity can be expressed either through the dynamic viscosity μ or the kinematic viscosity $\nu = \mu/\rho$. While the chord length c is used to calculate the Reynolds number for an airfoil, different characteristic reference lengths L are used in

other applications. The last term of Equation 2.15 is the Mach number

$$M = \frac{V_\infty}{a}. \tag{2.18}$$

Therefore, Equation 2.15 can also be written as follows:

$$f(C_R, Re, M_\infty) = 0. \tag{2.19}$$

This shows that C_R is a function of Re and M_∞ only.

$$C_R = f(Re, M_\infty) \tag{2.20}$$

The angle of attack α was kept constant for the analysis above. Without this constraint, C_R for a given body shape will also depend on α:

$$C_R = f(Re, M_\infty, \alpha). \tag{2.21}$$

Since the lift coefficient C_L and the drag coefficient C_D are components of C_R, they depend on the same parameters:

$$C_L = f(Re, M_\infty, \alpha) \tag{2.22}$$

$$C_D = f(Re, M_\infty, \alpha). \tag{2.23}$$

The dimensionless coefficients defined above are the basis of all aerodynamic considerations which are needed for performance calculations. The starting point for all performance calculations is an accurate lift and drag polar of the entire aircraft. Performance prediction methods are based on independent aerodynamic analysis of the individual aircraft components. Aerodynamic analysis uses theoretical calculations, wind-tunnel measurements, flight test data or a combination of those. For conventional aircraft lift contributions mainly come from the wing and the horizontal stabilizer, the fuselage influence is neglected. Drag contributions of all components are summed with additional interference drag. Sources of drag include but are not limited to the following:

- Profile drag of wing
- Induced drag of wing
- Fuselage drag

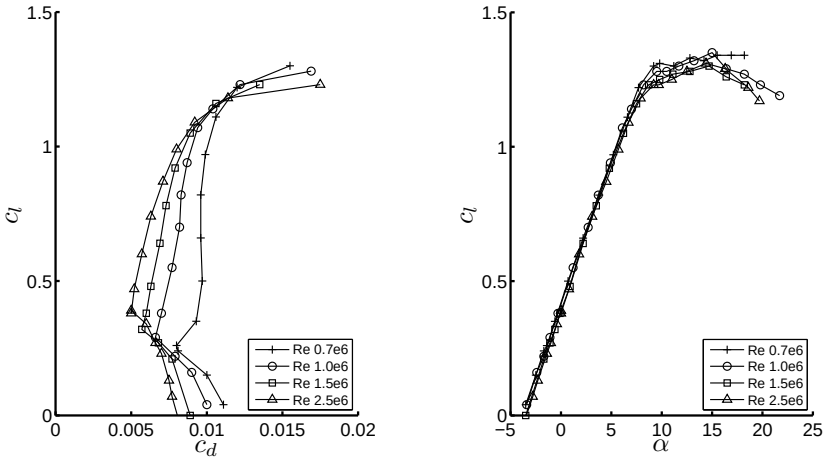

Figure 2.3.: AH 93-157 airfoil polar. Measurement in the Stuttgart laminar wind tunnel, from Althaus [11].

- Stabilizer drag, including profile drag and induced drag due to stabilizer lift
- Interference drag
- Drag due to surface imperfections and externally mounted equipment

Since individual aircraft components have different reference areas, aerodynamic coefficients of the individual components must be normalized to wing reference area before they are added up.

For a given aircraft geometry the estimation of the aircraft lift and drag polar normally starts with the airfoil polar. Figure 2.3 shows the c_l/c_d and c_l/α polar of the AH 93-157 airfoil, which is a typical example for NLF airfoils used on modern gliders. The Reynolds number effect on the drag is clearly visible since the airfoil drag in the laminar bucket roughly consists of two-thirds of friction drag and only one third pressure drag. Lift slope is not affected by the Reynolds number, only the high lift behavior is affected when flow detachments occurs due to boundary layer separation.

Airfoil polars can be obtained from wind tunnel measurements or numerical simulations. Simple panel programs based on potential flow

theory with added boundary-layer methods, like *xfoil* from Drela [12] or *profil* from Eppler [13], provide acceptable polars with little computational effort. Since boundary-layer velocity profiles are only modeled from similarity velocity profiles for special cases, the absolute value of friction drag often differs from wind tunnel measurements. Also the maximum lift coefficient and the processes beyond maximum lift cannot be predicted accurately because massive flow separation cannot be predicted by simple boundary layer models. The use of wind tunnel data to correct calculated polars is a good way to obtain accurate polars for a modified airfoil based on an existing airfoil.

In order to use airfoil polars, the Reynolds number Re must be similar to the flight Reynolds number. In conjunction with airfoil polars, the influence of compressibility is often not considered since compression is smaller than 5% for Mach numbers up to 0.3. In contrast to wind tunnel measurements where lift (through angle of attack) and Reynolds number (through freestream velocity) can be varied independently, they are coupled in flight as a result of the horizontal flight condition. From Equation 2.1 follows that lift must equal weight

$$\frac{1}{2}\rho V^2 S C_L = W \tag{2.24}$$

or after rearrangement

$$V = \sqrt{\frac{2}{\rho}\frac{W}{S}\frac{1}{C_L}}. \tag{2.25}$$

It is clearly visible that the flight velocity is proportional to the square-root of the wing loading W/S and inverse proportional to the square-root of the lift coefficient C_L for a given aircraft geometry. Inserting Equation 2.25 into Equation 2.17 yields the fundamental correlation between Reynolds number and lift coefficient in flight:

$$Re \propto \sqrt{\frac{1}{C_L}}. \tag{2.26}$$

Wind tunnel polars are typically measured at one or more constant Reynolds number for all AoAs, see Figure 2.3 for example, the Reynolds number varies with AoA in flight. In order to create a airfoil polar which resembles flight conditions, the airplane design parameters chord length c and wing loading W/S are assumed and Reynolds numbers for different lift coefficients are calculated. Then the airfoil polar is composed

out of the wind tunnel polars for different Reynolds numbers using the Reynolds number according to the lift coefficient. In *xfoil* either a wind tunnel polar, where Re and c_l are independent, or a flight polar, where c_l is a function Re (Eq. 2.26), can be calculated.

After the two-dimensional airfoil polar is created, the three-dimensional wing polar must be calculated. In contrast to the airfoil polar, the effects of the wing planform do not depend on Reynolds number directly since they can be explained with potential flow theory. There is only an indirect effect through the local chord length, which determines the local Re number, which again has an effect on the extent of the airfoil's linear lift range. Although the wide range of flight Re numbers is a critical point in the design of NLF airfoils for sailplanes, see Thomas [5] for details, it will not be discussed here. For simplification, only linear wing theory based on potential flow is considered. The most influencing factor in wing design is the aspect ratio $\mathit{A\!R}$.

$$\mathit{A\!R} \equiv \frac{b^2}{S} = \frac{b}{c} \tag{2.27}$$

It is defined as the wing span b to the power of two divided by the wing area S, which is in other words the ratio of wing span to mean chord length. The limiting case $\mathit{A\!R} \to \infty$ is two-dimensional flow. The lift slope $dC_L/d\alpha$ for a wing as a function of $\mathit{A\!R}$ can be calculated using Prandtl's lifting line theory for example, see [9].

$$\frac{dC_L}{d\alpha_{geo}} = \frac{2\pi \mathit{A\!R}}{\mathit{A\!R} + 2} \tag{2.28}$$

The limit of validity for this equation is $\mathit{A\!R} > 5$ [9]. Since the angle of attack for zero lift α_0 is identical for an airfoil and a wing, the wing lift slope (Eq. 2.28) substituted into the airfoil lift

$$c_l = (a_{geo} - a_0)\frac{dc_l}{d\alpha_{geo}} \tag{2.29}$$

gives the lift of a wing as a function of the angle of attack:

$$C_L = (a_{geo} - a_0)\frac{2\pi \mathit{A\!R}}{\mathit{A\!R} + 2}. \tag{2.30}$$

In reality, the value of airfoil lift slope $dc_l/d\alpha$ is a little bit smaller than 2π (from thin airfoil theory) and the real value is inserted into Equation

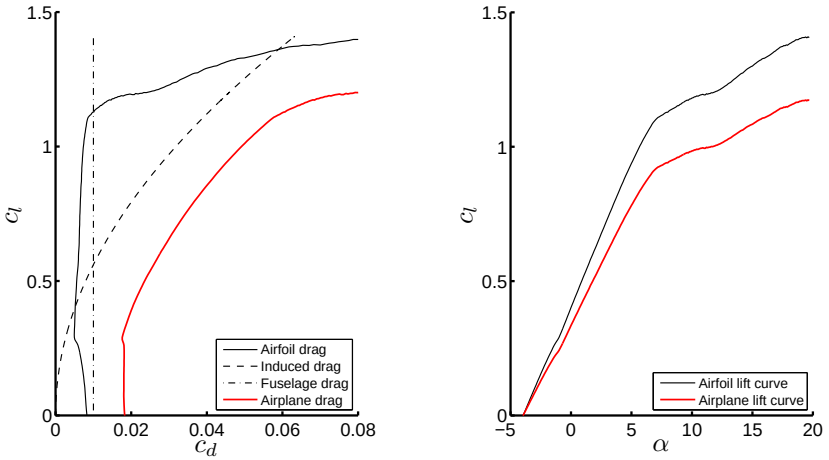

Figure 2.4.: Exemplary calculation of an airplane polar and lift curve composed of different components assuming $\mathcal{AR}$= 10 and a constant fuselage drag.

2.30 instead.

The induced drag coefficient $C_{D,i}$ only depends on the lift coefficient C_L and the wing shape:

$$C_{D,i} = \frac{{C_L}^2}{\pi e \mathcal{AR}} \tag{2.31}$$

For a wing with elliptic lift distribution the Oswald factor is $e = 1$, for any other other lift distribution the induced drag is higher, hence $e < 1$. The wing drag C_D is the sum of airfoil drag and induced drag:

$$C_D = c_d + \frac{{C_L}^2}{\pi e \mathcal{AR}} \tag{2.32}$$

In order to calculate the airplane's lift and drag polar, the lift and drag contributions from all components must be added. An example for the development of an airplane polar is given in Figure 2.4. With this polar the aerodynamic performance of an airplane is known and the aerodynamic forces can be extracted for the purpose of flight mechanics and performance calculations.

2.2.3. Performance Increase through Laminar Flow

Drag reduction is a key component in the pursuit of better aircraft performance. A laminar boundary layer has less friction drag compared to a turbulent boundary layer. Therefore, extending the amount of laminar boundary layer flow over the aircraft's surface reduces friction drag. It is obvious that aircraft which achieve good performance through laminar flow are prone to a performance loss due to factors causing premature transition.

Reducing airfoil drag is a major element in drag reduction. In the beginning of aviation, airfoil development was based primarily on trial and error. Some of the more successful designs were used as the basis for a family of airfoil sections tested by the NACA in the early 1920's. A major breakthrough was the NACA-4-series catalog of airfoils in 1933. Another notable early airfoil series is the Göttingen-series, which is basically Joukowski airfoils [9]. The stability theory developed in the early 1930's by Tollmien and Schlichting [10] shows a relation between pressure gradient in a flow along a surface and the stability of the laminar boundary layer, see Figure 2.5. This knowledge gave the theoretical background for the development of natural laminar flow airfoils, for example the pioneering NACA-6-series of 1939. Natural laminar flow means that the stability of the laminar boundary layer is only controlled passively through the airfoil's pressure distribution given by its shape and not through active flow control. Since a favorable pressure gradient stabilizes the laminar boundary layer, the point of maximum thickness is located further aft, compared to conventional airfoils, is a characteristic of all NLF airfoils. The aft placement of the point of maximum thickness is limited because this causes a strong increase in static pressure in the aft portion of the airfoil. This in turn causes boundary-layer separation leading to a high pressure drag and low lift. Up to a certain point it can be stated, that moving the point of maximum thickness backwards in airfoil design lowers drag in the laminar bucket but decreases the size of the laminar bucket [5].

A detailed description of the stability theory itself and an overview of the historic development is given by Schlichting and Gersten [10, Chapter 15] and will not be repeated here. Practical aspects of the application of NLF principles are discussed and an evaluation of capabilities and risks is given instead.

Despite the promising wind tunnel results, first NLF airfoils in real applications, e.g. NACA-6-series airfoils on the P-52, did not deliver the

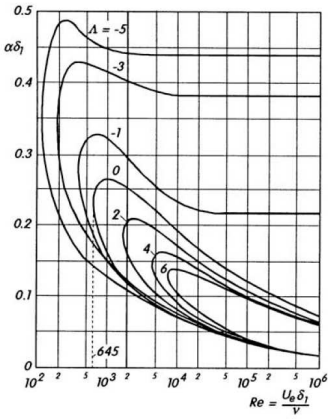

Figure 2.5.:
Neutral stability curves for laminar boundary layer velocity profiles with favorable ($\Lambda > 0$) and adverse ($\Lambda < 0$) pressure gradient, from [10].

projected performance. The required smooth surfaces could neither be realized in aluminum construction manufactured in mass production nor maintained in military or commercial service. Due to the limited success and a shift towards space activities, the development of NLF airfoils was abandoned by NACA.

With the development of the composite structures for sailplanes in the 1950's, the required smooth surfaces for NLF airfoils were feasible. NLF airfoils especially for sailplanes were developed by Wortmann (later published in [14]) as well as Eppler. While Wortmann took advantage of the Stuttgart laminar wind tunnel, Eppler had no access to this wind tunnel and developed a software for airfoil calculations and design. A comprehensive overview on the development and problems in the application of NLF airfoils for sailplanes until the 1980's is given by Boermans and Selen [15]. Later NLF airfoils for sailplanes can be found in [11]. Figure 2.6 shows the advances in airfoil drag reduction and compares airfoil drag with the friction drag of double-sided flat plate of equal size. Taking advantage of these technologies, the performance of the best sailplanes today has doubled compared to the best wooden sailplanes before "composite age", see [5].

The great success of NLF airfoils in sailplane applications led to new efforts of NASA in the field of laminar flow research from the late 1970's until early 1990's. Consequently, most literature in this field dates back to this time.

Holmes et al. [16] report the results of early in-flight laminar flow experiments with various airplanes and accompanying wind tunnel test:

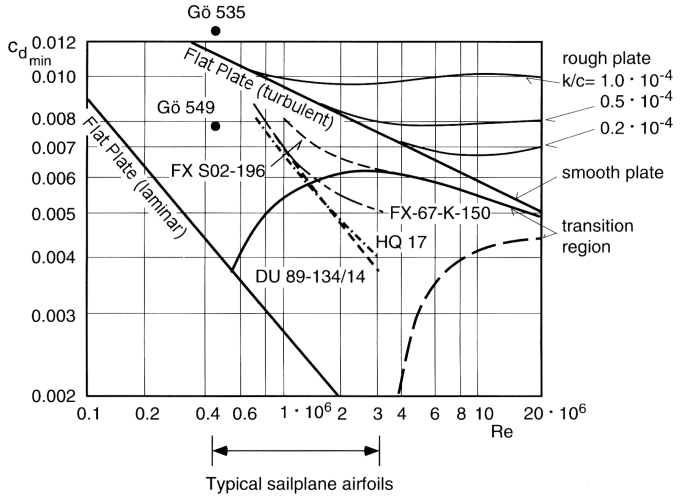

Figure 2.6.: Airfoil drag for laminar airfoils in comparison to flat plate friction drag, from Thomas [5].

"The airplanes tested were selected to provide relatively stiff skin conditions, free from significant roughness and waviness, on smooth modern production-type airframes. The observed transition locations typically occurred downstream of the measured or calculated pressure peak locations for the test conditions involved. No discernible effects on transition due to surface waviness were observed on any of the surfaces tested. None of the measured heights of surface waviness exceeded the empirically predicted allowable surface waviness. Experimental results consistent with spanwise contamination criteria were observed. Large changes in flight-measured performance and stability and control resulted from loss of laminar flow by forced transition. Rain effects on the laminar boundary layer caused stick-fixed nose-down pitch-trim changes in two of the airplanes tested. No effect on transition was observed for flight through low-altitude liquid-phase clouds. These observations indicate the importance of fixed-transition tests as a standard flight testing procedure for modern smooth airframes."

As a result, Holmes and Obara [17],[18] set up manufacturing requirements for NLF aircraft structures in terms of roughness and waviness. Dodbele et al. [19] developed design procedures for fuselages with long runs of natural laminar flow in the class of business-aircraft. Holmes

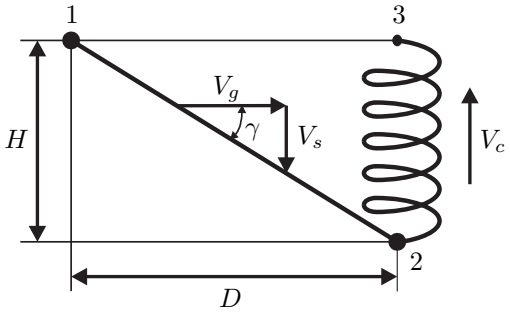

Figure 2.7.: Principle of sailplane cross-country flight consisting of two segments, interthermal glide ($1 \rightarrow 2$) and climb within a thermal ($2 \rightarrow 3$).

et al. [20] estimate a possible overall drag reduction of 24% for a business-jet employing NLF principles or 12% if NLF principles are only employed to the wing.

Due to the crises of the General Aviation in the late 1980's most airplane models manufactured today are heritage aircraft and received only minor upgrades. Since then only few aircraft were developed from a clean sheet and apply NLF principles. Nevertheless, the number of NLF aircraft continues to increase as do demands for further research on this topic.

2.2.4. Modeling Sailplane Performance

The loss of performance in atmospheric turbulence was discovered with sailplanes. For the development and assessment of theories on performance loss under turbulent conditions, a basic knowledge of sailplane performance is necessary. Therefore a brief description of sailplane performance is given. Although the glide ratio is the preferred sales argument, the characterization of sailplane performance is much more complicated. Maximum average cross-country speed is the ultimate goal for cross-country flight, which consists of two completely different flight conditions of almost equal duration.

Figure 2.7 shows the principle segments of sailplane cross-country flight, interthermal glide ($1 \rightarrow 2$) and climb within a thermal ($2 \rightarrow 3$), where the altitude lost in glide is recovered. The average cross-country speed is determined by the sum of the time which is required to glide t_g the distance D and the time to spend climbing t_c to the original altitude again:

$$V_{avg} = \frac{D}{t} = \frac{D}{t_c + t_g} \tag{2.33}$$

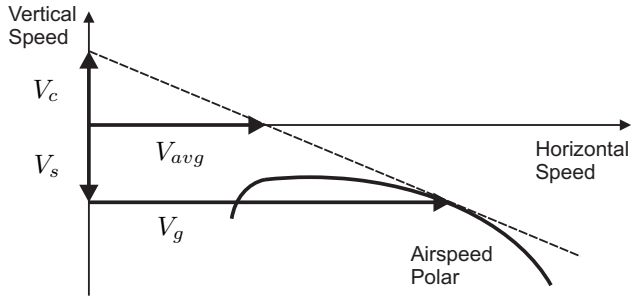

Figure 2.8.: Graphical solution to glide speed and average cross-country speed from sailplane performance polar and climb speed.

Figure 2.8 shows the graphical solution to MacCready's speed-to-fly theory, see Reichmann [21], with optimum interthermal glide speed V_g for a given climb rate V_c and performance polar. The climb rate V_c is the thermal strength V_T minus V_{Sc}, the sink rate of the circling sailplane. The resulting average cross-country speed V_{avg} can be found on the abscissa, since the mean vertical speed is zero at this point. A constant average cruise altitude is the requirement for cross-country flight. Therefore a high average cross-country speed is achieved by:

- Good climb performance in thermals
- Low sink rate in glide between thermals up to high flight speeds

In turn, every mechanism reducing either climb or glide performance has negative impact on the average cross-country speed as a measure of sailplane performance. Optimization of sailplane performance for a wide range of meteorological conditions, defined by strength and diameter of thermals mainly, is a tricky task in the design phase of a sailplane. Since the understanding of the processes in atmospheric turbulence is the topic of this work, refer to Thomas [5] for further details on sailplane design and its optimization.

2.3. Flight under Real Conditions

2.3.1. Known Influences on Operational Performance

The previous section gave a brief introduction to classical aircraft performance theory where flights take place in idealized conditions. However,

standard atmosphere pressure and temperature, calm and blue skies are seldom found in reality, only on rare occasions. Operational performance is influenced among other things by:

- Air density
- Steady wind
- Insect contamination
- Rain
- Frost and icing
- Runway condition

For example, air density, wind and runway condition have significant influence on take-off and landing performance while the wind is the most important influencing factor in terms of range. These topics are basics which can be found in every textbook on flight mechanics, e.g. [22] or [4]. As stated before, surface roughness is a critical point in the application of laminar flow principles because it leads to laminar-turbulent transition and increased drag. Therefore, surface contamination through insects, rain drops or frost is a negative factor especially for laminar airfoils. In contrast, airfoil shape modification as a result of icing has a severe impact on all types of airfoils.

The effects of insect contamination in NLF airfoils have been investigated since the 1950's and several protection methods were proposed, see Lachmann [23], Boermans and Selen [15] or Croom and Holmes [24]. Flight test evaluation of the LS-3 sailplane by Johnson [25] with 20 bugs per meter on the leading edge showed an increase in sink rate of roughly 20% over a large part of the horizontal speed range. Bug wipers are commonly used to remove insects from sailplane wings, their use on wind turbine blades is patented [26]. The influence of frost or rain drops is similar. Icing is an important topic and subject of current research due to its imminent danger on aircraft operations. The influence especially on NLF airfoils was studied for example by Chung and Addy [27]. Surface contamination of any type is not studied in this work and was minimal during the flight tests.

2.3.2. Influences of Atmospheric Turbulence

Influence on Aircraft Performance

Whereas surface contaminations of all types have been studied extensively, less research has been done on the influence of atmospheric turbulence in the context of aircraft performance. In contrast, much research has been done in the context of gust loads. One reason for neglecting turbulence can be found in FAA's Flight Test Guide [28, Chapter 2], which states:

"The purpose of §23.45(a) is to set the atmospheric standards in which the performance requirements should be met. The air should be smooth with no temperature inversions, mountain waves, and so forth. This is essential to obtaining good data and repeatable results. Non-standard conditions of temperature, pressure, and so forth, can be corrected to standard, but there are no corrections to compensate for poor quality data due to turbulence or poor pilot technique."

This shows that temperature and pressure variations are considered as as normal influences which can be corrected mathematically, whereas turbulence is considered as a disturbance leading to poor quality flight test results. Logical consequences on the other hand are, that turbulence has a considerable influence on performance and that this influence should be investigated and quantified.

Influence on Aircraft Loads

From the beginning of aviation atmospheric turbulence has been associated with gusts and consequently gust loads on the aircraft's structure. With regards to structural loads a vertical gust component is the most critical case since it results in sudden AoA change. This unsteady problem has been addressed in the 1920's and 1930's using thin airfoil theory and small AoA variations for attached flow. Wagner obtained a solution for the transient step change of AoA in 1925. Küssner (1935) addressed the problem of a sharp-edged vertical gust. Airloads on an oscillating airfoil were tackled by Glauert (1929) and the problem was solved by Theodorsen (1935). Von Karman and Sears (1938) solved the problem of a sharp-edged and sinusoidal vertical gust. A summary with references and relevant equations is given by Leishman [29, Chapter 8].

For the certification of sailplanes [30] and airplanes up to 5700 kg [31],[32] a simplified procedure for calculation of applicable load factors as result of a gust is used. Static gust load factors n are calculated from

the empirical equation given in CS 22.341 or CS/FAR 23.341:

$$n = 1 \pm \left[\frac{\left(\frac{k}{2}\right) \rho_0 U V a}{\left(\frac{mg}{S}\right)} \right] \tag{2.34}$$

using the following dimensional and dimensionless quantities:

ρ_0	=	density of air at sea-level $[kg/m^3]$
U	=	gust velocity $[m/s]$
V	=	equivalent airspeed $[m/s]$
a	=	slope of wing lift curve per radian $[m/s]$
m	=	mass of airplane $[kg]$
g	=	acceleration due to gravity $[m/s^2]$
S	=	design wing area $[m^2]$
k	=	gust alleviation factor $[-]$

The gust alleviation factor is calculated from the formula

$$k = \frac{0.88\mu}{5.3 + \mu} \tag{2.35}$$

where

$$\mu = \frac{2\frac{m}{S}}{\rho l_m a} \tag{2.36}$$

is the non-dimensional airplane mass ratio with

ρ	=	density of air $[kg/m^3]$ at the altitude considered
l_m	=	mean geometric chord of wing $[m]$

CS 22.341 also states that the value of n does not need to exceed

$$n = 1.25 \left(\frac{V}{V_{S1}} \right)^2 \tag{2.37}$$

where V_{S1} is stall speed in steady horizontal flight. Assuming a gust velocity U of $15m/s$ at design gust speed V_B and $7.5m/s$ at design maximum speed V_D the load factors for a given aircraft can be calculated. A graphical depiction of the airplane's gust envelope is the V-n-diagram in Figure 2.9.

Looking into Equations 2.34 to 2.37, some principle influence quantities on airplane behavior under the influence of atmospheric turbulence can be seen without a deeper look into aerodynamics or flight mechanics:

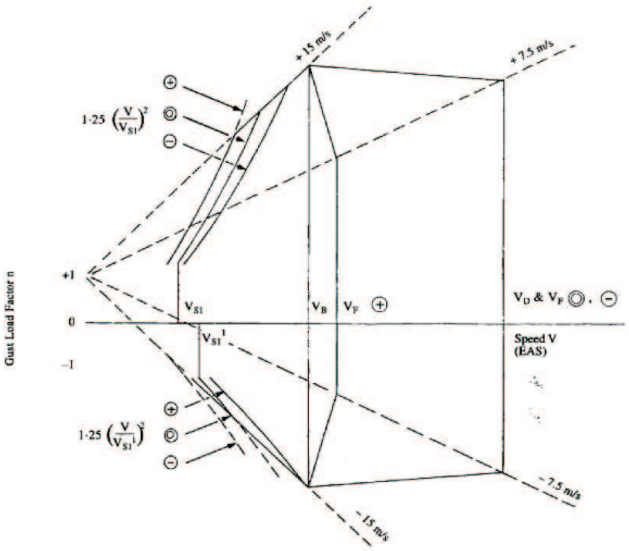

Figure 2.9.: Gust envelope from CS22 [30].

- Gust velocity and aircraft's speed
- Slope of wing lift curve → wing aspect ratio
- Wing loading
- Dynamic stall effects with lift increase over the static maximum can occur (Eq. 2.37)

Since the airplane reaction not only depends on the gust speed but also on the flight speed, the aspect ratio and the wing loading, the same gust feels different in various types of aircraft. Pilot reports on turbulence strength, see Table 2.1 for turbulence reporting criteria, therefore imply no information on the actual gust velocity. Nevertheless, they are helpful for other pilots and air traffic control.

MacCready [33] proposes a procedure to standardize gustiness values from aircraft. He uses the standard deviation of the airplane's vertical acceleration $\sigma_{\triangle n}$ as a measure of turbulence severity from the pilot's view independent from the type of aircraft:

Intensity	**Aircraft Reaction**	$\sigma_{\triangle n}$ (5 *sec.*)
Light	Turbulence that momentarily causes slight, erratic changes in altitude and/or attitude (pitch, roll, yaw).	$\sigma_{\triangle n} \leq 0.1$
Moderate	Turbulence that is similar to Light Turbulence but of greater intensity. Changes in altitude and/or attitude occur but the aircraft remains in positive control at all times. It usually causes variations in indicated airspeed.	$0.1 \leq \sigma_{\triangle n} < 0.3$
Severe	Turbulence that causes large, abrupt changes in altitude and/or attitude. It usually causes large variations in indicated airspeed. Aircraft may be momentarily out of control.	$0.3 \leq \sigma_{\triangle n} < 0.6$
Extreme	Turbulence in which the aircraft is violently tossed about and is practically impossible to control. It may cause structural damage.	$0.6 \leq \sigma_{\triangle n}$

Table 2.1.: FAA turbulence reporting criteria, see [36], and typical $\sigma_{\triangle n}$ values from [34].

Negligible	$\sigma_{\triangle n} \leq 0.05$
Slight	$0.05 < \sigma_{\triangle n} \leq 0.10$
Moderate	$0.10 < \sigma_{\triangle n} \leq 0.20$
Moderately heavy	$0.20 < \sigma_{\triangle n} \leq 0.30$
Very heavy	$0.30 < \sigma_{\triangle n}$

To this day, there is no official definition of turbulence severity in terms of absolute or mean vertical accelerations due to gusts. Mean values $\sigma_{\triangle n}$ for a running 5 second interval from newer sources [34],[35] are similar to the values used by MacCready [33].

MacCready correlates turbulence intensities in typical meteorological conditions, e.g. turbulence through a thermal or thunderstorm, and the energy dissipation rate. It will be shown in the following chapter that the energy dissipation rate ε is the measure of atmospheric turbulence intensity. Figure 2.10 shows the proposed turbulence magnitude scale

with ε and descriptive meteorological condition. This scale is independent from an aircraft. For each particular aircraft a response function, which also depends on the aircraft's speed, can be found. The relation between ε and aircraft response is fundamental in newer research on the use of onboard Doppler radar for gust detection and load alleviation [34],[35] but not discussed further.

Most of the research on atmospheric turbulence is focused on stronger turbulence and motivated by the determination of structural loads or load alleviation techniques for reduced maximum loads or improved ride qualities under turbulent conditions. Nevertheless, also for light and moderate turbulence addressed in this work, essential concepts can be derived.

2.4. Similar Challenges in other Applications

2.4.1. Other Classes of Aircraft

The performance loss with increasing atmospheric turbulence level was discovered on modern gliders with NLF airfoil. This was reported by Waibel, the designer of the ASW24 sailplane, in personal communication. Probably other classes of aircraft are affected, too. A growing number of aircraft designs, e.g. general aviation aircraft, business jets and Unmanned Areal Vehicles (UAVs), are built from composite materials and use NLF airfoils. Changes in the lift-to-drag ratio have a direct influence on the range of an aircraft. Maximum range R can be approximated using the Breguet range equation, e.g. see [22]. For aircraft with power-producing engines (propeller-driven) with a given propulsive efficiency η_j and specific fuel consumption c_p the range becomes:

$$R = \frac{\eta_j}{c_p} \frac{C_L}{C_D} ln \frac{W_1}{W_2} \tag{2.38}$$

Equation 2.38 shows that the range linearly depends on L/D. It can be shown that this linear relation is independent from the type of propulsion. For aircraft with thrust-producing engines (turbo-fans, turbo-jets) the range depends on flight profile but is still linearly dependent on L/D. For aircraft applying laminar flow principles, premature transition through turbulence or surface contamination increases drag, lowers L/D and the range. An example for a modern business jet with NLF surfaces is the *HondaJet*, which is currently under development [37]. NLF principles are systematically used for all aircraft components. Fujino

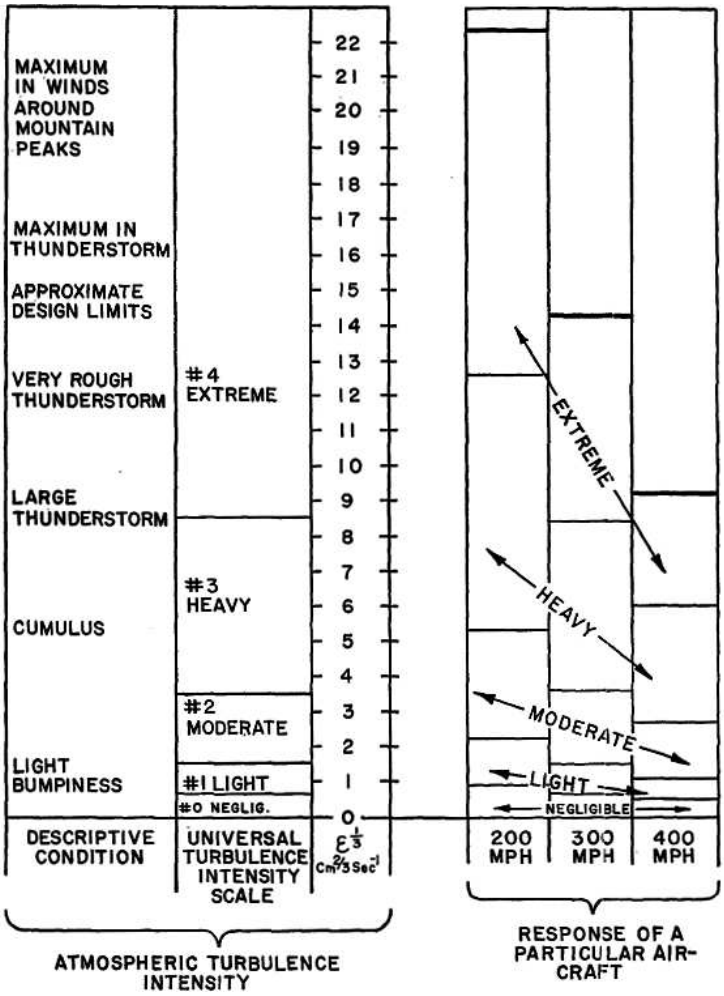

Figure 2.10.: Turbulence intensity scale and response of a particular aircraft, from [33].

et al. [38] describe the development of the NLF airfoil which is based on a NASA high-speed laminar airfoil [39]. In cruise flight, the transition location is located at 0.45 c on the airfoil suction side. Under this condition a transition strip at 0.2 c causes a 10% in airfoil drag increase

whereas transition strip located at 0.1 c already causes a 50% increase in airfoil drag. Airfoil drag is only one part of the aircraft total drag but it is a significant one under cruise conditions. In long range operations increased drag through a loss of laminar flow can easily use up a typical safety margin of 10% to the maximum range.

Most UAVs employ NLF principles and therefore are influenced by atmospheric turbulence in the same manner as manned aircraft, especially since many smaller UAVs operate at lower altitudes within the atmospheric boundary layer. A decrease in L/D not only reduces the range, but in many applications more important also the endurance because a higher power setting is necessary to hold altitude while loitering.

A relatively new but very promising approach for smaller UAVs in order to gain performance instead of losing performance under turbulent conditions in the convective boundary layer is autonomous soaring. It can be used to improve the range, duration or cross-country speed of an autonomous aircraft. Many UAVs have similar sizes and wing loadings to soaring birds and manned sailplanes. Strategies for extracting energy from thermals and other sources have been published for glider pilots, see for example Reichmann [21]. Three different techniques are used by glider pilots and soaring birds:

- Climb through circling in thermal convection
- Optimal soaring strategy (flight path and speed-to-fly technique)
- Dynamic soaring in wind shears

The first two techniques are commonly used by glider pilots in thermal conditions or uplifts due to ridges whereas dynamic soaring is inspired by the flight of the albatross using vertical wind gradients, see Sachs [40],[41].

Autonomous thermal soaring UAVs were first proposed by Wharington and Herszberg [42] in 1998 as a method to extend UAV performance but their learning algorithms for thermal flight were computationally too intensive for real-time use. Less complex autonomous soaring autopilots hosted on a number of model glider airframes have been used to detect and use thermals to gain altitude with mixed results. A guidance and control method for autonomous soaring flight in thermal updrafts was developed and successfully tested by Allen [43] using a small electric-powered UAV. This control method was later patented [44]. Andersson et al. [45] developed and successfully demonstrated a centering controller

that is based on a thermal centering technique for manned gliders proposed by Reichmann [21]. Akos et al. [46] present an overview of the knowledge of the soaring flight and flight strategies of birds and compare it with control strategies that have been developed for soaring UAVs. They investigated the flight of peregrine falcons employing GPS tracking. Akos et al. [46] found flight path and speed optimization techniques in the flight of falcons. Falcons instinctively apply the speed-to-fly theory that was originally developed and described by Paul MacCready, see Fig. 2.8, and since then is widely used by pilots in thermal soaring.

Optimal soaring techniques can be used by soaring UAVs for the cross-country flight between thermals or by powered UAVs either to reduce the required power or increase average cross-country speed, see Patel et al. [47],[48]. Basic concept of speed to fly theory is to increase flight speed in a downdraft (to penetrate it in a short time) and decrease flight speed in an updraft (for a longer use of the lift). Because this technique results in continuous altitude variations and looks like the movement of dolphins, it is also called dolphin flight. This is a major deviation from the typical control concept in powered flight of flying at a constant altitude. Using this concept the speed in a downdraft is reduced in order to maintain altitude and speed in an updraft is increased. This means that in average more time is spent in a downdraft then in an updraft, which in turn lowers average speed. Optimized flight path planning instead of straight line flight in order to fly through more regions with updrafts and use their lift is another technique routinely used by glider pilots and also proposed for UAVs, see Chakrabarty and Langelaan [49].

Dynamic soaring is a technique to extract energy from vertical wind velocity gradients instead of using thermal convection. Wind shears mainly can be found close to the ground, near inversions or at the tropopause. Optimal dynamic soaring is described amongst others by Zhao [50] or Sukumar and Selig [51] and involves continuous maneuvering. As the speed-to-fly theory, it can either be applied in unpowered applications or in powered applications to minimize required power and fuel consumption [52].

The application of soaring techniques to UAVs results in a highly dynamic flight and involves continuous maneuvering and the presence of atmospheric turbulence is a precondition. Given the potential of this approach, it is an additional reason to investigate the influence of atmospheric turbulence on laminar airfoils.

2.4.2. Wind Turbines

Another aerodynamic application with similar, unsteady flow conditions is wind turbines. Inherent to the operation close to the ground in the atmospheric boundary layer, the blades move through turbulent flow with a vertical velocity gradient. The turbulence level is mainly determined by the site where the wind turbine is located. In rough terrain higher turbulence levels are found compared to off-shore applications or in flat terrain sites. Fluctuations in wind velocity act as AoA variations and/or plunging motions in the rotating blades coordinate system. Further unsteadiness arises when the rotation is misaligned to the mean flow direction, i.e. yawed. A comprehensive overview is given in the textbook written by Hau [53].

For modern wind turbines with typical tip speed ratios of about 6 to 8, the magnitude of AoA variations is similar to the magnitude of AoA variations in flight through vertical gusts. Changes in lift or drag influence the performance as well as the bending moments on the blades and the tower. Unsteady aerodynamic effects on wind turbine blades are a topic of current research. Wind turbine aerodynamics and unsteady aircraft aerodynamics therefore complement each other.

2.4.3. Helicopter Aerodynamics

Although the problem of an aircraft encountering AoA variations due to atmospheric turbulence is less complex and different airfoils are used, much effort has been spent in the field of helicopter aerodynamics to investigate unsteady airfoil behavior. Therefore, concepts from rotor aerodynamics will be used in this work.

The aerodynamic complexity of a helicopter in forward flight is much higher compared to an aircraft in forward flight. The flow field in which the rotor operates is more complex because of the individual wakes and tip vortices trailed from each rotor blade. With increasing forward speed the asymmetric flow over the rotor disk gives rise to a number of aerodynamic problems. The blade tips at the advancing side of the rotor reach high Mach numbers up to transonic speeds with associated problems like compressibility or even strong shock waves. On the retracting side of the rotor the flow velocity is low and high AoAs are required to produce lift. A detailed description of all problems is given by Leishman [29].

2.5. Objectives and Contributions of this Work

Outline of the Scientific Problem

The performance loss discovered on sailplanes in atmospheric turbulence is not solely a flight performance issue or a problem in the design and application of NLF airfoils. Much more it reveals a fundamental deficit in the design of sailplanes and other aircraft. Different domains in aircraft design basically work next to each other but seldom altogether. Each domain uses assumptions and simplifications and results are made available via predefined interfaces. On a number of occasions the simplifications in one domain cancel out the fundamental assumptions of another domain. Even in the field of aerodynamics separate research communities work on laminar-turbulent transition and unsteady aerodynamics with little interconnection and completely different approaches. For example a steady pressure distribution is assumed for investigations on the influence of microscale turbulence in transition research whereas the influence of microscale turbulence is neglected. In unsteady aerodynamics AoA oscillations and their influence on pressure distribution are examined but microscale turbulence is not considered.

A good example for the problem is the interaction between meteorology and sailplane performance. A multidisciplinary approach is used to optimize sailplane design with regard to cross-country speed. Therefore meteorological models are used to describe thermals (strength, size and distribution) and design parameters as wing loading or aspect ratio are optimized. In the same optimization process a quasi-stationary treatment of lift and drag is used with airfoil polars, which were obtained in turbulence-free conditions. The existence of thermals together with turbulence-free inflow is a clear contradiction to actual meteorological conditions.

Scientific Objectives

It is obvious from the presentation of the problem that aircraft performance under realistic conditions can differ from the performance figures obtained through flight testing under ideal conditions significantly. The main scientific goal is to gain a deeper understanding of the aerodynamic processes in flight under the influence of atmospheric turbulence. Therefore, theoretical models taking this influence into account must be developed, interactions and prevailing mechanisms must be identified and the influence on flight performance must be quantified. To achieve

these goals, a new multidisciplinary approach taking the following fields into account is necessary:

- Aircraft performance
- Loads and aeroelasticity
- Meteorology
- Unsteady aerodynamics
- Laminar-turbulent transition, receptivity

The first items are applicable to all aircraft whereas the last item only applies to aircraft employing laminar flow technologies. Special attention is payed to the last point with the goal of developing a design-criterion for NLF airfoils that they are not negatively effected by atmospheric turbulence.

Contributions of this Study

The influence of atmospheric turbulence on aircraft performance is a far reaching topic. This work is the starting point for a longer project working on the objectives defined above. Furthermore, the developed research aircraft and the additional equipment is also a new start for other in-flight experiments in the field of active flow control. The contributions of this work can be divided into three parts:

Theoretical analysis: The emphasis of the first part is theoretical analysis of the influence of atmospheric turbulence. The theoretical analysis includes a review of relevant parts of aircraft performance theory (Chapter 2) and a literature survey on atmospheric turbulence (Chapter 3.1) as well as existing theories on the performance loss (Chapter 3.2). An important step is the extraction of the aerodynamic problem from the performance problem and the critical analysis of the theories on performance loss. Verification strategies are developed and requirements for an in-flight experiment are defined.

Research aircraft: The emphasis of the second part is the development of a research aircraft with appropriate measurement equipment and its evaluation. Most important items are the design of a new wing glove with favorable aerodynamic characteristics and a completely

new, cost-effective measurement system capable of measuring unsteady effects (Chapter 4). The system evaluation by means of numerical simulations, wind tunnel and flight tests is another important aspect (Chapter 5). It is the prerequisite in order to obtain accurate results in the last part of this work and future projects.

In-flight experiments under atmospheric turbulence: The third part includes the development of flight test methods for unsteady conditions, the execution and the scientific analysis of in-flight experiments. Prevailing influence mechanisms are identified and future improvements for a more detailed study are proposed.

3. Theoretical Analysis

3.1. Flight environment

3.1.1. Earth's Atmosphere and Atmospheric State

Temperature and pressure as well as turbulence intensities are quantities of the atmospheric state. In the following, a brief overview on the Earth's atmosphere and some typical conditions are given.

The atmosphere can be divided into five main layers. Starting from the ground up these layers are the troposphere, stratosphere, mesosphere, thermosphere and exosphere. Each of these layers has a different lapse rate, defining the rate of change in temperature with height. As mentioned before, different models describe a standardized atmosphere state, e.g. the International Standard Atmosphere (ISA) [6].

The troposphere begins at the surface and extends to between 9 km at the poles and 17 km at the equator with some variation due to the weather, see Figure 3.1. The tropopause is the boundary between the troposphere and the stratosphere. The troposphere is mostly heated by transfer of energy from the surface, so in average the lowest part of the troposphere is the warmest and temperature decreases with altitude. This promotes vertical mixing, which is the primary source for atmospheric turbulence in the troposphere, see Etling [54].

Other sources of atmospheric turbulence are shear flows at inversion layers [54]. Typical examples are jet streams, which are fast flowing and narrow air currents found in the free atmosphere near the tropopause. The major jet streams on Earth are westerly winds (flowing west to east). Jet streams have influence on flight operations near the tropopause in two different ways. Flight time can be dramatically affected by either flying with the flow or against the flow of a jet stream. Clear-air turbulence often is found in a jet stream's vicinity. The jet stream is only mentioned here to show that even in the stable atmosphere at high altitudes, a source of atmospheric turbulence exists.

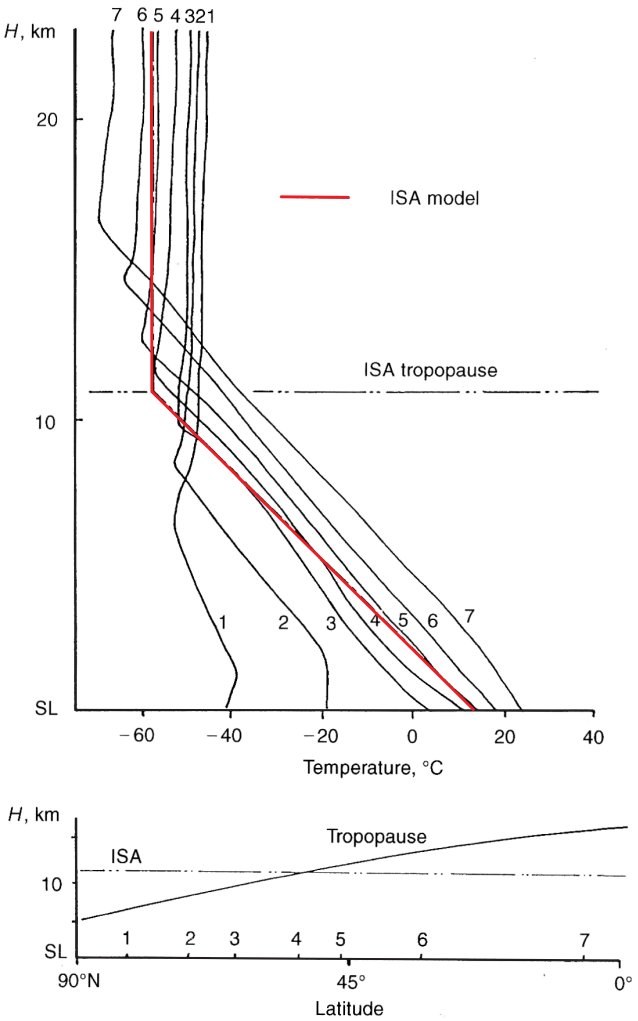

Figure 3.1.: Atmosphere's temperature distribution measured at different geographical positions and standard atmosphere, from Eshelby [4].

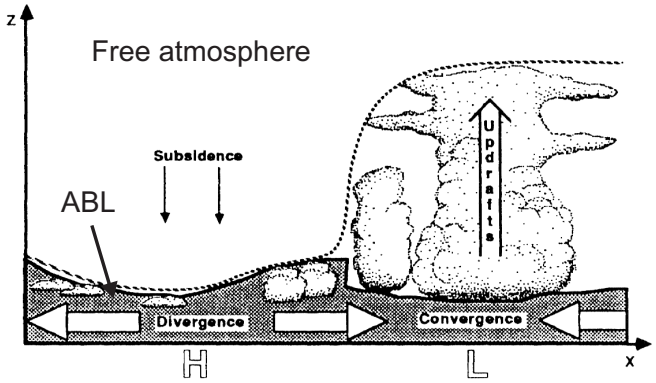

Figure 3.2.: Definition of the atmospheric boundary layer, from Stull [55].

3.1.2. Atmospheric Boundary Layer

The troposphere itself can be divided into two parts, see Figure 3.2. The atmospheric boundary layer (ABL), also known as the planetary boundary layer (PBL), and the free atmosphere above. The ABL is the part of the troposphere that is nearest to the Earth's surface and is directly affected by it. During daytime the ABL usually is well-mixed, while at nighttime it becomes stably stratified with weak or intermittent mixing. The depth of the planetary boundary layer ranges from as little as about 100 m on clear, calm nights to 3000 m or more during the afternoon in dry regions. Above the ABL is the free atmosphere where the wind is approximately geostrophic. Normally, the top of the ABL is a capping inversion layer which is the upper limit for thermal convection and associated turbulence. The free atmosphere is usually stable and therefore non-turbulent. In cases of an unstable atmosphere, thermal convection can go up to the tropopause (thunderstorms). In this case the upper limit of the ABL, or the lower limit of the free atmosphere respectively, is defined by the cloud base, although there is turbulent mixing up to the tropopause, see Stull [55].

3.1.3. Atmospheric Turbulence

Atmospheric turbulence is one important element of the atmospheric state. It is characterized by simultaneous occurrence of multiple sizes of

Scale	Horizontal length scale	Locale
Micro	< 1 km	local
Meso	1 km - 100 km	regional
Macro	100 km - 10 000 km	continental

Table 3.1.: Meteorological definitions of spatial scales.

turbulent eddies, described e.g. by time or length scales, see Wyngaard [56]. Turbulence can be found within the convective boundary layer of the atmosphere but also in conjunction with thunderstorms and shear layers. Definitions of the spatial scales used in meteorology are given in Table 3.1. Microscale meteorology is the study of short-lived atmospheric phenomena smaller than mesoscale, about 1 km or less, and a duration of less than an hour. Thermal convection in the atmospheric boundary layer is an example for one of the biggest phenomena studied in micrometeorology. Thunderstorms are considered as a mesoscale phenomenon. Meteorological scale definitions should not be confused with turbulent scale notations used in aerodynamics in the following chapters. In aerodynamics, turbulent scales larger than a chord length with influence on the whole airfoil will be referred to as macro scale turbulence. Smaller scales with influence only to the boundary layer will be referred to as micro scale turbulence.

Since flights with sailplanes under turbulent conditions mostly take place in the atmospheric boundary layer, a more detailed look at this atmospheric layer is necessary. The state of the ABL can be described by two principle types. One type is the convective planetary boundary layer (CBL), where positive buoyancy flux at the surface from solar heating (negative temperature lapse rate with altitude) creates a thermal instability and thus generates additional or even major turbulence. The CBL is typical in mid-latitudes during daytime. The other type is the stably stratified planetary boundary layer (SBL), where negative buoyancy flux at the surface (positive temperature lapse rate = inversion) dampens the turbulence. The SBL is typical at nighttime at all locations and even at daytime in places, where the Earth's surface is colder than the air above.

The development of the ABL over the course of one day is shown in Figure 3.3. During the day the ABL is of the convective type with strong turbulent mixing, therefore the CBL is also called mixing layer. When the ground cools in the evening the lowest part of the ABL becomes stable (SBL). In this stable layer turbulence dissipates faster than

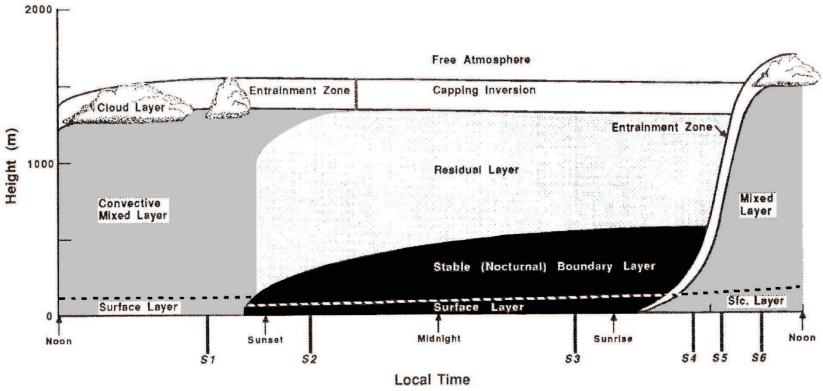

Figure 3.3.: Structure of the atmospheric boundary layer over the course of one day, from Stull [55].

in the less stable residual layer above. The turbulence intensity in the residual layer decays over the course of the night and the early morning. Since calm air is required for performance flight testing, flight tests typically take place either in the stable layer, the residual layer or the free atmosphere.

In turbulence theory for high Reynolds number flows the largest scales in the energy spectrum are called integral length scales. These eddies obtain energy from the mean flow and also from each other. Thus, these are the energy production eddies which contain the most of the energy. They have the large velocity fluctuation, are low in frequency and are highly anisotropic. In case of atmospheric turbulence in the ABL, turbulent kinetic energy is generated through thermal convection. Therefore, the largest eddies have sizes in the order of the convective boundary-layer thickness δ_{CBL} [55].

To sustain turbulent flow a constant source of energy supply is required. During daytime solar heating and consequent thermal convection is the required source. Otherwise, turbulence dissipates rapidly as the kinetic energy is converted into internal energy (heat) by viscous shear stress. This happens at night, see Figure 3.3.

Turbulence causes the formation of eddies of many different length scales. Most of the kinetic energy of the turbulent motion is contained in the large scale structures. The energy is transferred from these large scale structures to smaller scale structures by an inertial and essentially

inviscid mechanism, which is called the energy cascade. In the inertial range the turbulent kinetic energy of large eddies is transferred down to a larger number of smaller eddies while the total energy stays constant. This process continues, creating smaller and smaller structures until these structures are small enough that molecular diffusion becomes important and viscous dissipation of energy finally takes place [57]. The dissipative length scale η is also called Kolmogorov scale.

$$\eta = \left(\frac{\nu^3}{\varepsilon}\right)^{\frac{1}{4}} \tag{3.1}$$

This scale depends only on the kinematic viscosity ν and the dissipation rate par unit volume ε of turbulent kinetic energy.

The application of Kolmogorov's hypothesis on the small-scale structure of turbulent motion to atmospheric diffusion was first proposed by Batchelor [58]. He estimated the dissipative scale in the lower layers of the atmosphere in the order of $\eta = 2\ mm$. Similar estimations are given by Wyngaard [56]. The range of turbulent scales in the atmospheric boundary layer is

$$\eta \ll L_e \ll \delta_{CBL}. \tag{3.2}$$

where the large eddy range is in the order of δ_{CBL} and the dissipative range in the order of η (Equation 3.1).

The intermediate scales between the largest and the smallest scales make up the inertial subrange $O(L_e)$. They are not dissipative and pass down the energy from the largest to the smallest scales without dissipation. Kolmogorov's theory describes how energy is transferred from larger to smaller eddies, how much energy is contained by eddies of a given size and how much energy is dissipated by eddies of each size. For homogeneous turbulence, the turbulent kinetic energy k is the same everywhere in space.

Kolmogorov argued that the directional biases of the large scales are lost in the chaotic scale-reduction process as energy is transferred to successively smaller eddies in the inertial subrange. Hence the small-scale turbulent motions are statistically isotropic. Large scale turbulence may still be anisotropic. Kolmogorov also argued that not only the directional information gets lost as the energy passes down the cascade, but that also all information about the geometry of the eddies gets lost. This is a very important finding because for that reason the structure of atmospheric turbulent scales of the order of the airfoil chord length and

one or two orders higher is independent of the structure of the source. That means that the exact shape of the thermals has no influence, only their strength has an influence on the level of turbulent kinetic energy k.

The way the kinetic energy of the atmospheric turbulence E_{kin} is distributed over the wave number $k = \left(\frac{2\pi}{L_e}\right)$ fits quite well to Kolmogorov's universal law for turbulent energy distribution

$$E_{kin}(k) = C_T \; \varepsilon^{\frac{2}{3}} \; k^{-\frac{5}{3}} \tag{3.3}$$

wherein C_T is a universal constant and ε is the energy dissipation per unit mass per unit time. The Kolmogorov hypothesis is presented here as it can be found in textbooks like [57]. In a log-log plot of turbulent kinetic energy E_{kin} as function of the wave number k, the decay in the inertial subrange can be easily identified by the characteristic slope of $-\frac{5}{3}$. Since C_T is a constant, the energy dissipation rate ε is sufficient to describe the turbulence intensity in the CBL.

MacCready showed the applicability of this concept through in-flight measurements of turbulent spectra with a sailplane, see [59] for the experimental setup and [60] for the results. The value of C_T using SI-Units is assumed to be 0.15 [33]. When the spectrum represents the longitudinal turbulence (airspeed fluctuations) measured from an aircraft moving at mean airspeed V the spectrum is usually given in terms of the frequency f rather than the wave number $k = \left(\frac{2\pi}{L_e} = \frac{2\pi f}{V}\right)$ [33].

$$E_{kin}(k) = C_T \; V^{\frac{2}{3}} \; \varepsilon^{\frac{2}{3}} \; f^{-\frac{5}{3}} \tag{3.4}$$

In essence, it is important to remember that in atmospheric turbulence not a single length or time-scale is dominating, but all length scales ranging from convective scales of the order of some hundred meters to dissipative scales of the order of millimeters are coexistent and superimposed.

Turbulence can not only be described by energy spectra, also statistical moments can be used. One example is the turbulence intensity level Tu, defined as

$$Tu = \frac{1}{U_\infty} \sqrt{\frac{1}{3}\left(\overline{u'^2} + \overline{v'^2} + \overline{w'^2}\right)}. \tag{3.5}$$

For isotropic turbulence $\left(\overline{u'^2} = \overline{v'^2} = \overline{w'^2}\right)$ equation 3.5 reduces to

$$Tu(u') = \frac{1}{U_\infty}\sqrt{\left(\overline{u'^2}\right)}. \tag{3.6}$$

Riedel and Sitzmann [61] give an overview of in-flight measurements of the atmospheric turbulence intensity in the atmospheric boundary layer as well as the free atmosphere, which were obtained within the framework of different European collaborative flight-test programs. The in-flight measurements have yielded turbulence intensities for the quiescent air atmosphere which are less than 0.05% but the turbulence levels close to an inversion layer or within clouds are significantly higher, see 3.4.

Zanin [62] reports turbulence levels of about 0.3% within a thermal and more than 1% within cumulus clouds. This is consistent with the results of Riedel and Sitzmann [61] since deviations in the numerical value of the turbulence level are also a result of different sampling and filter frequencies. The low frequency but high amplitude fluctuations have the greatest influence on the turbulence level value. Hence, the definition of the filter frequency to split the velocity into a mean velocity and the fluctuations determines the turbulence level value for a given turbulent flow. The filter frequency must be selected carefully and stated together with the turbulence level.

Due to the fact that the turbulence intensity Tu as such holds no information on characteristic length or timescales, Zanin [62] also shows turbulent kinetic energy spectra. A comparison between atmospheric turbulence energy spectra with wind tunnel energy spectra shows significant differences. This leads to the question whether wind tunnel and atmospheric turbulence intensities are comparable in terms of forcing on the airplane's boundary layer. Furthermore, the question arises whether energy spectra are sufficient to describe turbulence, as they are averaged and therefore disregard singular events.

3.2. Theories on the Performance Loss

3.2.1. Increased Drag through Premature Transition

The first theory on performance loss under turbulent conditions assumes an increased friction drag due to premature laminar-turbulent transition. It is therefore only applicable to aircraft with laminar airfoils, or more precisely, aircraft with laminar airfoils and smooth surfaces which do not

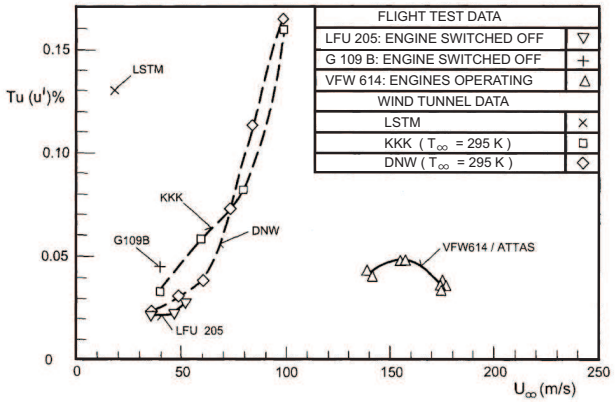

(a) Still air turbulence levels

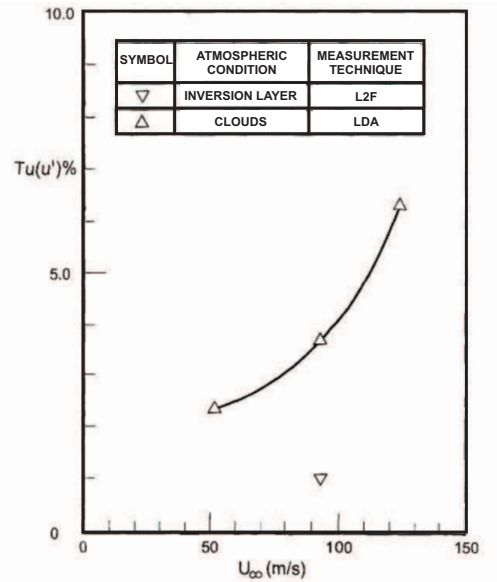

(b) Turbulence levels in clouds and close to inversion layers

Figure 3.4.: Comparison of the turbulence intensity $Tu(u')$ for different meteorological conditions from flight-test data with wind tunnel measurements, from Riedel and Sitzmann [61].

cause transition.

The origin of natural boundary-layer transition lies in free-stream disturbances such as sound and vorticity. Receptivity theory deals with the entrainment of these external disturbances into the boundary layer causing the onset of transition. Therefore, this theory is also referred to as "Receptivity Theory" in the following.

After the stability theory was developed in the early 1930's by Tollmien and Schlichting, an experimental investigation in order to verify the stability theory was performed by Dryden, Schuhbauer and Skramstad [10]. In the course of this they discovered that the transition location is influenced by the free-stream turbulence level, see Figure 3.5.

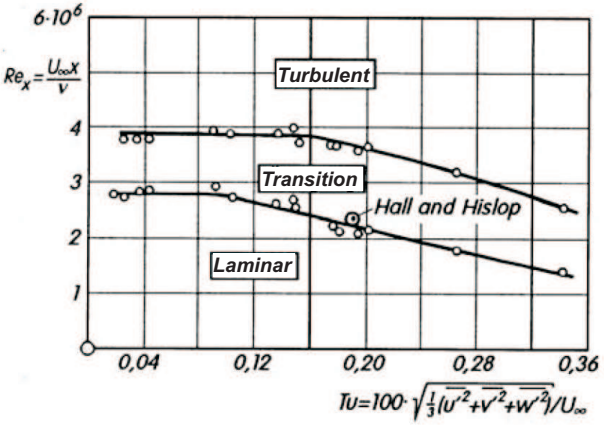

Figure 3.5.: Influence of the turbulence level on the critical Reynolds number of a flat plate flow. Measurements of Schubauer and Skramstad, from [10].

The turbulence levels of about 0.3% within a thermal and more than 1% within cumulus clouds reported by Zanin [62] suggest that premature transition can occur in atmospheric turbulence. Transition location as a function of the turbulence level cannot be calculated from stability theory up to this date. An empirical transition criterion to determine the transition N-factor using the e^n-method is given by Mack [63]:

$$n_{tr} = -8.43 \ - 2.4 \ln Tu. \tag{3.7}$$

In order to identify influencing mechanisms a more detailed look into

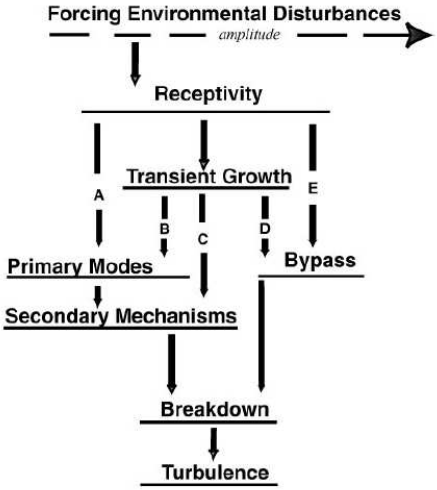

Figure 3.6.:
Paths to turbulence, from Saric et al. [65].

transition theory is necessary. The classical approach in transition research is to divide transition mechanisms in two-dimensional boundary-layer flows into two main classes. The first class is described by the classical evolution of small wavelike instabilities, so-called "Tollmien-Schlichting waves" (TS-waves), which occur in a flow environment with low disturbance levels. The second class, "Bypass Transition", is typically attributed to strong disturbances, for example when cross-flow with unstable cross-flow modes is present, the surface is rough or the free-stream turbulence (FST) is high enough to cause "bypass" of the traditional route. Both scenarios are described in more detail by Kachanov [64] for example.

A more universal approach trying to incorporate the latest results of transition research and reuniting both scenarios by the receptivity concept is given by Saric et al. [65]. The transition process is described qualitatively by so-called "roadmaps to turbulence", see Figure 3.6 for the most important transition scenarios. In the classical approach one had to choose between path A and E.

Upon entering the boundary layer, a wide disturbance spectrum is present, but only a limited number of disturbances conform to the vital conditions (amplitude, frequency and phase) for instability generation and amplification inside the boundary layer. The question which type dominates depends on the base flow conditions as well as on the magni-

tude of the forcing environmental disturbances. Wall curvature (pressure gradient), wall temperature, surface roughness, the flow's Reynolds and Mach numbers may all have an influence on the formation of instabilities and their downstream development.

The parameter regime of the present work gives rise to two possible instability types. Depending on the disturbance environment either exponentially growing wavelike disturbances or low-frequency streaky structures have been detected in wind tunnel experiments, see Saric et al. [65]. While exponentially growing TS-waves typically occur in low ambient disturbance environments, so-called Klebanoff modes are observed under moderate free-stream turbulence (FST) levels ($Tu > 0.5\%$). The latter instability creates streaky boundary-layer structures of fluctuating high and low velocity areas elongated in the base-flow direction. In contrast to the TS-waves, which typically possess frequencies of several hundred Hertz, the streaks resemble stronger fluctuations of only a few Hertz. Bertolotti [2] supposes that a Klebanoff type of transition is more likely than TS-transition in atmospheric turbulence. Whereas most receptivity theories assume no pressure gradient, the influences of the pressure distribution have been investigated theoretically by [66].

While TS-waves could be detected in various free-flight experiments (e.g. Seitz [67]) the Klebanoff modes have only been subject to wind tunnel experiments up to now. Which mechanism is prevalent in flight under elevated turbulence levels is not known to this day [68].

It should be pointed out that receptivity and stability theories both assume a constant pressure distribution. Rapid pressure distribution variations caused by angle of attack oscillations are not considered. The fundamental question arises whether Klebanoff modes lead to premature transition under higher FST levels in free flight or if the loss in aerodynamic performance can be rather attributed to the angle of attack fluctuations. If and how far transition moves upstream for a specific pressure distribution and how this affects viscous drag, must be investigated. This question constitutes one of the main questions of the present study.

3.2.2. Quasi-stationary Lift Effects

Whereas the previous section emphasized viscous drag as cause for the performance degradation, the model presented in the following focuses on lift effects. Hence, it is not exclusively limited to NLF airfoils.

The conventional way to maximize performance of any aerodynamic

design is to define the mission and prescribe the highest and lowest lift coefficient out of it. This design range within the flight envelope is then optimized. Drag is usually minimized only within this design range. Less attention is paid to airfoil behavior outside of this range except for some specific features like stall characteristics and the maximum lift coefficient. In order to improve stall characteristics many NLF airfoils are designed such that at high AoAs beyond the laminar drag bucket, when flow detachment occurs, the lift is not increased further. This gives a more gentle stall behavior compared to a steadily increased lift up to a sudden lift loss.

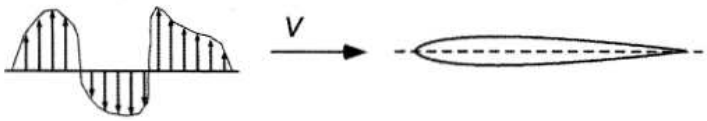

Figure 3.7.: Angle of attack oscillations due to external forcing (gust).

In the real atmosphere, calm air mainly exists outside a convective boundary layer. Within the CBL a flight through up- and downdrafts leads to angle of attack variations. Bernardy [3] measured AoA variations up to $\pm 5°$ from trimmed condition flying a sailplane within a thermal. At low speeds and high lift coefficients respectively, the angle of attack can easily exceed the upper border of design range when encountering these forced oscillations. Hence, the airfoil works outside prescribed design range less efficiently.

A simple approach to investigate flight performance in turbulent air is given by Boermans [1]. First, the equations of motion are set up treating the airplane simplified as a mass point. Then a quasi-steady treatment of the aerodynamic forces is used. Instantaneous AoA values are taken from [3] to calculate instantaneous lift force using the airfoil's steady lift curve. Another assumption in the theory by Boermans is that due to the high lift-to-drag ratio of modern sailplanes, drag changes can be neglected.

For flights at high speeds and low C_L in the linear range of the lift curve, AoA oscillations have no influence on the mean lift because the linear lift range is not exceeded in case of a AoA increase through a gust. At a high stationary C_L values the superposition of an AoA oscillation leads to a different result. A lower AoA decreases C_L linearly whereas

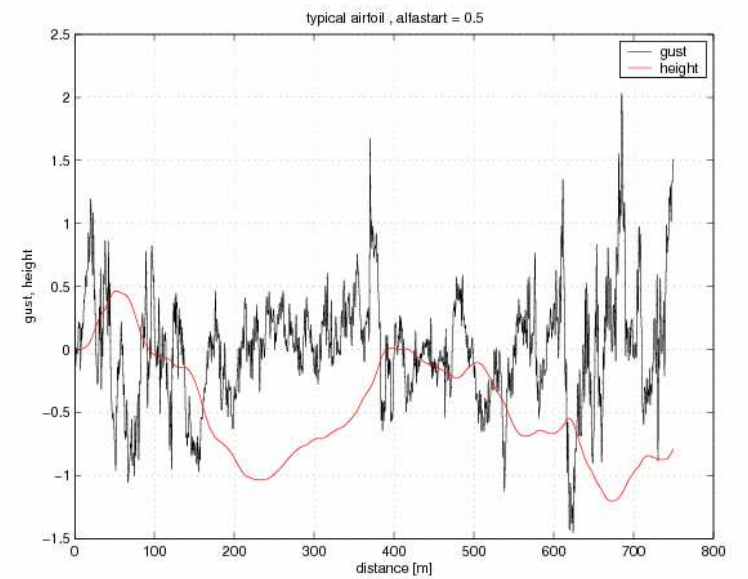

(a) Measured AoA variations and calculated altitude loss for a trimmed lift coefficient $C_L = 1.2$

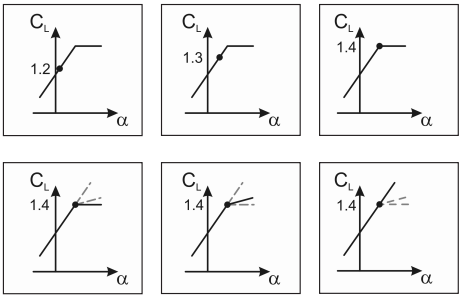

(b) Simplified static lift curves. Upper row: Lift coefficients for different steady flight conditions. Lower row: Different slopes of the lift curve in the non-linear range.

Figure 3.8.: Calculation of altitude loss for a sailplane in slow flight based on simplified lift curve models, lift coefficient for trimmed flight and measured AoA variations within a thermal, from [1].

C_L is not increased for a higher AoAs if the linear range of the lift curve is exceeded. Hence, in average lift is lost in turbulent conditions. The flight trajectory for given AoA oscillations can be computed (Figure 3.8(a)) using different initial conditions and slopes of the lift curve in the nonlinear range (Figure 3.8(b)). Following these assumptions, the shape of the airfoil's static lift curve in the non-linear range dominates sailplane climb performance in gusty conditions.

Neglecting drag, turbulence does not influence performance at low lift coefficients and the theory is not applicable to powered aircraft in cruise flight. Sailplane performance in terms of average speed is negatively affected because time to climb increases, see Figure 2.7 and Equation 2.33.

If the drag is not neglected as assumed by Boermans [1], then quasi-stationary lift effects can also affect cruise flight at low AoAs if the laminar drag bucket is left at the lower end due to AoA oscillations. Additionally the induced drag varies with lift coefficient and there can be an important factor at high lift.

3.2.3. Unsteady Aerodynamic Effects

The previous approach treated unsteady effects in a quasi-stationary way. The unsteadiness of the flow can be described by the reduced frequency

$$k_{red} = \frac{\omega c}{2U_\infty} \tag{3.8}$$

where ω is the circular frequency of the oscillation, c is the chord of the airfoil and U_∞ is the free-stream velocity. According to McCroskey [69] and Leishman [29] the unsteady effects are small for $k_{red} < 0.05$, but can not be neglected for $0.05 < k_{red} < 0.2$. For higher reduced frequencies the unsteady forces begin to dominate the air loads.

Besides the degree of unsteadiness, unsteady aerodynamic effects can be distinguished by the flow conditions at which they occur. For large and rapid changes to high angles of attack at low Reynolds numbers the flow becomes separated and dynamic stall takes place. But unsteady effects also play an important role in attached flow conditions.

Attached Flow

Results for the problem of unsteady airfoils in attached flow conditions have been formulated by, among others, Theodorsen, Wagner and Küssner, a detailed summary is given by Leishman [29]. All of these the-

oretical approaches are based on thin-airfoil theory, hence only lift is considered. Theodorsen's approach describes the problem in the frequency domain. A flat-plate airfoil undergoes harmonic forcing in an incompressible, two-dimensional flow with the airfoil and the shed wake being represented by vortex sheets.

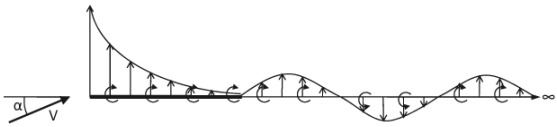

Figure 3.9.: Model of Theodorsen's approach. A thin-plate airfoil is undergoing harmonic forcing. The airfoil and its shed wake are modeled as vortex sheets.

In case of a plunging motion of the airfoil with $h = \overline{h}e^{i\omega t}$ the lift coefficient is given by

$$C_l = \left[2\pi k_{red}\left(iF - G\right) - \pi k_{red}^2\right]\frac{\overline{h}}{b}e^{i\omega t} \tag{3.9}$$

where $b = \frac{1}{2}c$ is the half chord of the airfoil. F and G are part of Theodorsen's function which can be written in terms of Hankel functions as

$$C(k_{red}) = F(k_{red}) + iG(k_{red}) = \frac{H_1^{(2)}(k_{red})}{H_1^{(2)}(k_{red}) + iH_0^{(2)}(k_{red})}. \tag{3.10}$$

A deficit in Theodorsen's approach is that the reduced frequency k_{red} is an ambiguous parameter because it includes the circular frequency of the oscillation ω as well as the free-stream velocity U_∞. Wagner describes the problem in the time domain for a thin airfoil undergoing a transient step change in AoA in incompressible flow. The variation in the lift coefficient for a step change in AoA is given by

$$C_l(t) = \frac{\pi c}{2V}\delta(t) + 2\pi\alpha\phi(s) \tag{3.11}$$

where $2\pi\alpha$ is the steady-state lift coefficient and $\phi(s)$ is Wagner's function with the distance traveled in semi-chords s. One approximation to

the Wagner function is given by Jones.

$$\phi(s) \approx 1.0 - 0.165e^{-0.0455s} - 0.355e^{-0.3s} \tag{3.12}$$

Küssner tackles the problem of finding the transient lift response on a thin airfoil entering a sharp-edged gust. The AoA changes progressively as the airfoil penetrates into the gust whereas in Wagner's approach the AoA changes instantaneously over the whole chord. The lift coefficient is given by

$$C_l(t) = 2\pi \left(\frac{w_0}{V}\right) \psi(s) \tag{3.13}$$

where w_0 is the vertical velocity of the gust and $\psi(s)$ is the Küssner function. One approximation for $\psi(s)$ is given by Sears and Sparks.

$$\psi(s) \approx 1.0 - 0.5e^{-0.13s} - 0.5e^{-1.0s} \tag{3.14}$$

The comparison between lift coefficients calculated with quasi-stationary and with unsteady methods from measured AoA data can prove the validity of a quasi-stationary approach as described before.

Detached Flow

Detachment of the flow takes place when the angle of attack, at which static stall occurs, is exceeded. The stall scenario depends on the magnitude of the AoA oscillation and how far the AoA for maximum steady lift is exceeded. In case of very high AoAs a vortex is generated at the leading edge which detaches and travels over the airfoil, inducing additional lift on it. After it reaches the trailing edge the flow becomes fully separated and dynamic stall occurs. When the angle of attack is small enough the flow reattaches to the airfoil. Due to lags in the separation and reattachment of the flow, large hysteresis effects can be found in the process [69]. Additionally to the lift effects, this scenario is accompanied by a massive drag increase. If dynamic stall effects happen regularly in slow flight, then they have a considerable influence on climb performance.

The case of the separated flow is very complex to model so that most dynamic stall models are semi-empirical. A good summary can be found in Leishman [29]. In contrast to the models for attached flow mentioned before, most empirical models also predict drag.

Regardless of the question if flow detachment occurs through AoA os-

cillations or not, the measurement of the unsteady development of the static pressure distribution around the airfoil is a key element within this project to verify the unsteady effects. Although no accurate pressure drag can be calculated from the pressure distributions if the number of measurement points is to low, typical patterns in the pressure distribution can be observed from such data.

3.3. Critical Analysis of the Existing Theories on Performance Loss

The proposed theories on the performance loss are quite different, so a critical analysis of the existing theories including an estimation of the possible performance degradation is necessary. This critical analysis includes the identification of relevant length scales of atmospheric turbulence related to the different theories.

To distinguish between quasi-stationary and non-stationary AoA oscillations the reduced k_{red} characterizing the degree of unsteadiness of an aerodynamic problem can be used. It is assumed that turbulence is not statistically changed during the short time of the flight through an eddy. In measurements, frozen turbulence is also referred to as Taylor's hypothesis, which allows time series measured at a single point to be interpreted as spatial variations. Using the frozen turbulence hypothesis, Equation 3.8 can be rearranged to solve for the characteristic length scale L of the eddy instead of the angular frequency ω encountered flying through the eddy

$$L = \frac{\pi}{k_{red}} c. \tag{3.15}$$

Using Equation 3.15 the degree of unsteadiness can be expressed in length scales compared to the present airfoil's chord length c.

Quasi-steady	$0 \leq k_{red} < 0.05$	$63\ c < L$
Unsteady	$0.05 \leq k_{red} \leq 0.2$	$16\ c \leq L \leq 63\ c$
Highly unsteady	$0.2 < k_{red}$	$L < 16\ c$

Table 3.2.: Degree of unsteadiness in terms of eddy size compared to chord length.

Table 3.2 shows the degree of unsteadiness not only in terms of reduced frequency as it is typically found in the literature [29] but also in terms of eddy size compared to chord length of the airfoil. In the inertial

subrange of the energy cascade the energy content decreases with eddy size. Therefore, low frequency oscillations, which allow for a quasi-steady treatment, have the biggest amplitudes. High frequency oscillations have only small amplitudes and are rather perturbations. For this reason it is assumed in the following that eddies smaller than the chord length have only an influence on the boundary layer but not in terms of unsteady airfoil motion. Hence, they have little influence on the airfoil pressure distribution.

An unsteady treatment is necessary for eddy sizes between 16 and 63 times the chord length. If the size of the eddy is smaller than the wing span, it cannot influence the entire wing. The G109b has an $\mathcal{AR}$of 16, therefore, the limit where an eddy influences influences only a part of the wing is 16 c. It is a coincidence that highly unsteady fluctuations have only influence on the local lift but not on the entire aircraft. This is also true for other aircraft since $\mathcal{AR}$=16 is a typical value also for other sailplanes.

For the receptivity theory, atmospheric turbulence must contain frequencies capable of forcing the boundary layer directly. Frequencies of TS-waves are assumed to be in range of 500 Hz to 1000 Hz, depending on the flight velocity. Free-stream disturbances in this range are considered potentially dangerous in terms of direct boundary-layer forcing. For a given chord length (c=1.35m) and flight velocity, eddy sizes which result in potential forcing frequencies f are calculated (Table 3.3).

Flight velocity:	$30m/s$	$45m/s$
Eddie size for $f = 500Hz$	$81mm$	$122mm$
Eddie size for $f = 1000Hz$	$41mm$	$61mm$

Table 3.3.: Estimated eddy sizes capable of direct boundary-layer forcing.

Dissipative scales, Equation 3.1, in convective boundary layers of the atmosphere were estimated as $\eta = 2\ mm$ by Batchelor [58] and MacCready [60]. From these estimates it is very likely that in turbulent conditions a large number of eddies capable of forcing laminar-turbulent transition exists. For a better overview, turbulent length scales relevant to the performance loss theories are marked in a schematic diagram of the energy cascade, see Figure 3.10. It has been shown that length scales of atmospheric turbulence relevant to all theories exist in the convective boundary layer. Another important aspect in the critical analysis of

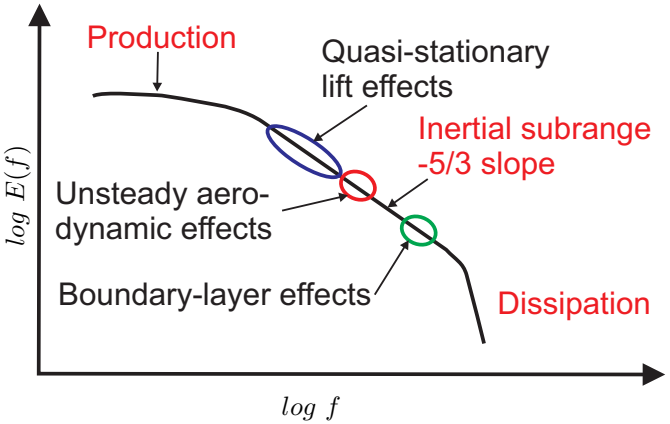

Figure 3.10.: Turbulent energy cascade showing relevant scales with regard to the performance loss theories.

the performance loss theories is to quantify the possible performance degradation in sailplane applications as well as other applications. Soaring UAVs are considered as sailplanes. For the purpose of assessment, three principle flight conditions are examined: slow flight, best glide and high-speed glide.

Two information sources are particularly helpful in the assessment of the performance loss theories. The first source is the drag breakdown for a typical sailplane, see Figure 3.11 for an example. It shows the relative amount of drag for the aircraft components at different lift coefficients or flight velocities respectively. This drag breakdown shows the dominating drag contribution for each lift coefficient and allows an estimation on the influence on the total drag.

The second source is the V-n-Diagram. Figure 3.12 shows a reconstruction of the V-n-Diagram for the G109b for $m = 850kg$ and upward gusts of different speeds. Instead of the certification gust velocities from CS22, typical gust velocities are used to show their influence. The static stall limit is the acceleration caused by the maximum attainable static lift force ($C_{L,max,stat}$). The dynamic stall limit assumes that a dynamic lift coefficient 25% higher than the maximum static lift coefficient is reached before the leading edge vortex separates and the lift breaks down. An additional limit is shown in Figure 3.12, which cannot be found in the certification specification. The limit of the linear range of the lift slope

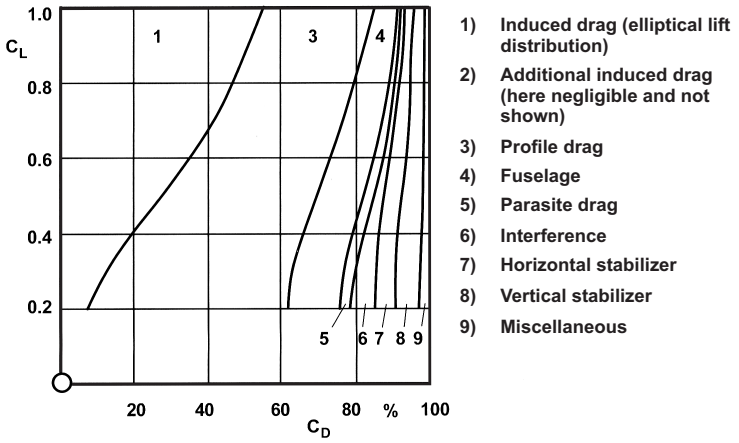

Figure 3.11.: Typical sailplane drag breakdown (SB 8), from Thomas [5].

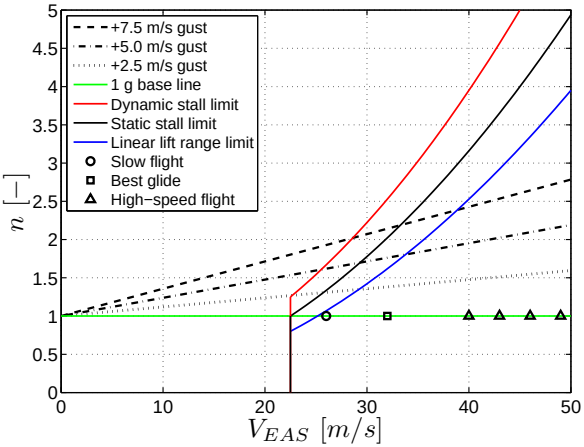

Figure 3.12.: Reconstructed G109b V-n-Diagram for $m = 850kg$ and upward gusts of different speeds.

can be found at roughly 80% of the maximum static lift coefficient. If this limit is exceeded, the theory for quasi-stationary lift effects theory on the performance loss comes into consideration. For a better overview three different flight conditions are examined in the following discussion.

Slow Flight

Slow flight accounts for roughly half of the flight time in soaring applications, in powered applications this flight condition is less important for a typical mission involving a long cruise flight.

At high lift coefficients during slow flight, e.g. circling within a thermal, a glider is operated at the upper end of the airfoil's laminar bucket. In this flight condition induced drag accounts for about half and airfoil drag for about 30% of the total drag. A complete loss of laminar boundary-layer flow with an assumed doubling of airfoil drag would lead to an approximate total drag increase of 30% (Figure 3.11). A complete loss of laminar boundary-layer flow through microscale turbulence is not very likely in this flight condition. The BL on the pressure side is very stable due to a favorable pressure gradient and the amount of laminar BL flow on the suction side is already small due to the suction peak and following adverse pressure gradient.

It seems probable that macroscale turbulence has more impact on performance in this flight condition because it leads to AoA variations which in turn effect lift and drag. Even smaller AoA variations cause a lift increase above the laminar bucket's limit with a strong increase in airfoil drag. Additionally, induced drag is increased with c_l^2. If the linear range of the lift curve is left during AoA oscillations, the average lift is lower than steady lift for the mean AoA. Dynamic stall effects due to AoA oscillations seem possible too in this flight condition.

Best Glide

Best glide, which is roughly in the C_L region of 0.6 or 0.7, is less important in soaring applications, although it is the most important sales argument, because flight speeds are lower while circling and higher in straight flight due to the speed to fly theory. In powered applications this flight condition is much more important because maximum range and endurance are achieved.

In light or moderate turbulence AoA variations are not high enough that the linear range of the lift curve is left or even dynamic stall effects occur. Induced drag is still effected. A drag increase through loss of

laminar BL flow is more probable in this flight condition compared to slow flight because the BL large laminar flow distances are found on the airfoil's suction and pressure side. Due to the less stable pressure gradient on the pressure side, premature transition due to microscale turbulence is more likely.

High-Speed Flight

High-speed flight is the other dominating flight condition in soaring applications and the counterpart to slow flight in cross-country flight. In powered applications it is also an important flight condition because often higher cruise flight speeds are used than the flight speeds for optimal range.

In high-speed flight airfoil drag accounts for more than 50% of the total drag whereas the induced drag is minimal. Additionally, this flight condition is used outside of thermals and the AoA variations are minor compared to the AoA variations within a thermal and the linear lift range limit is not reached. Therefore, it is likely that macroscale turbulence is not the dominating factor in this flight condition.

There is even an adverse pressure gradient on the pressure side of the airfoil with disturbance amplification in the BL starting shortly beyond the leading edge. This is an optimal condition for external forcing through microscale turbulence. Airfoil drag dominates total airplane drag, so every increase in airfoil drag has a significant effect on total drag.

3.4. Possibility of Verification

3.4.1. The Need for In-Flight Experiments

After the different theories on performance loss have been described and critically analyzed, the question remains how these theories can be verified. All common methods in aerodynamic research are considered systematically.

Theoretical Analysis

Theoretical analysis using mathematical models has been used in aerodynamics for a long time and important questions have been answered using this tool. The given problem is very complex. The variety of performance loss theories and the fact that they are based on completely

different scientific approaches, which include unrealistic assumptions, interdicts the sole use of a theoretical analysis. However, in some cases verified theoretical models allow the calculation of additional quantities not accessible in experiments from measured experimental data.

Numerical Simulations

As stated before, the given problem is very complex and the initial inflow conditions for the simulations are not known. Therefore, little data for the validation of numerical simulations exist and appropriate numerical simulations for the verification of the performance loss theories are therefore seldom possible. The high Reynolds numbers also prohibit direct numerical simulations. Nevertheless, numerical simulations are a powerful tool complementing other methods, for example to calculate stationary airfoil pressure distributions and the steady flow field on the wing glove.

Wind Tunnel Experiments

Wind tunnel experiments cannot reproduce exact flight conditions, especially for the case of atmospheric turbulence. Although the wing glove can be mounted in the TU Darmstadt low-speed wind tunnel on a wing section specially designed for this purpose, and the flow velocities are identical to flight conditions, the turbulence spectrum is quite different. Additionally, high frequency AoA oscillations and other unsteady effects cannot be simulated in a conventional wind tunnel. The wind tunnel therefore is not the appropriate method for these unsteady aerodynamic investigations. However, it is a good means for investigation of steady flow conditions, including stall effects at constant AoA, which are not stable flight conditions and therefore not well experimentally accessible in flight. Equipment calibration and system tests are other tasks, which are more easily performed in the wind tunnel compared to flight tests.

In-Flight Experiments

In-flight experiments are the only possible method to investigate the influence of atmospheric turbulence under realistic conditions. The disadvantages of in-flight experiments like complexity, cost and the limitation to certain measurement methods are exceeded by the advantage of realistic conditions by far. Since not all aerodynamic values of interest are accessible in flight, in-flight experiments are supported by all

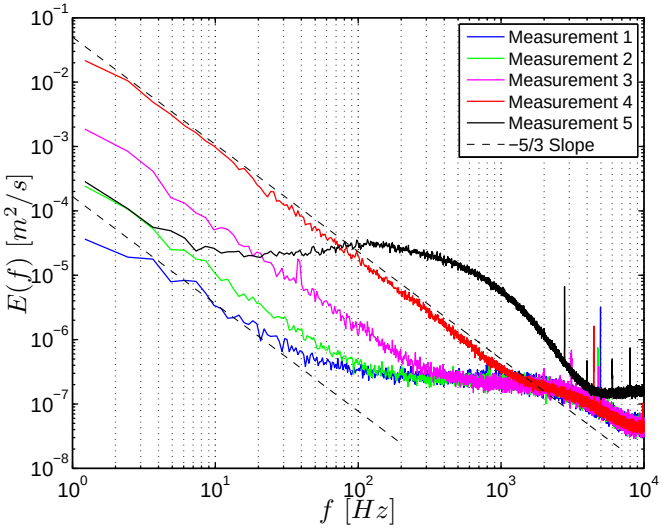

Figure 3.13.: In-flight power spectral densities for different atmospheric conditions in comparison to spectra in the TU Darmstadt low speed wind tunnel at same flow velocity.

the other methods mentioned above for an extensive investigation of the performance loss.

Preliminary Measurements

Preliminary in-flight measurements on atmospheric turbulence are carried out in different meteorological conditions with a boom-mounted single hotwire probe. The primary intention is to obtain a first impression of atmospheric turbulence, compare it with meteorological results and underline the need for in-flight experiments. The other intention of these preliminary measurements is to test the robustness of hotwire probes in the environment of flight operations.

Figure 3.13 shows power spectral densities measured in flight in conditions described in Table 3.4. A single hotwire probe operated in constant temperature mode was used for these measurements and proved to be robust enough to withstand flight tests.

Measurements 1 and 2 show that the turbulence intensity varies in the atmospheric residual layer, see Figure 3.3, although no turbulence is

Measure-ment No.	Description of conditions	Tu [%] (1-10000Hz)
1	Morning, 7500ft, no perceptible turbulence	0.09
2	Morning, 5500ft, no perceptible turbulence	0.11
3	Morning, 2300ft, light turbulence	0.22
4	Afternoon, 6000ft, Flight trough thermal	0.65
5	TU Darmstadt wind tunnel at 30 m/s	0.34

Table 3.4.: Conditions for the measurements shown in Figure 3.13.

perceptible to the pilot. Measurement 3 shows the markedly increased turbulence level at lower altitude. The turbulence caused by first weak thermals in the morning is only barely perceptible to the pilot. Measurement 4 is a flight through a strong thermal in the afternoon. The measured turbulence levels are consistent with other results [61],[62].

For comparison, measurement 5 shows the turbulence spectrum of the TU Darmstadt low-speed wind tunnel at similar flow velocity. Results show that the turbulence spectra of wind tunnel and atmospheric conditions are clearly different although turbulence level are similar in certain conditions. This is a clear proof that investigations on the influence of atmospheric turbulence must be performed in free flight.

3.4.2. Utilization of Experimentally Accessible In-Flight Data

For the verification of the theories on performance loss it is necessary to examine the unsteady inflow conditions and the response on the wing glove simultaneously. Due to the random nature of atmospheric turbulence continuous data logging is required. Furthermore, data must be recorded with a high temporal resolution to verify the receptivity theory.

A large variety of measurement methods may be used for these tasks. An overview can be found in the textbook of Nitsche and Brunn [70]. Due to practical issues, not every method is usable in flying applications. The stringent weight and size requirements of the G109b impose further limitations. A description of methods used for steady measurements is given by Erb [71] or Seitz [67]. In the following the aspects of unsteady measurements are emphasized. Cost of the measurement system also plays an important role.

Inflow Conditions and Characteristic Numbers

Typical inflow conditions must be known for every aerodynamic experiment. These conditions are velocity V_∞, static pressure p_∞, density ρ_∞, temperature T_∞ and dynamic viscosity μ_∞. These values are also used to calculate the similarity numbers Re and M_∞, see Equations 2.17 and 2.18. This is standard for in-flight experiments, for example see Erb [71] or Seitz [67].

A reliable angle of attack measurement is important for this project. The coupling between flight velocity and AoA at given aircraft weight via the horizontal flight condition does not hold for AoA variations due to gusts. Bernardy [3] used a wind vane for AoA measurements on a *ASW19* glider flying in thermals and Hardt [72] compares several methods on the *G109b*. The temporal resolution is limited for all these methods. Defining one chord length as minimum characteristic length for unsteady aerodynamic effects, this translates into a temporal resolution for the AoA measurement 27 milliseconds or a frequency resolution of 37Hz respectively at a flight velocity of 50m/s.

Velocity fluctuations are another important parameter in this work. The question must be answered if inflow disturbances interact with the boundary layer. Therefore fluctuations with the frequency of TS-waves must be measured. With an assumed TS-wave frequency range of 500 - 1000 Hz, multiplied with a safety factor of 1.5 and an additional factor of 2.0 (Nyquist sampling theorem), the minimum sampling frequency for inflow velocity measurements is 3000 Hz. Because the TS-wave frequency range is only an assumption and higher harmonics are not included into this, a higher sampling frequency is desirable.

Basically three experimental methods are capable of the the measurement of unsteady inflow conditions (V', α', β') under free-flight conditions. Flow disturbing methods are boom-mounted hotwire or fast multi-hole probes. A non-disturbing optical method successfully used in flight is LIDAR, which is ruled out from the beginning due to its cost, weight and energy consumption.

Complete hotwire measurement systems including probes and controller are available commercially. The same is true for fast multi-hole probes with pressure transducers close to the orifice and temporal resolutions in the order of some kilohertz. All three velocity components can be measured using a single five-hole probe whereas two standard x-wire probes or one custom-made three-wire probe are the options in hotwire anemometry. The temporal resolution of a hotwire system is

higher compared to a multi-hole probe. Additionally, the resolution of the reading is high for low velocities and decreases with increasing velocity for hotwire anemometry whereas resolution is low at low velocities and increases for the multi-hole probe with velocity.

Due to the fast response and higher resolution the hotwire system is preferred to resolve velocity fluctuations in atmospheric turbulence at the low flight speeds of a motor glider. Therefore, it was chosen for the flight tests and a literature study on system performance and calibration methods as well as extensive wind tunnel testing was conducted by Arnold [73]. Handling, durability and performance under real flight conditions were proved by preliminary flight tests.

Pressure Distribution

The knowledge of the pressure distribution $c_p(x)$ around the glove is important for two reasons. First, the lift coefficient can be calculated from the pressure distribution. This is important to verify the performance loss theories involving lift. Second, the pressure distribution determines the stability of the boundary layer. To measure the influence of AoA variations on the lift, the pressure distribution must be measured with a sampling frequency of the order of the AoA variations.

The correct measurement of the airfoil pressure distribution depends, among other aspects, on the shape of the orifice Nitsche and Brunn [70]. This topic will not be discussed here. Important in this work is the time lag in the unsteady pressure measurements. Schnell [74] designed the pressure measurement system of the previous G109b wing glove using equations from Sinclair and Robins [75]. The dynamic behavior of a pressure line is a first-order transfer function. A laminar pipe flow is assumed in the tube. Fill times t_f for a pressure step from p_1 to p_2 outside the orifice can be calculated for static pressure lines using Equation 3.16:

$$t_f = \frac{128\eta l_e \left(V_{sens} + V_{tube}\right)}{\pi d^4 p_2} ln\left(\frac{p + p_2}{p - p_2} \cdot \frac{p_1 - p_2}{p_1 + p_2}\right) \tag{3.16}$$

The fill time depends on the pressure p at the sensor, which is a certain percentage of p_2, typically 99%. Using reference lengths and diameters, Equation 3.16 can be extended for multiple tube sections [74]. Fill times for exemplary pressure line setups calculated with the equations above are given in Table 3.5. The fill time depends mainly on tube diameter and length. It is almost independent of magnitude of the external pressure

No.	Orifice (⌀; length)	Pressure line (⌀; length)	Fill time 99% [ms]	Frequency [Hz]
1	0.3mm; 0.7mm	1.0mm; 2.0m	113	8.9
2	0.3mm; 0.7mm	1.3mm; 2.0m	71	14
3	0.3mm; 0.7mm	1.0mm; 0.2m	1.9	538
4	1.0mm; 200mm	1.3mm; 1.5m	37.5	26.7

Table 3.5.: Calculated fill times for static pressure lines until reaching 99% of the external pressure step at the sensor.

step. Setups number 1 and 2 describe a typical pressure system used in conjunction with a multi-channel pressure transducer. The orifice is a 0.3mm hole through a layer of glass fibers and a steel tube with a distance of about 0.7mm from the outer surface into the hole. The length of the longest plastic tubes in the glove from the steel tubes to the pressure transducer is assumed with 2 meters. It is clearly visible that the required measurement frequencies for static pressure fluctuations cannot be obtained using long tubes of typical inside diameters.

For unsteady pressure measurements sensors must be located close to the pressure tap. This requirement prescribes the use of miniature pressure transducers. Calculations show that the sensors do not necessarily have to be wall mounted to reach the desired frequency resolution. Setup 3 assumes the same orifice as in setup 1 and 2 but a pressure line only 0.2 meters long. The resultant fill time is in the order of 2 milliseconds corresponding to a frequency of 500 Hz. This is more than 10 times faster compared to the required time. Even if the real frequency response is slower than the calculated one, it is still much faster than required. Therefore this setup can be used for the unsteady pressure measurements without any further validation.

Setup 4 models the pressure lines of a pitot tube rake for wake measurements. The frequency resolution is not high enough to measure very fast changes in airfoil drag. It is sufficient to resolve continuous drag increases through an enduring premature transition if they occur in elevated atmospheric turbulence levels.

Boundary-Layer State and Transition Location

The movement of the transition location x_{tr}/c must be measured with with a sampling frequency of the order of the AoA variations. However, for an observation of the processes in the boundary layer, e.g. TS-waves,

a minimum sampling frequency of 3000 Hz is required.

Different experimental methods for the observation of the processes in the boundary layer have been flight tested on the G109b during the DFG Priority Program "Transition", see Nitsche et al. [76] and [77]. The following methods were tested:

- Hotfilm sensor arrays (RWTH Aachen, TU Darmstadt)
- Piezo foil sensor arrays (TU Berlin)
- Laser Doppler Anemometry (Uni Erlangen)

The requirement of an areal observation in stream-wise and span-wise direction rules out Laser Doppler Anemometry (LDA) from the beginning. The piezo foil technique, see also Peltzer [78], is not commercially available. A hotfilm sensor array in conjunction with a 32 channel CTA system was calibrated by Roth [79] and used in earlier in-flight experiments by Erb [71]. However, this measurement system is not functional anymore and a new measurement system had to be developed and aquired consequently.

Comparable multi-channel CTA systems and hotfilm sensors are available commercially, but their cost is prohibitive at this stage of the project, where the prevailing influence mechanism is unknown. Therefore a more cost effective measuring method is sought, accepting a lower reliability and accuracy. An improved measurement system can be subsequently specified as a result of the flight tests.

The use of wall mounted microphones has been proposed by Nitsche and Brunn [70] as a cost effective method to measure high-frequency pressure fluctuations. This method has successfully been used by Peltzer [78] in preliminary wind tunnel experiments. Due to the fact that the detection of transition plays a critical role, several microphones were tested by Barckmann [80]. Table 3.6 shows the specifications of tested microphones.

The *EM3* microphone shows the best signal-to-noise ratio in ground tests whereas the *PMO4015* is far smaller and still delivers an acceptable signal-to-noise ratio. The other two microphones were not considered for the flight tests because they are much bigger than the *PMO4015* and did not exhibit better signal-to-noise ratios in ground tests.

Preliminary flight tests under non-turbulent conditions show that both microphones are capable of detecting TS-waves and transition. A usable signal is only available when the engine is shut down, the use of microphones is therefore limited to soaring flight [80]. Due to their much

Name	Size [mm] (⌀; H)	Frequency range [Hz]	Sensitivity [dB]	Remarks
EM3	9,7; 10,0	20-18.000	up to -64	3 pin
ECM60	9,7; 7,0	40-14.000	-55 to -67	2 pin
ECM10	6,5; 5,4	50-13.000	-56 to -72	2 pin
PMO-4015PN	4,0; 1,5	20-16.000	-42 ± 3	2 pin

Table 3.6.: Comparison of tested microphones for transition detection, from Barckmann [80].

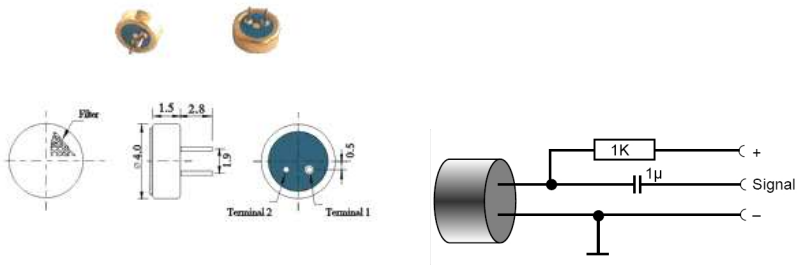

Figure 3.14.: PMO4015 microphone with schematic circuit diagram.

smaller physical size the *PMO4015* microphones are selected for the final sensor array. The height is critical because the microphones should not protrude outside of the glove's laminate and a smaller diameter allows for a denser sensor spacing. Figure 3.14 shows the *PMO4015* microphone and the schematic circuit diagram used for the measurements.

4. Development of a Universal Research Aircraft

The G109b, operated at the Institute of Fluid Mechanics and Aerodynamics, was used in previous research projects. The combination of several features makes a motorized glider an almost ideal platform for in-flight experiments. The aircraft can be used as a glider by simply switching off the engine and selecting the feathered propeller position for measurement flights. Acoustic noise, structural vibrations and electromagnetic disturbances caused by the engine and its ignition are completely avoided and thus can neither interfere with the receptivity and transition processes nor the measurement equipment. Another advantage is the low operating cost compared to larger aircraft. For these reasons the G109b is also used as platform for the in-flight experiments in this project.

4.1. Requirements for a Universal Research Aircraft

Basic requirements for a research aircraft and its equipment can be derived from the theoretical analysis in the previous chapter.

Aerodynamics: The aerodynamic characteristics of the glove should be similar to the characteristics of the airfoil where the performance loss was found.

Structure: The wing glove must not interfere with the aircraft structure.

Sensors: All sensors, which have to be placed directly in the glove, must be small. They have to fit into the installation space between wing surface and the outer skin of the glove.

Measurement equipment: The measurement equipment must be capable of continuous data logging with a data rate of at least 3kHz. In-flow conditions and the effects on the glove must be recorded simultaneously.

Cost: The measurement equipment not only has to fulfill the requirements mentioned above, also the most cost effective measurement methods have to be found.

Besides the basic requirements for a research aircraft, which were set up as a result of the theoretical investigation, additional requirements are imposed for in-flight experiments. Some requirements hold true for all in-flight experiments, others result from the use of the G109b as measurement platform.

Certification: The existing certification must be retained. All changes must be evaluated with regard to airworthiness and certification.

Flying qualities: External equipment must not change the flying qualities of the aircraft. Only an increased total drag is permissable.

Weight: The payload of the G109b is limited. The new equipment must not weigh more than the old equipment. Not only the total weight, but also the weight for certain components must be within the certification limits.

Size: All equipment must fit into the baggage compartment and the equipment pods. A size reduction for the equipment pods is desirable.

Safety: All equipment must must be manufactured to aircraft standards and properly secured. Equipment must not interfere with the aircraft controls nor obstruct evacuation in case of an emergency. This requirement prohibits the use of laptops or exposed wiring in the cockpit.

Energy: Energy supply must be independent from the aircraft's electrical system. Battery capacity (24V, 16Ah) cannot be increased due to weight and size constrains. Therefore, energy consumption must be minimized to achieve an operating time of at least 2 hours.

Reliability: The measurement system must be reliable due to the cost of flight time. No measurement data already obtained should be lost in case of a system failure. The function of the system must be monitored and a malfunction must be reported to the operator.

Maintainability: The measurement equipment must be easily removable from the aircraft for equipment as well as aircraft maintenance.

The development of a research aircraft including a new wing glove and completely new measurement equipment as well as a new instrument panel for additional flight instruments and the flight guidance system is an extraordinary effort, which cannot be justified for only one research project. For this reason the demands of a follow-on project and other future projects involving in-flight experiments, especially active flow control experiments, must be predicted and incorporated into the design from the beginning. This imposes further requirements:

Replaceability of sensors: The selection and placement of sensors is based on theoretical considerations. It is likely that additional or other sensors will be proposed for a follow-on project as result of this work. Therefore, the measurement section of the glove must be interchangeable without destroying the glove.

Modular design: The design of the equipment must be modular for two reasons. First, the ambient air data system and flight guidance system must be independent from the glove. That is important when different gloves are used on the aircraft in the future. Second, measuring instruments must be independent from data acquisition hardware and data acquisition in turn must be independent from PC hardware due to interchangeability and different life cycles.

All these requirements must be taken into account in the design phase. Furthermore, the fulfillment of these requirements must be proved either before first flight or through flight testing. In summary it can be stated that the design fulfills all requirements, as will be shown to in the following sections.

4.2. G109b Motorglider

4.2.1. G109b Motorglider

The G109b is a two-seated, low-wing motor glider developed as a derivative from the G109 by Grob Aircraft. The airframe is constructed from glass and carbon fiber reinforced plastic. Characteristic aerodynamic features are a high aspect ratio wing with an Eppler E580 natural laminar flow airfoil, which is discussed more detailed in chapter 4.3.2. The wing is a simple trapezoid with only slight dihedral, it has no geometric twist. The wing's leading edge is straight with a slight forward sweep (negative sweep) at the quarter chord line. Wing span is 17.4 m with an

area of 19.0 m^2, that results in an $\mathcal{AR}$ of 15.9. At the maximum take-off weight (MTOW) of 850 kg the wing loading is 44.7 kg/m^2. The wing produces enough lift that no lift increasing trailing or leading edge flaps are needed. The only movable parts on the wing are the ailerons and the air brakes on the top side of the wing. Speeds range from the minimum speed V_{S0} of 73 km/h (20.3 m/s) with air brakes retracted to the never exceed speed V_{NE} of 240 km/h (66.7 m/s). Additional technical data, operational limits and procedures can be found in the G109b's Type Certificate Data Sheet (TCDS)[81] and the Approved Flight Manual (AFM) [82].

The aircraft received type approval from the Luftfahrt Bundesamt (LBA) in accordance with certification specification JAR-22 [83] in the Utility Category in 1983. The JAR-22 certification specification is applicable for sailplanes and powered gliders and has less stringent requirements compared with the JAR/CS-23 certification specification for airplanes with a MTOW up to 5700 kg. Nevertheless, there are significant restrictions within the JAR-22 airworthiness standards. Among other requirements, the MTOW must not exceed 850 kg, the stall speed must not exceed 80 km/h and the smallest rate of descent in power-off configuration must not exceed 1.2 m/s. Additionally, flights are restricted to Visual Flight Rules (VFR), flights at night outside the glide range of an airfield, flights under Instrument Flight Rules (IFR) as well as flights into known icing conditions are prohibited.

While the original G109b is powered by 67 kW carbureted, naturally-aspirated Grob 2500 engine, the specific G109b is equipped with 96 kW fuel-injected, turbo-charged Limbach 2400 DT1 engine. This engine is installed in accordance with a Supplemental Type Certificate (STC) held by Korff and it notably improves the take-off, climb and high altitude performance besides reducing fuel consumption.

4.2.2. Modifications

Major alterations are necessary in order to convert the unmodified G109b into a measurement aircraft, which meets the functional specifications defined in chapter 4.1. While minor alterations to an aircraft are possible without documentary proof to the aviation authorities, major alterations in contrast either require a STC or an approved major change. Since the measurement aircraft is unique, the process of approval of major changes on a single aircraft is used instead of the more complicated process of obtaining a STC. The changes can be divided into two categories, per-

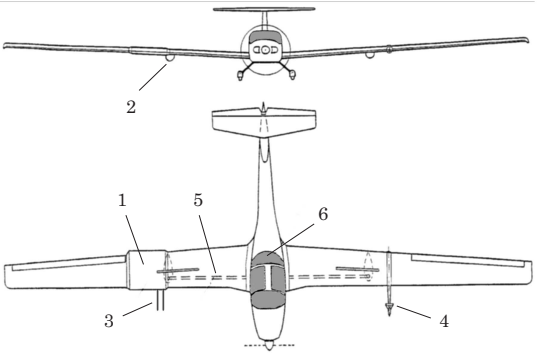

1 Laminar wing glove
2 Pod for measurement equipment (optional)
3 Hot wire probes
4 Air data system
5 Conduit
6 Instrument platform (vibration-isolated)

Figure 4.1.: G109b research aircraft with airframe modifications and additional equipment.

manent modifications to the airframe and non-permanent changes like removable measurement equipment.

Figure 4.1 shows the G109b measurement aircraft with permanent modifications and the removable measurement equipment. Permanent modifications to the airframe are necessary to incorporate additional pressure taps, to attach removable equipment and to accommodate equipment as well as supply lines internally. Except for a new instrument panel, no permanent airframe modifications were added to the existing modifications within the cope of this work. The permanent airframe modifications originate from earlier scientific projects, see Erb [71], thus they will only be discussed briefly.

Most airframe modifications are located on the wing. Each wing has reinforced fastening points for underwing equipment pods and large diameter internal cable ducts from the pods through the wing root into the fuselage. The cable ducts are accessible through removable access panels on the upper as well as on the lower side of both wings. The modifications in the fuselage are fastening points for a vibrations-isolated carrier plate for instrumentation in the baggage compartment. This carrier plate replaces the standard baggage compartment floor and allows for fast and flexible equipment installation, details and limitations can be found in Winterfeld [84]. A new instrument panel was designed in order to accommodate additional flight instruments as well as the new flight guidance system.

While the modified G109b without measurement equipment is visually almost indistinguishable from the standard G109b, the aircraft changes remarkably with the measurement equipment attached. The wing glove on the right wing is the most characteristic modification, which results in an asymmetric state of the symmetric aircraft. Much effort has been spent in the past as well as in the present work in order to design and validate the aerodynamics of a wing glove, which does not change the flight characteristics despite the asymmetric state of the aircraft. Another important feature is the ambient air data system on the left wing, which is completely independent from the aircraft's air data system as well as the sensors in the glove. All modifications are certified, a detailed description and further references are given in the work of Erb [71]. Operational procedures and limitations for flights with measurement equipment can be found in the appendix to the AFM [85].

A crucial limitation is the MTOW of 850 kg. With an airframe empty weight of about 660 kg and an additional equipment weight of about 80 kg, flights with fuel and two persons aboard are practically impossible within the allowable weight limits. An increase in payload is only possible trough an increased MTOW, which is contrary to 850 kg MTOW limit defined in the certification specification JAR/CS22. Consequently, a higher payload cannot be achieved permanently via STC or approved change. An increased MTOW of 950 kg is permitted temporary using a "Permit to Fly" issued by the LBA with additional limitations, which can be found in the "Permit to Fly" and a further appendix to the AFM [86]. The operational limits related to the increased MTOW were calculated by Sommer [87]. For example, these limitations include a reduction of the never exceed speed V_{NE} of 240 km/h to 180 km/h and dictate the use of hard surface runways. On the scale of things, these limitations are much less restricting for in-flight measurements compared to the insufficient payload with the standard MTOW.

Since the prevalent goal in previous projects was the development and in-flight evaluation of different measurement techniques for boundary-layer effects on laminar wings, the existing wing glove and the ambient air data system is not ideally suited to meet the requirements as described in chapter 4.1. Additionally, much of the existing measurement equipment is outdated and unreliable. These circumstances led to the decision to design a new wing glove and new measurement equipment. All design considerations described hereafter are evaluated particularly with regard to the preservation of the existing approval by the LBA.

4.3. Design of a new Wing Glove

4.3.1. Fundamental Options

The wing glove used by Erb [71] was designed to test and compare different measurement techniques for transition research. The required measurement equipment for this project cannot be incorporated into the existing glove. Thus, a new wing glove has to be built. The options are not to change the shape and use the existing mold or to use a different shape, which requires a new mold. In the following the crucial design considerations for the new glove are discussed. Whether the old shape or a a new one is used, the new wing glove must meet four major goals sorted by their importance.

- The glove must hold the measurement equipment without interference with the wing's structure.
- The glove must match the wing section's lift and drag that the flight characteristics of the airplane with the wing glove are similar to the behavior of the clean aircraft in spite of the asymmetric design.
- Airfoil pressure distribution on the glove must be favorable for transition experiments.
- The glove should provide approximately an ideal two-dimensional flow in its center section under free-flight conditions since the investigation of two-dimensional boundary-layer flow is highly desirable for the theoretical explanation and the numerical validation of experimental results.

Considerable research and development effort has been spent on the wing glove. Influences of airfoil, planform, flow fences and equipment pods were investigated in a numerical case study by Barckmann [80]. The old wing glove meets the first two practical requirements and the fourth requirement (2D-flow) on the upper side, but the flow is disturbed on the lower side by a large underwing pod. In addition the airfoil characteristics are not advantageous for the research of natural transition and the influence of atmospheric turbulence as well as for future active flow control experiments. Therefore, it was decided to design a new glove with more advantageous airfoil characteristics.

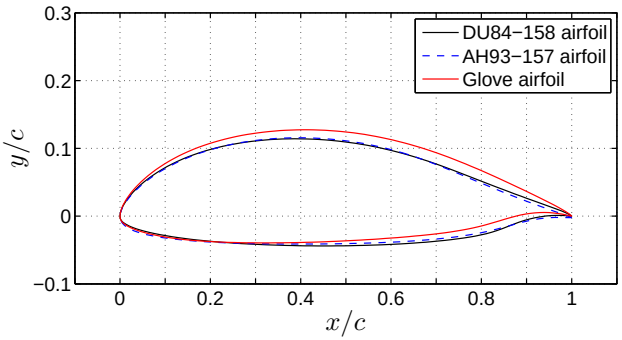

Figure 4.2.: Airfoil comparison, y-axis stretched for clarification.

	Glove airfoil	DU84-158 (original)	E580 (wing)
Thickness	0.16631	0.15776	0.16099
Camber	0.04448	0.03531	0.04067
Radius LE	0.01258	0.01054	0.01017

Table 4.1.: Comparison of thickness, camber and leading edge radius for different airfoils.

4.3.2. Airfoil

The glove airfoil is designed with transition experiments in mind but it is also better suited for a later use in active flow control experiments compared to the old glove airfoil. The airfoil is based on the *DU84-158* airfoil developed by Boermans and used on the *ASW24* sailplane on which the performance loss in turbulence was discovered. Wind tunnel polars for a very similar airfoil, the *Althaus AH93-157* airfoil, can be found in [11]. Figure 4.2 shows a comparison of glove airfoil with the basic airfoils. In comparison to the *DU84-158* airfoil, thickness, camber and trailing edge angle of the glove airfoil are customized, see Table 4.1. This customization is necessary to achieve the desired pressure distributions, see Figure 4.3, and good flying characteristics at the same time. The pressure distributions for the glove airfoil shown in Figure 4.3 are calculated with *xfoil* for three different c_l values at Reynolds and Mach numbers that roughly correspond to in-flight conditions.

Pressure gradients ranging from slightly adverse to zero pressure gradient to favorable can be set on the lower side of the glove depending on

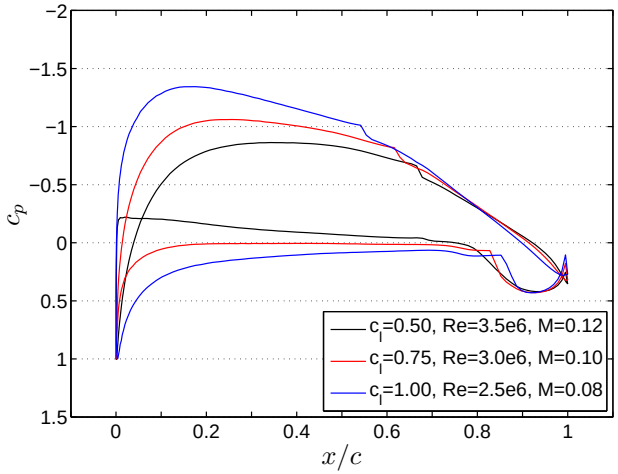

Figure 4.3.: Pressure distributions for glove airfoil for typical c_l values at corresponding Re and Mach numbers. Calculated with *xfoil*.

the flight condition. The airfoil is designed that the local static pressure is equal to ambient pressure p_∞ at a zero pressure gradient in order to enable comparisons with flat plate flows. This is not possible with the unmodified *DU84-158* airfoil where the static pressure is above ambient pressure for a zero pressure gradient. This results in a lower lift coefficient which is desired. The product of chord length with lift coefficient must be equal for glove and wing.

Transition prediction in *xfoil* is based on the semi-empirical N-factor method. The amplification of TS-disturbances amplitudes A compared to the initial disturbance A_0 is expressed by the N-factor ($N = ln(A/A_0)$) and can be seen in Figure 4.4. Laminar-turbulent transition under non-turbulent free-flight conditions is assumed at N=11. The microphones for transition detection are placed with the help of the calculated N-factor distributions. At low AoAs TS-waves are amplified over half of the chord length on the lower side whereas only over a quarter chord on the upper side. The stability of the boundary layer can be varied in a wide range to investigate the influence of external disturbances. A weak amplification of disturbances over a long distance eases observation compared to a strong amplification where the transition process takes place only over a short distance. This makes the glove's lower side the

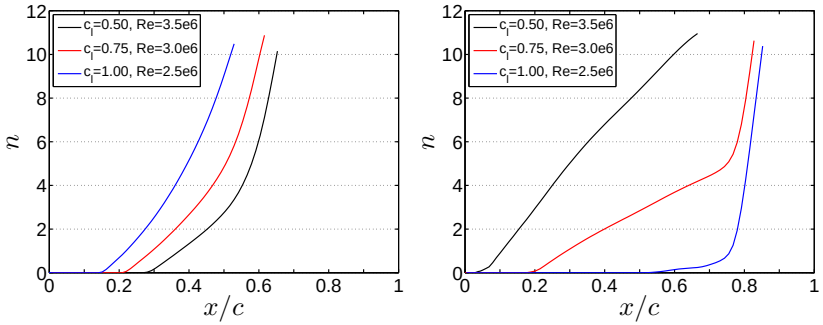

(a) suction side (b) pressure side

Figure 4.4.: Glove airfoil boundary layer N-factors. Calculated with *xfoil*.

preferred one for receptivity investigations.

The pressure distributions on the upper side of the glove are similar to the ones of the original *DU84-158* airfoil. The shape of suction side dominates the behavior of the airfoil at high lift. This is important to verify the performance loss theories involving lift.

4.3.3. Glove Contour

It is possible to fulfill the first three requirements mentioned above (no interference of glove and wing, flying qualities and airfoil pressure distribution) with different glove contours. The mean chord length has to be adapted properly to match lift and drag. An important aspect to ease the understanding of the aerodynamic processes on the glove and to allow for comparison with theory is two-dimensional flow. The G109b wing contour is a simple trapezoid with a taper ratio of 0.55 between wing tip and wing root. Due to the high $\mathcal{R}$ and minor wing sweep, no considerable cross-flow is present at the position of the glove between speed brake and aileron. Two contrary influences of the glove contour on the two-dimensionality of the flow must be weighted up. In contrast to a trapezoid, a rectangular contour delivers a two-dimensional base flow. But the trade off compared to a trapezoid contour is a bigger step between chord length of the glove and the wing on the outboard side. This step in chord length induces cross flow, too.

A numerical case study is the simplest method to consider the in-

fluences of contour as well as external pods and flow fences carefully. Different contours for the glove (rectangular and trapezoid) were investigated in a numerical case study by Barckmann [80]. The findings can be summarized as follows:

Contour is an important factor but the negative influences of a bigger chord length step for a rectangular contour and the negative influences of a taper are almost equal. Rectangular and trapezoid contours are possible.

Equipment pods have a considerable influence on the two-dimensionality of the flow on the lower side of the glove.

Flow fences must be rather large to have a considerable influence on the two-dimensionality of the flow.

Both contours have advantages and disadvantages from the aerodynamical side. Another important factor of non-technical nature, which is not considered in the numerical case study, is the certification issue. The old wing glove had a quadratic footprint with fillets on both sides to intersect the wing contour again. No contour was found that has considerable aerodynamic advantages towards the quadratic footprint. For this reason and with regard to the certification the quadratic footprint with fillets on both sides is also kept for the new wing glove. The quadratic section has a chord length and spanwise elongation of 1.35 m. Fillets of 0.1m on each side result in a total width of 1.55m in spanwise direction for the glove. The positioning of the glove section over the wing section is shown in Figure 4.5. It is visible that there is the possibility to store some equipment in the glove on the lower side aft the wing spar. Storing equipment in this area permits a size reduction or complete omission of the equipment pods. Flow fences are not used because they are either small and have little influence or they are impractical due to their size. A sketch of the glove contour is shown in the following section where the positioning of the measurement equipment is discussed.

4.3.4. Lift Distribution and Flying Qualities

The lift distribution of the wing with the glove and the drag must be similar to the clean wing in order to achieve convenient flying qualities. In fact, the lift of the glove section must be higher compared to the same wing section because of the added weight of the glove. The airfoil and the glove contour have been treated separately in the previous sections.

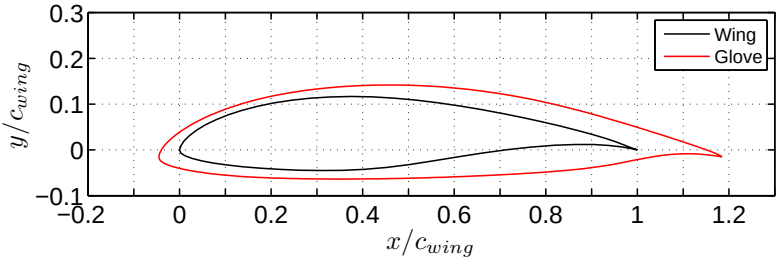

Figure 4.5.: Glove section on wing section.

In the design of the glove, they are coupled because not the local lift coefficients of glove and wing must be equal but the product of local lift coefficients and the particular chord length must be equal.

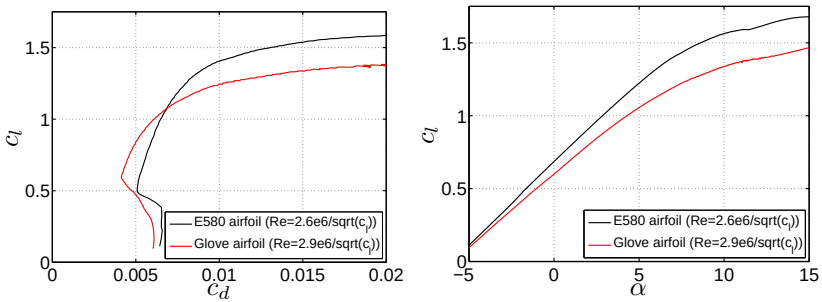

Figure 4.6.: Comparison of glove and wing airfoil polar. Polars calculated with *xfoil*.

Figure 4.6 shows the calculated c_l/c_d and c_l/α polars for the glove and wing airfoil. It is easy to see that the lift at given AoA as well as maximum lift is lower for the glove airfoil. Hence, the chord length of the glove must be increased to compensate for that. Of course this is necessary as the glove must fit over the wing, too. The drag coefficient of the glove airfoil is lower compared to the glove airfoil over a majority of the lift range used in flight. This is crucial to compensate for the greater chord length of the glove. The camber of the glove airfoil has been increased compared to the *DU84-158* airfoil as starting point in the airfoil design, see Table 4.1. This is helpful for a better coincidence

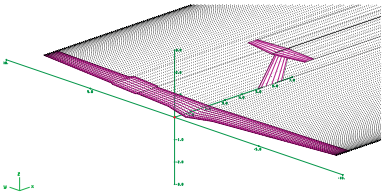

Figure 4.7.: Vortex-Lattice model in AVL of the G109b

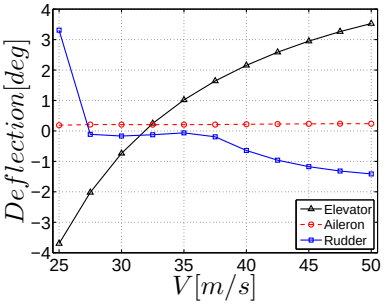

Figure 4.8.: Control surface deflections calculated with AVL.

of the zero lift AoAs for glove and wing airfoil. The lower maximum lift coefficient of the glove airfoil is compensated by the increased local chord length.

The wing's lift distribution and flight mechanics are calculated with the program AVL by Drela. Also the wing bending moments are calculated and compared for the clean aircraft, the old and the new wing glove. AVL is a program for the aerodynamic and flight-dynamic analysis of rigid aircraft of arbitrary configuration. It employs an extended vortex lattice model for the lifting surfaces, together with a slender-body model for fuselages and nacelles. Since the fuselage has little influence on the wing aerodynamics and the flight mechanics of non-slip flight conditions, it is not modeled. The vortex-lattice model of the G109b with the new wing glove in AVL is shown in Figure 4.7.

The G109b AVL model is also used to calculate the control surface deflections for steady, non-slip flight conditions at different airspeeds. A flight mass of $930kg$ is assumed in this model because this is a typical mass with measurement equipment, two average persons and half fuel aboard. A simple airfoil drag polar can be modeled in AVL for the estimation of the wing drag. Due to the asymmetric aircraft configuration this program feature must be used to calculate the rudder deflection. The results are shown in Figure 4.8. The aileron deflection is about $0.2°$ constantly, which is barely noticeable for the pilot. In the middle speed range the required rudder deflection for flight without sideslip is also low. At low and high flight speeds an increased rudder deflection is necessary but still manageable for the pilot. The direction changes from low to

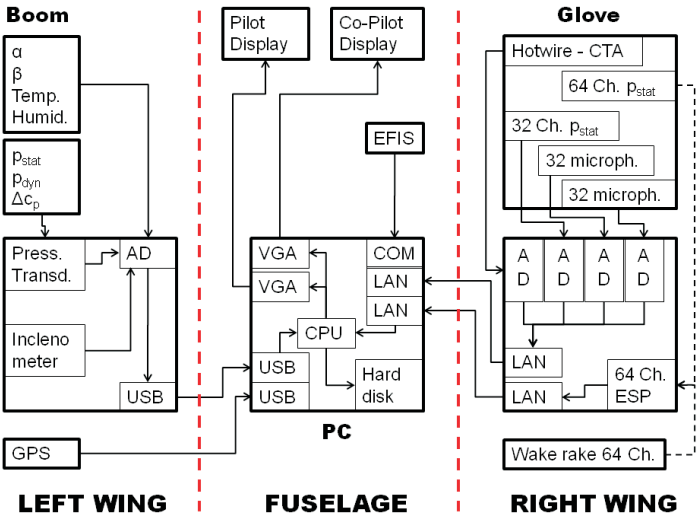

Figure 4.9.: Measurement equipment overview.

high speeds. This can be seen from the airfoil polars and is noticeable in flight. Flight without rudder deflection for drag compensation results in a sideslip angle of about $2 - 3°$.

4.4. Measurement System

4.4.1. Equipment Overview

The measurement system of the G109b research aircraft developed for this project is a highly sophisticated system. The complexity and the vast performance requirements come from the requirement to record a high number of measurement parameters simultaneously and continuously. The measurement system is based on hardware by *National Instruments* and uses the *LabView* software package from *National Instruments*. The development of the system is described in the work of Friedrichs [88]. A functional diagram of the system is given in Figure 4.9. The main components are described in detail in following sections.

4.4.2. Glove

The glove is the most important and most demanding part of the measurement system. The placement of the pressure taps, wall microphones and other equipment is shown in Figure 4.10. The main hardware component is *NI CompactRIO* system consisting of a *cRIO-9074* chassis with four *NI-9205* AD converter modules with 32 channels (single ended) per module. All analog measurement data is converted into digital data in the glove. Therefore an equipment pod containing the *NI CompactRIO* system is essential. However the size is considerably smaller compared to the previous equipment pod and the influence on the flow on the bottom side of the glove is minor. Data is transferred from the *cRIO* to the main PC in the cockpit via a network cable through the cable duct in the wing.

Free-Stream Turbulence, α and β (Unsteady)

Free-stream velocity is measured with high temporal resolution, 6 kHz sampling frequency in the present case, by means of hot wire anemometry. Two orthogonally aligned X-wire probes (*Dantec* $55P61$), operated with a *Dantec* $Multichannel\ CTA$ system, are boom mounted to the wing glove. This setup allows decomposition of the free-stream velocity vector U_∞ into its three components u, v, w and resolves the velocity fluctuations u', v', w'. Free-stream turbulence intensity Tu, energy dissipation rate ε as well as rapid α and β variations are calculated from the X-wire data. The remaining quantities for the calculations, like pressure or temperature, are taken from the air data measurement system.

Airfoil Pressure Distribution (Steady and Unsteady)

The correct measurement of the pressure distribution on the glove surface is a critical point in the measurement campaign because it is required to calculate the lift. Therefore, an important part in the development of the measurement equipment is the pressure measurement system. A new cost effective approach to measure unsteady changes in lift distribution and high frequency pressure fluctuations associated with TS-waves was developed. Instead of using one very expensive sensor (e.g. *Kulite*) per measurement point capable of measuring accurate static pressure, unsteady changes in static pressure as well as pressure fluctuations in the boundary layer (TS-waves), these quantities are measured at the same point with multiple, but less expensive sensors.

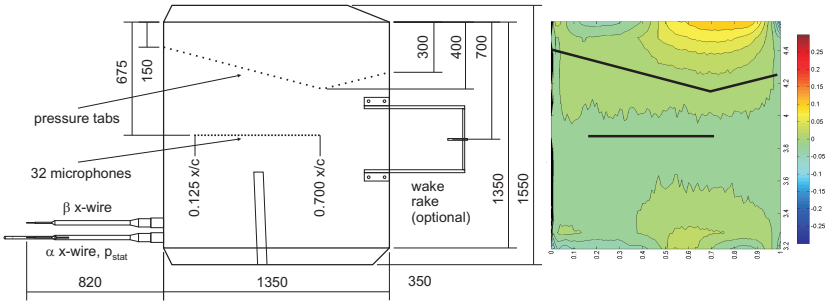

(a) top view

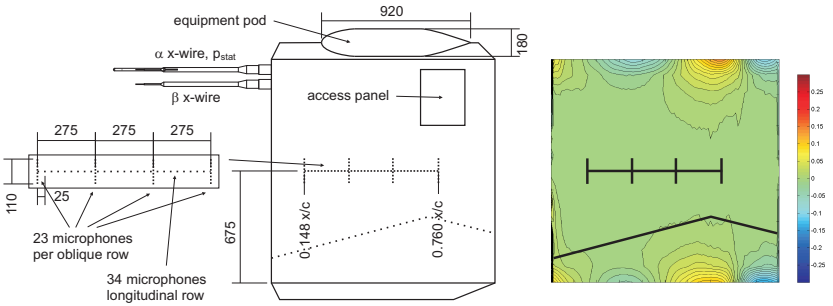

(b) bottom view

Figure 4.10.: Glove views with sensor layout and equipment. Placement of the pressure taps shown in Δc_p distribution from the numerical case study [80].

A 64 channel electronic miniature pressure scanner with a measurement range of $\pm 2.5 PSI$ (*Pressure Systems* $ESP - 64HD$) is used to measure the static pressure distribution precisely for 64 measurement points. A network connection independent from the *cRIO* network is used for the data transfer to the PC in the cockpit. Fill times have been calculated in the previous chapter. Typical tube lengths between orifice and transducer of about 2 m yield inappropriate fill times for unsteady pressure distribution measurements. Thus, an additional set of 32 miniature pressure sensors with a measurement range of $\pm 12.5 mbar$ (*Sensortechnics* $HCL - series$) located in the glove close to the orifice is used to measure fast pressure variations caused by AOA variations. Using a custom calibration instead of the given calibration function,

the measurement accuracy is of the same order as the ESP 64 channel electronic miniature pressure scanner, see Böpple [89]. The 64 channel pressure transducer is also used for an optional wake rake to measure the airfoil drag. A static pressure probe is mounted to the inner hotwire-boom and delivers the required static pressure as reference because all pressure transducers measure a differential pressure.

The results of the numerical case study by Barckmann [80] were taken into account for the placement of the pressure taps. The c_p variation compared to the c_p distribution in the center section is shown aside the glove with a line showing the placement of the pressure taps. A cant of 15 degree is used to prevent erroneous pressure measurements in case a orifice triggers transition. At 0.7 x/c the direction of the cant is turned in order to avoid structural interference with the equipment insert in the middle of the glove. This layout is also favorable with regard to the pressure distribution and gives a more accurate pressure measurement than the arrangement of the pressure taps parallel to chord line.

TS-Waves and Transition Location

An array of electret condenser microphones is used to detect TS-waves and transition location. Their resolution is sufficient to detect the small pressure fluctuations caused by TS-waves. They fully cover the TS-frequency band and their small dimensions allow the allocation of various sensors in a dense array for high spatial resolution. Their positions were determined using the calculated N-factor regimes for different AoAs, see Figure 4.4. Because of the limited number of AD-converter channels, two principle setups are possible. Either the chordwise microphone lines on top and bottom side (32 microphones each) together with the 32 unsteady pressure sensors or the 96 microphones of the 4 spanwise microphone rows for transition experiments in low turbulence environment, see Reeh [90], can be used alternatively.

Airfoil Drag

A wake rake is used for the direct measurement of the airfoil drag. Out of operational considerations the rake is located 0.3 x/c aft the trailing edge of the glove. The use of the wake rake is optional because the same 64 channel electronic miniature pressure scanner ($Pressure\ Systems\ ESP-64HD$) is used for the rake measurements in the wake, which is also used to measure the static pressure distribution. This is non-restricting because the unsteady static pressure sensors and the rake can be used

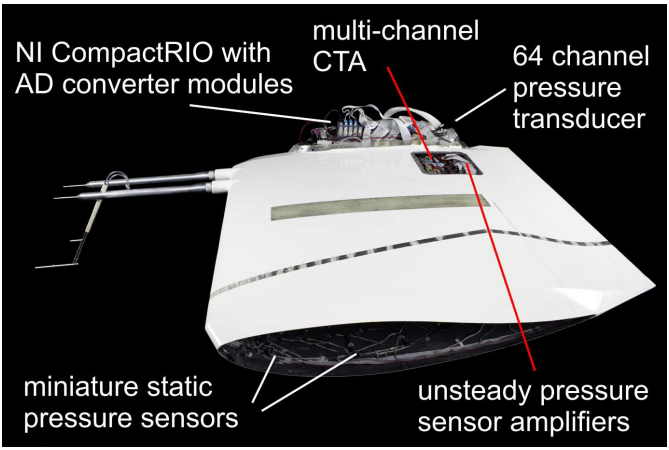

Figure 4.11.: Bottom view of the glove with measurement equipment.

simultaneously.

4.4.3. Air Data Measurement System

Ambient Air Data, α and β (Steady)

A static pressure probe and a pitot tube are used to measure static pressure p_∞ and dynamic pressure p_{dyn}, respectively. Temperature T and relative humidity ϕ are measured to calculate the air density ϱ, the true airspeed U_∞, the dynamic viscosity η and the resulting Reynolds number at the wing glove. The humidity has a considerable influence on the air density and all values calculated from it, e.g. Reynolds number or altitude. Since the relative humidity increases in a thermal from the value at the ground to 100% at condensing level (cumulus cloud base) it cannot be neglected, see Reeh [90] and Böpple [89]. For measurement flights above the temperature inversion (typical for other in-flight transition experiments) the inclusion of the humidity is less important because the relative humidity is low above the inversion. Angle of attack α and side slip angle β are measured with a *Dornier Flight Log*, which is basically a wind vane. The whole air data system is mounted to a boom on the left wing. This part of the air data measurement system is identical to the old system used by Erb [71]. Pressure transducers and the AD-converter are new components located in the equipment pod.

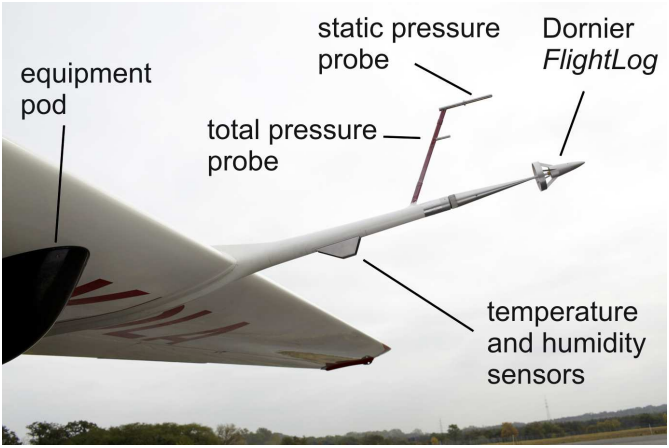

Figure 4.12.: Ambient air data measurement system on the left wing.

In order to avoid temperature errors, the *Setra* pressure transducers for static (*Model* 270) and dynamic pressure (*Model* 239) measurements are kept at constant temperature in a thermostatically controlled box. An inclinometer is used to measure pitch attitude in steady horizontal flight for calibration purpose. All analog data are converted into digital data in the equipment pod using a *NI USB-6259* AD converter. Data is transferred via an USB connection to the PC in the cockpit. A GPS receiver is located on the left wing and data is also transferred via USB cable through the cable duct in the wing to the PC.

4.4.4. Flight Guidance System and Data Storage

All data from the glove and the air data measurement system as well as an electronic flight information system (EFIS) by *Dynon Avionics* are processed in the PC, which is mounted on the vibration isolated instrument platform in the baggage compartment of the G109b. Because a PC with a solid state hard disk is used, a vibration isolation is not mandatory but the platform is kept unchanged because it is practical and certified in its existing form. The necessity of a flight guidance system to obtain constant and reproducible flight conditions has been shown by Erb [71].

An advanced system has been developed by Friedrichs [88] and Reeh [90]. The use of a LCD screen in front of the pilot allows greater flexibility

Figure 4.13.: Cockpit view with flight guidance (left) and operator (right) LCD displays.

compared to an analog device. The goal for a good measurement point under steady conditions is to hold AoA and slip angle as constant as possible. A hairline cross depiction of AoA and slip angle is used to hold these values constant. Velocity, course and altitude are depicted in rollbar style with reference markings left, above and right of the hairline cross. This depiction was chosen because it is similar to the depiction used in modern EFIS systems. The hairline cross depiction for α and β is intuitive for the pilot because it has the same command function as an instrument landing system indicator, α equals the glide slope indication, β equals the locator indication.

The system operator in the right seat has an own LCD touch screen to operate the measurement system. He can set the desired parameter for the flight guidance system, start measurements and monitor if the data stream from each component is received. If a component fails, a warning sign is shown on the operators screen. The data stream from all components of the measurement system is saved as a binary file on the hard disk whereas only ambient air data and the hot-wire data are processed in-flight and used for flight guidance. The entire measurement system is battery powered (24V) and independent from the aircraft power system. The battery is stored in the copilot foot well and lasts for about 2 1/2 hours of operation.

5. Aerodynamic Reference State for Non-turbulent Atmospheric Conditions

The design of the new wing glove is based on theoretical models and numerical simulations. A survey of the base flow in non-turbulent conditions values prior to the investigations under turbulent conditions is essential as baseline data. Furthermore the comparison of the results with the design values proves that one essential part of this work, the design of an airborne measurement system with unique experimental capabilities for multiple applications, was successful. Therefore different methods are used additional to in-flight experiments to obtain information which is not or only hardly obtainable in flight.

5.1. Data Processing and Analysis

5.1.1. Calculation of Relevant Flight Parameters

Measured Variables

The calculation of relevant flight parameters from the measured variables is described in the following. Static pressure p and dynamic pressure p_{dyn} are measured with *SETRA* high precision pressure sensors. In order to avoid temperature errors, these sensors are located in a thermostat box in the equipment pod under the left wing. Temperature T is another basic variable which is measured directly in the flow.

The influence of the humidity φ on the ambient quantities has been investigated by Reeh [90] and Böpple [89]. The relative humidity φ can be defined as the ratio between the partial pressure of the vapor in humid air and the partial pressure of fully saturated air.

$$\varphi = \frac{p_{vap}}{p_{sat}} \tag{5.1}$$

Dalton's law states that the total pressure exerted by a gaseous mixture is equal to the sum of the partial pressures of each individual component

in a gas mixture.

$$p = \sum_i p_i = p_{vap} + p_{dry} = \rho_{hum} R_{hum} T = R_{hum} T \sum_i \rho_i \tag{5.2}$$

A semi-empirical procedure procedure is used to calculate the partial pressure of water vapor. The humidity is included into the calculation of the flight parameters.

Air Density

The air density is calculated using the ideal gas law. Instead of using the gas constant R for dry air, the gas constant for humid air R_{hum} is calculated for the actual humidity.

$$\rho_{hum} = \frac{p}{R_{hum} T} \tag{5.3}$$

For simplicity, air density is referred to as ρ only in the following.

Viscosity

Sutherland's formula is used to derive dynamic viscosity μ of an ideal gas as function the temperature T.

$$\mu = \frac{\beta_s T^{3/2}}{T + S} \tag{5.4}$$

Herein β_s and S are *Sutherland's constants* which are determined empirically for each gas.

The kinematic viscosity ν is given by:

$$\nu = \frac{\mu}{\rho} \tag{5.5}$$

Tabulated values of μ and ν also can be found in the definition of the Standard Atmosphere [6].

Velocity

For the calculation of the flight velocity, Equation 2.7 (dynamic pressure definition) is rearranged to solve for the velocity. Different velocities are commonly used in aviation. The true airspeed V_{TAS} is calculated using

the actual air density ρ.

$$V_{TAS} = \sqrt{\frac{2q}{\rho}} \tag{5.6}$$

The calibrated airspeed

$$V_{CAS} = \sqrt{\frac{2q}{\rho_0}} \tag{5.7}$$

with

$$\rho_0 = 1.225 kg/m^3.$$

is calculated using the Standard Atmosphere's air density at sea level ρ_0.

For a given aircraft weight, AoA is coupled with the dynamic pressure and therefore with the calibrated airspeed independent from the altitude. Hence, airspeed is referred to as calibrated airspeed in the following, is not otherwise denoted. For completeness the indicated airspeed V_{IAS} is mentioned here, which is the airspeed reeding on the airspeed indicator. The difference to the calibrated airspeed is the instrument error of the airspeed indicator. This error is not present in the ambient air data system since the complete measurement chain from the sensor to the digital data is calibrated.

Reynolds and Mach Number

Reynolds and Mach numbers are calculated using Equations 2.17 and 2.18, respectively. For the calculation of the Reynolds number, the chord length of the glove (1.35m) is used as reference length.

Altitude

The measured static pressure is the basis for altitude calculations since the hydrostatic pressure varies with the altitude.

$$H - H_{ref} = \frac{T_{ref}}{\beta_{Trop}} \left(\left(\frac{p}{p_{ref}} \right)^{-\left(\frac{\beta_{Trop} R_{air}}{g} \right)} - 1 \right) \tag{5.8}$$

The derivation of Equation 5.8 can be found for example in [4]. This equation assumes a constant temperature lapse rate which is true for the troposphere up to the tropopause with some deviations in certain weather conditions, see also 3.1.

Different altimeter settings with different reference quantities are used in aviation. In this work the reference quantities shown in Table 5.1 are used, hence all altitudes are pressure altitudes.

Constant	Value	Dimension	Description
g	9.80665	m/s^2	acceleration due to gravity
ρ_{ref}	1.225	kg/m^3	air density at SL
R_{air}	287.053	J/kg K	gas constant
T_{ref}	288.15	K	temperature at SL
p_{ref}	101325	Pa	static pressure at SL
T_{ref}	288.15	K	temperature at SL
H_{ref}	0	m	reference altitude = SL
β_{Trop}	-0.00065	K	temp. lapse rate, Troposphere

Table 5.1.: Reference quantities for altitude calculations, from [6].

5.1.2. Hotwires

Velocity and Angle of Attack

Hotwires are operated at constant temperature, which means at constant wire resistance. Because the heat flow from the wire to the fluid depends on the flow velocity, electrical power depends on the flow velocity too. *King's law* relates the voltage at the measuring bridge E_b to the flow velocity U

$$E_b^2 = A + B\ U_{\text{eff}}^n \tag{5.9}$$

where A,B and n are calibration coefficients. The complete derivation can be found for example in the textbook of Bruun [91]. Within the scope of the work, different calibration methods for hotwires have been investigated by Arnold [73]. Due to the accuracy and simplicity and effective speed method is used.

$$U_{\text{eff}} = \tilde{V} \cdot f\left(\alpha\right) \tag{5.10}$$

The effective speed U_{eff} is component of the flow velocity $\tilde{V}$, which is perpendicular to the wire. Different angular calibration functions are reviewed by Bruun [91]. The cosine law (Equation 5.11) is used as angular calibration function in this work.

$$f(\alpha) = \cos\alpha \tag{5.11}$$

Using two wires (x-wire probe) the flow velocity $\tilde{V}$ and the flow angle θ can be calculated.

$$U_{\text{eff},1} = \tilde{V} \cos^m (\overline{\alpha}_1 + \theta) \tag{5.12}$$

$$U_{\text{eff},2} = \tilde{V} \cos^m (\overline{\alpha}_2 - \theta) \tag{5.13}$$

Therefore Equations 5.12 and 5.13 are inserted in each case into Equation 5.9 and a system of two equations with two unknowns is solved.

For an ideal x-wire probe the angles between the wires and the probe's center axis($\overline{\alpha}_1$ and $\overline{\alpha}_2$), which should be aligned with the main flow direction, are $\pm 45°$. Due to manufacturing inaccuracies the wire angles differ up to 5° from the ideal 45° angle. This is taken into account in the calibration of the probe and improves the accuracy of the angular calibration considerably. Arnold [73] showed a total calibration error of less than 0.3° for $\theta = \pm 5°$ and an error of about 1° for $\theta = \pm 10°$ if $\overline{\alpha}$ is not corrected and ideal $\overline{\alpha} = \pm 45°$ are used. The correction of $\overline{\alpha}_1$ and $\overline{\alpha}_2$ leads to an error of less than 0.3° for $\theta = \pm 15°$.

The voltage at the measuring bridge E_b for a given flow velocity U depends on the flow temperature T. If the flow temperature $T_{fl,m}$ differs from the flow temperature during the calibration $T_{fl,0}$, the measured bridge voltage must be corrected before the velocity is calculated using the calibration function. The corrected bridge voltage is

$$E^2_{b,\text{kor}} = E^2_{b,m} \cdot K_{\Delta T} \tag{5.14}$$

where

$$K_{\Delta T} = \left(\frac{T_{w,0} - T_{fl,0}}{T_{w,m} - T_{fl,m}} \right) \tag{5.15}$$

is the correction factor due to temperature differences. Errors in the velocity measurements due to temperature, pressure and viscosity changes with altitude together with long-term drift cannot be corrected analytically if the ambient conditions vary significantly from the calibration conditions. Errors in the velocity measurements were in the order of 15% whereas the effect on the AoA measurement is minor since both wires are affected in the same way. For the correction of the velocity measurement a linear correction factor K_V is used.

$$\tilde{V}_{\text{cor}} = \tilde{V}_m \cdot K_V \tag{5.16}$$

The correction factor K_V is the ratio of the mean values of $\tilde{V}_m$ and

V_{TAS} from the ambient air data system. K_V is calculated for each measurement. Are more detailed description is given in Appendix B.

Turbulence Level

Turbulence in the inertial subrange of the energy cascade is assumed to be isotropic and only two velocity components of the flow are measured. Hence, the turbulence intensity level for isotropic turbulence $Tu(u')$ (Equation 3.6) is calculated from the hotwire velocity data. For simplicity, it is referred to as turbulence level Tu in the following.

The airspeed over a hole measurement is not constant, deviations from the average speed are considerably. Therefore the magnitude of the turbulence level strongly depends on the partitioning of the flow velocity into a mean value U_∞ and the fluctuations $\overline{u'^2}$. The time interval or filter frequency respectively to calculate the mean flow velocity is given in each measurement.

Energy Dissipation Rate

The energy dissipation rate has been shown to be a good measure for the strength of atmospheric turbulence independent from specific aircraft characteristics[33]. An energy spectra is calculated from the hotwire velocity data. The energy spectrum is estimated once a second. At a sampling frequency of 6000 Hz this yields a frequency resolution of 0.75 Hz up to a maximum frequency of 3000 Hz (Nyquist frequency). Knowing the energy level for each frequency and the flight velocity, the energy dissipation rate is calculated using Equation 3.4, which is rewritten to solve for ε.

5.1.3. Lift and Drag Coefficients

Local Coefficients - Airfoil

Local lift coefficient for the glove airfoil is determined using the measured airfoil static pressure distributions. The normal component per unit span N' of the aerodynamic force R is determined by integration of the pressure and viscous forces around the airfoil[8]:

$$N' = -\int_{LE}^{TE} (p_u \cos\theta + \tau_u \sin\theta)\,\mathrm{d}s_u + \int_{LE}^{TE} (p_l \cos\theta - \tau_l \sin\theta)\,\mathrm{d}s_l \tag{5.17}$$

Assuming a negligible effect of the viscous drag on lift, Equation 5.17 reduces to

$$N' = -\int_{LE}^{TE} (p_u \cos\theta)\, \mathrm{d}s_u + \int_{LE}^{TE} (p_l \cos\theta)\, \mathrm{d}s_l \tag{5.18}$$

Pressure on the upper side of the airfoil p_u produces a force directed downwards whereas pressure on the lower side p_l produces an upward lift force. Since pressure acts perpendicular to the surface, which has the angle θ relative to the chord line, only the component perpendicular to the chord line is integrated. The pressure drag can be derived integrating the tangential component. Whereas the normal component delivers accurate results with the limited number of measurement points, the number of measurement points is not sufficient to deliver accurate results for the tangential component. Hence, the pressure drag is not calculated.

Neglecting the influence of the drag, the lift coefficient can be written as:

$$c_l \approx c_n \cos\alpha = \frac{N'}{qc} \cos\alpha \tag{5.19}$$

Airfoil lift coefficients c_l shown in the following are determined this way. Comparisons between the lift coefficients calculated from the 64 measurement points of the *ESP* pressure transducer and the 32 unsteady pressure sensors show a good agreement.

Airfoil drag is calculated by integration of the momentum deficit over the wake of the airfoil.

$$c_d = \frac{2}{c} \int_W \frac{u}{U_\infty} \left(1 - \frac{u}{U_\infty}\right) \mathrm{d}y. \tag{5.20}$$

Using the *Bernoulli equation* the momentum deficit can also be expressed in terms of pressures instead of velocities:

$$c_d = \frac{2}{c} \int_W \sqrt{\frac{p_t - p_\infty}{q_\infty}} \left(1 - \sqrt{\frac{p_t - p_\infty}{q_\infty}}\right) \mathrm{d}y. \tag{5.21}$$

The pressures are measured using a pitot-tube wake rake. A basic assumption is that the wake is measured far enough behind the airfoil so that the static pressure is not influenced by the near field of the airfoil any more and is equal to ambient pressure p_∞. This assumption is ful-

filled more than 0.7c beyond the trailing edge of the airfoil, see Goett [92].

If the wake is measured closer to the trailing edge, the local static pressure must be taken into account. Assuming energy conservation along the stream line from narrow field to the far field, Equation 5.21 can be rewritten:

$$c_d = \frac{2}{c} \int_W \sqrt{\frac{p_t - p}{q_\infty}} \left(1 - \sqrt{\frac{p_t - p_\infty}{q_\infty}} \right) \mathrm{d}y. \tag{5.22}$$

In this equation also the static pressure must be measured. According to Barlow et al. [93] the measurement of the static pressure in three points and averaging the static pressure is sufficient. This procedure is used to analyze the wake measurements. The static pressure at the locations is taken from the CFD simulations by Schulze [94] because they have not been measured.

Global Coefficients - Airplane

The airplane speed polar can be calculated from the drag polar[5]. The flight velocity V as function of the lift coefficient, air density and wing loading follows from the horizontal flight condition (Equation 2.1):

$$V = \frac{1}{\sqrt{C_L}} \sqrt{\frac{2}{\rho} \frac{W}{S}} \tag{5.23}$$

The sink rate in glide

$$V_S = \frac{C_D}{C_L^{3/2}} \sqrt{\frac{2}{\rho} \frac{W}{S}} \tag{5.24}$$

depends also on the drag coefficient.

In turn, the global airplane lift and drag polar can be calculated from the measured airplane speed polar. This drag polar can be further broken down into its components because the induced drag can be calculated analytically (Equation 2.31).

5.1.4. Partially Automated Data Processing Software

The continuous recording of measurement data with a high sampling rate produces a large amount of measurement data. A partially auto-

mated data processing software written in *Matlab* has been developed by Loosmann [95] to deal with the large data files.

First, the text files are read, data is then converted into a *Matlab* format to improve computational performance. Second, raw data is converted into physical quantities using calibration functions. Third, an overview of ambient and GPS data is plotted. Now the measurement data are searched for relevant events manually.

After relevant events have been identified, the software allows further processing of relevant data like filtering, calculation of dimensionless coefficients and plotting of further data.

5.2. Wind Tunnel Results

Flow Field

The wind tunnel is used to investigate the flow field on the glove, the accuracy of the pressure measurement system and the dimensionless coefficients of the airfoil. Figure 5.1 shows the glove on a wing section in the 2.2 by 2.9 meter test section of the TU Darmstadt low-speed wind tunnel. This wing section was designed specially for this purpose and the hole flight range (AoA and dynamic pressure) can be reproduced. The boundary-layer effects of the wind tunnel walls are limited to the outer parts of the wing section and do not influence the glove. Especially at high AoAs the blocking of the test section is markedly and must be considered.

Erb [71] used tufts and a camera on a tripod for an in-flight investigation of the flow field of the previous glove. Because only the upper side of the glove is accessible in flight (without a chase plane) and the influence of the equipment pod on the lower side remains unclear, the flow field on the new glove is studied in the wind tunnel.

One important result of the tuft studies is that the center section of the wing glove is not effected by three-dimensional effects from the edges of the glove. The extent of the unaffected region with two-dimensional flow on the suction side decreases with increasing angle of attack. Even at high angles of attack, the cross flow at the position of the orifices for the pressure measurements is insignificant. Hence, the pressure measurements outside the center reproduce the pressure distribution in the center of the glove well.

The influence of the booms for the hotwire measurements on the flow field was only considered by simple geometric assumptions. Also in this

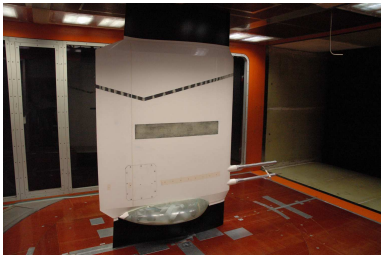

Figure 5.1.: Glove mounted on a wing section for experiments in the TU Darmstadt wind tunnel.

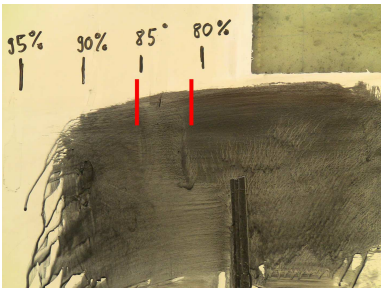

Figure 5.2.: Laminar separation bubble on the bottom side of the glove with partial tripping.

case the influence of the booms on the flow field is most critical on the pressure side at high AoAs. The booms were not considered in the numerical case study in the preliminary design phase [80]. Flow field visualizations with tufts and oil flow pictures prove that the wakes of the booms do not influence the flow field in the measurement section in the center of the wing.

A displacement effect of the equipment pods and a three-dimensionality of the flow has been shown in the numerical case study and an elimination of the pod has been proposed[80]. Due to the requirement to convert analog signals into digital data close to the sensors the pod could not be eliminated, only reduced in all dimensions, especially the spanwise width. Tuft investigations show the displacement effect of the pod clearly. This effect is only visible for less than the half way from the pod to the measurement section, hence the measurement section is not effected by the equipment pod.

Laminar Separation Bubble

A laminar separation bubble associated with a drag increase of roughly 15% was predicted on the pressure side by *xfoil* in the airfoil design. Depending on AoA and Reynolds number the separation was predicted starting at 0.8 to 0.82 x/c. Oil flow visualizations show the separation bubble with reverse flow starting at 0.81 to 0.82 x/c and reattachment at 0.85 to 0.87 x/c. Figure 5.2 shows the detachment and reattachment of

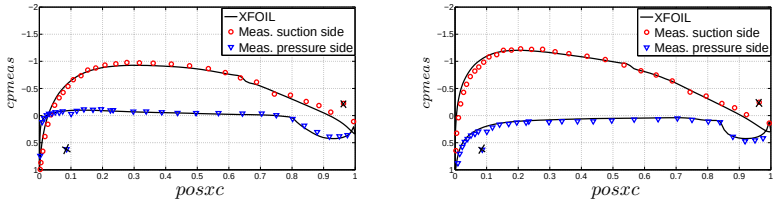

(a) $\alpha = 0.5deg$ (b) $\alpha = 3.0deg$

Figure 5.3.: Comparison of pressure distributions measured in the wind tunnel at $V = 30m/s$ with *xfoil* calculations.

the laminar separation bubble as well as the prevention of a separation bubble through boundary-layer tripping (lower half of the picture) at 0.78 x/c for an AoA of 3 degrees. Consequently a zig-zag tape, which is also used on the original *DU84-158* airfoil was attached to the glove at 0.78 x/c for the in-flight experiments.

Pressure distribution

Airfoil pressure distributions are measured in the wind tunnel using the ESP 64 channel pressure transducer. Figure 5.3 shows measured pressure distributions at a velocity of 30 m/s for two exemplary AoAs in comparison to *xfoil* calculations, see also [89].

The measurements are in good agreement with the pressure distributions calculated with *xfoil* in the design phase. Except for variations due to some broken sensors, data scatter is only minor. It is visible that the goals of the design, the possibility of changing the pressure gradient from adverse to favorable at ambient pressure levels on the bottom side, are met. At high AoAs the agreement is not as perfect as in the case of low AoA. The reason is the increased blocking of the test section and the wall effects on the pressure distributions.

The presence of a laminar separation bubble without boundary-layer tripping can be seen in the pressure distributions in Figure 5.3, which were obtained before the zig-zag tape was applied. A laminar separation bubble on the rear section of the bottom side at the concave curvature develops as the boundary layer becomes more stable with increasing angle of attack. At an AoA of 0.5 degrees transition occurs in the area of the concave curvature and the turbulent boundary layer is able to follow this curvature at 0.8 x/c without detachment. At an AoA of 3 degrees the

boundary layer is stable and separates at 0.8 x/c. Reattachment takes place at 0.85 x/c, a sharp bend in the pressure distribution can be seen in the measurements as well as calculations. This indicates that *xfoil* is capable of calculating laminar separation bubbles. Other measurements with boundary-layer tripping also show a good agreement in the area of the concave curvature with attached flow.

Wake Measurements

The wake rake used for the in-flight experiments is also used in the wind tunnel to measure the airfoil drag and calculate the steady airfoil polar. High angles of attack not obtainable in steady horizontal flight are also measured to investigate the airfoil behavior at high lift and with massive separation on the suction side.

Steady Airfoil Polar

A lift and drag polar for steady AoAs is calculated from the pressure distribution and wake rake measurements. See also Chapter A for the angle of attack definitions. The results are shown together with the results from the flight tests.

5.3. Computational Results

To study the complete flow field around the glove experimentally, elaborate measurements in the wind tunnel are necessary, for example using optical measurement methods. This is extremely time-consuming and also not practical since a black full surface is required for optical measurements whereas the glove is painted white and then polished due to flight requirements. The flow visualization using tufts in the wind tunnel showed that there is no significant influence of the glove edges, booms and equipment pod on the center section. Less significant but still noticeable influences cannot be ruled out with tuft visualization though.

Numerical simulations using commercial software (CFX) are a feasible way to provide a better understanding and quantification of the flow field around the glove in steady conditions. Complementary to the experiments they provide valuable information difficult to obtain otherwise. Two principal issues are addressed with the numerical computations. The first is the influence of the external attachments and the edges on the flow in the center section. This requires high resolution of details

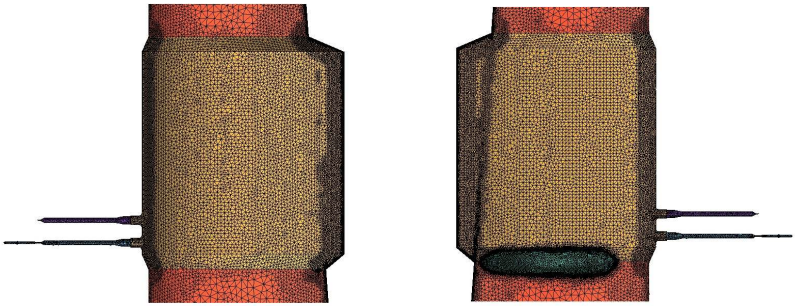

(a) suction side (b) pressure side

Figure 5.4.: Surface mesh of the wing glove.

but only the glove and a section of the wing around the wing has to be modeled. The other issue is the influence of the flow field on the flow quantities at the respective measurement positions. If no separation is expected, a potential flow calculation is sufficient but the whole wing must be modeled. Since the computational resources do not allow to use a high near-wall resolution for the entire wing, two different meshes are used.

The geometry of the glove has already been modeled and different meshes have been generated in the numerical case study [80]. One outcome of this study is that the fuselage blocking effect on the wing glove can be neglected. A solid wall boundary condition at the wing root saves the computational effort to model the fuselage. In this study only one angle of attack has been examined and neither the booms nor the equipment pod was included. Therefore the CAD model of the glove geometry has been updated after construction and details were added by Schulze [94]. The two new meshes for the wing section with the glove (5.5 million cells) and the whole wing outboard the wing fuselage junction (10.7 million cells) incorporate the geometry updates. The detailed mesh for the wing section with the glove is shown in Figure 5.4.

Detailed Glove Studies

Calculations with the detailed mesh are performed for angles of attack which are typical for the flight conditions during the measurements. These angles of attack are 0°, 3° and 6° where the latter case is the most critical one. Figure 5.5 shows the static pressure distribution around the

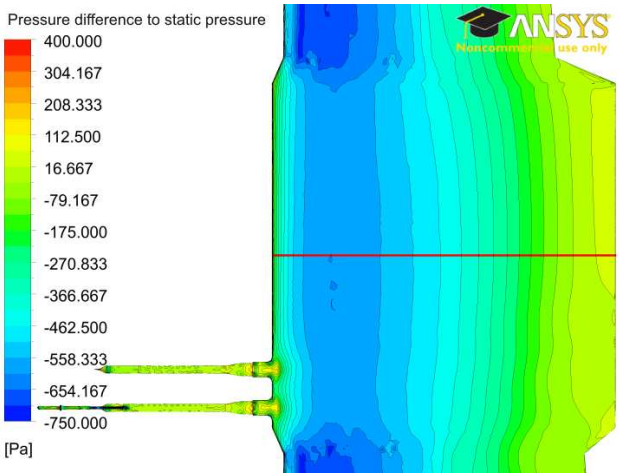

(a) suction side

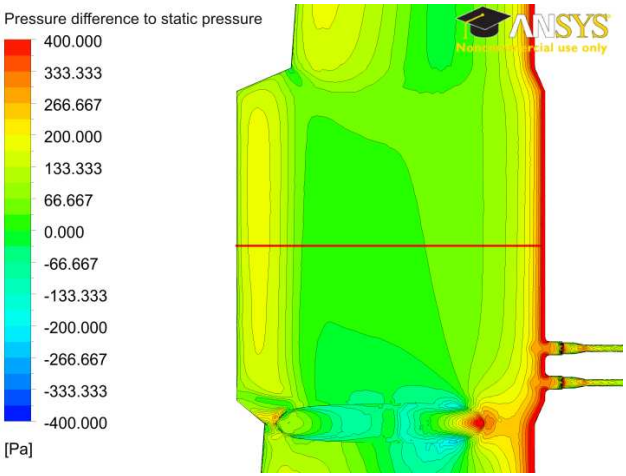

(b) pressure side

Figure 5.5.: Calculated pressure distribution for $\alpha = 6°$.

glove. It is identifiable that the static pressure on the suction side is lower on the wing compared to the glove. The resultant lower lift was taken into account in the design phase and is compensated through an increased chord length. The isobars are almost straight and not tilted on the suction side, the pressure distribution on the pressure side is almost uniform over a wide range.

Strong pressure gradients can be seen at the edges of the glove, especially in the area where the trailing edge intersects with the fillets to the wing with a large step in chord length. To reveal the influence of these pressure gradients on the two-dimensionality of the flow in the center section of the glove, the cross flow velocities outside the boundary layer (h=5mm) are extracted from the numerical results. Again, the most critical case ($\alpha = 6°$) is plotted, see Figure 5.6. Highest cross flow velocity components can be found at the edges. The same behavior was observed in the tuft studies in the wind tunnel. Clearly visible is also the influence of wakes of the booms on the suction side. This influence was also observed in tuft and oil flow visualizations. The abrupt widening of the vortices at 0.7 x/c comes with the turbulent mixing in the starting separation. Due to the separation with fluttering tufts in this condition, the widening was not visible in the tuft studies.

The chordwise and spanwise velocity components along the center line for different AoAs are plotted in Figure 5.7(a) and (b). For a better comparison of the chordwise velocity component U (a) with the spanwise velocity component V (b) for which no dimensionless coefficient is defined, absolute values for both velocity components are plotted. The inflow velocities for the calculations correspond to the freestream velocities of the respective flight condition.

For the analysis of the two-dimensionality of the flow in the center section, the ratio between V and U is plotted along the centerline for the suction side (c) and the pressure side (d). For attached flow the crossflow velocity component is less than 1% compared to the chordwise component over almost the entire glove. For the highest AoA of 6° the influence of the incipient detachment together with the wakes of the booms are visible. Still the crossflow component is below 4% before flow direction changes in the detached flow at the trailing edge.

The flow on the suction side is affected by the separation with increasing AoA whereas there is no separation on the pressure side. Hence the effects of AoA changes are less on the pressure side. Although the changes are less the cross-flow velocity components are higher but do not exceed 3%. For this reason the flow can be called two-dimensional

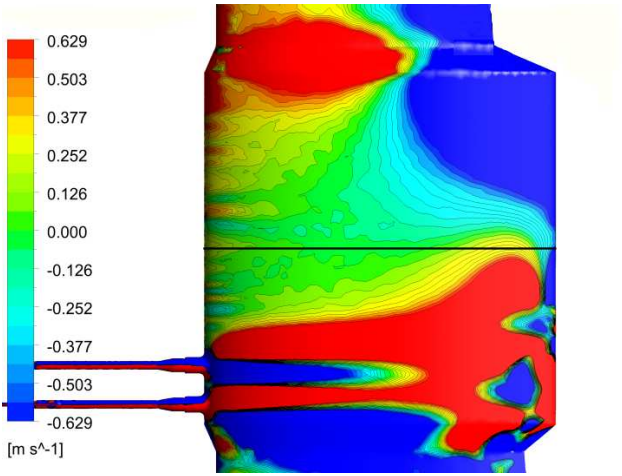

(a) suction side

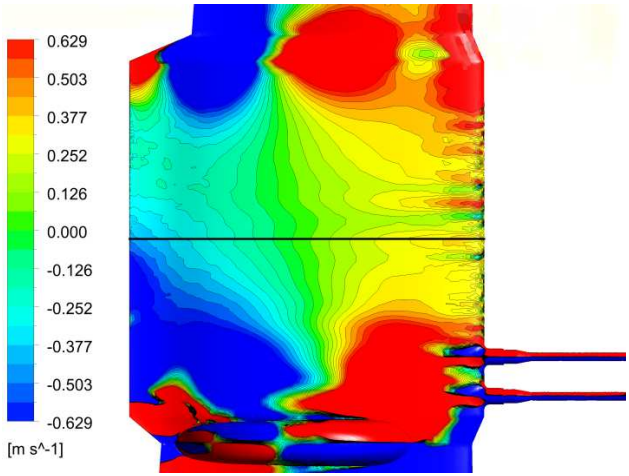

(b) pressure side

Figure 5.6.: Cross flow velocities outside the BL for $\alpha = 6°$.

in the center section and measurement area respectively.

Flow Field near the Wing

The other important influence besides the flow around the glove is the influence of the glove or the wing on the flow field near the wing. For practical reasons the probes for the measurement of important flow quantities have to be placed in the near field of the wing or glove respectively and cannot be located in the undisturbed far field. Therefore the flow quantities at the positions of the measurement probes must be known. Especially the AoA measurement, either with a wind vane (FlightLog) or the X-Wire probe, is effected by the curvature of the stream lines in front of the wing.

Complementary to the in-flight calibration for AoA measurements in the flow field near the wing, see Chapter 5.4.2, the flow field is also investigated numerically. Since the geometry of the glove has changed and only one reference flight case has been calculated in the former in-flight experiments by Erb [71], new calculations were carried out. In contrast to the simulations for the glove only with the 5.5 million cells mesh, the less detailed mesh covering the entire wing and the tip vortex (10.7 million cells) is used instead. Although the number of cells is almost doubled due to the much bigger computational domain, the resolution of the boundary layer is lower. A resolution of the boundary layer is not as important as in the previous case because an inviscid flow solution is sufficient to calculate the flow field near the glove for attached flow conditions.

The results of the calculations for a corrected angle of attack measurements are shown in the following section together with the results of the in-flight calibration. Corrections for the static pressure measurements are only determined by in-flight calibration since the possible errors due to the probe geometry are higher than the effects arising through a change in static pressure at the probe location.

5.4. In-flight Calibration

5.4.1. Pitot-Static System Calibrations

A high measuring accuracy of dynamic and static pressure is essential for reliable velocity and altitude determination. Additionally, the static pressure is used as a reference pressure for the airfoil pressure distribution and wake rake measurements.

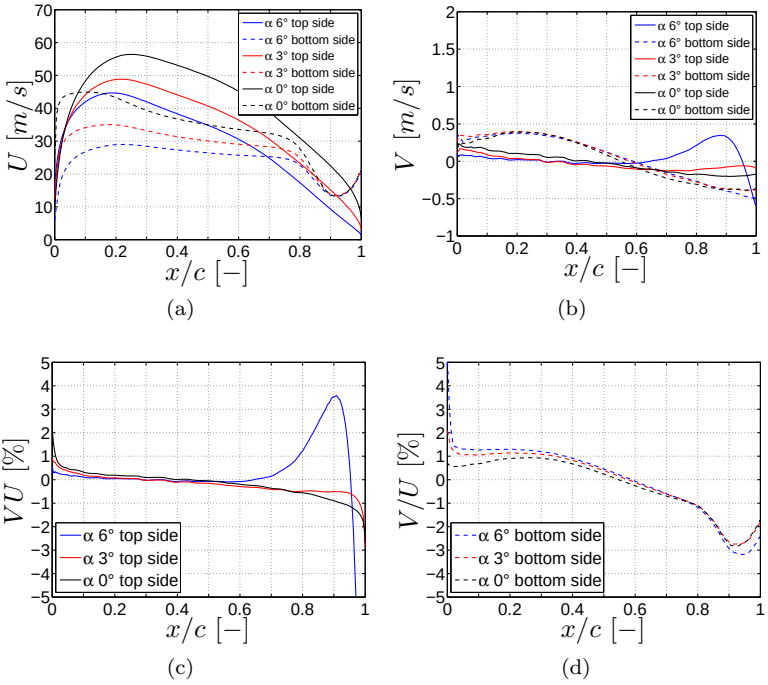

Figure 5.7.: Velocity components along the glove center line for different AoAs calculated with CFX [94]: (a) Absolute velocity in in chordwise direction; (b) Absolute velocity in in spanwise direction; (c) Relative velocity in in spanwise direction on top side; and, (d) Relative velocity in in spanwise direction on bottom side.

Measurement Errors

Measurement errors can be divided into two components: random errors and systematic errors. Random errors are always present in a measurement. Random errors show up as different results for the same repeated measurement. To minimize random errors pressure transducers with high accuracy and low signal-noise level have been used. They were calibrated in the lab by Böpple [89] through which systematic errors could be identified and subsequently eliminated. Systematic errors in the flight case are for example the influence of the humidity on density or measurement errors resulting from the shape of the probe and its position in the flow-field.

Whereas the influence of the humidity is investigated theoretically [90],[89], the measurement errors through probe shape and position have to be calibrated in flight. As a general rule the total pressure can be measured everywhere in the proximity of the aircraft as long the position is outside the boundary layer. Pitot tubes are unsusceptible against moderate slip angles [70] and therefore not prone to errors. The measurement of the correct static pressure is more difficult since the local static pressure is influenced by the flow field around the aircraft. This error is called position error and different methods for its determination are proposed in [7]. The onboard reference method used for the calibration of the old measurement system by Erb [71] was not feasible because the required "static bomb" was not accessible. For this reason a GPS method is was used instead.

GPS Method

Using GPS to determine pitot-static errors is a relative method. Detailed descriptions are given by Gray [96] and Lewis [97]. The big advantage of the method is that no additional equipment is needed and all required data can recorded using the G109b's measurement system. Using this data set instead of a handheld GPS and recording the data, the accuracy of this calibration method is comparable to a calibration with a "static bomb".

To do this method, at least three legs are flown at the same airspeed and altitude. Using GPS ground speed and ground track are recorded on each leg. Assuming the aircrafts true airspeed and the wind speed and direction are constant on each of the three legs, then three equations in three unknowns can be solved giving wind speed, wind direction, and true airspeed. Flying four legs instead of three legs results in three

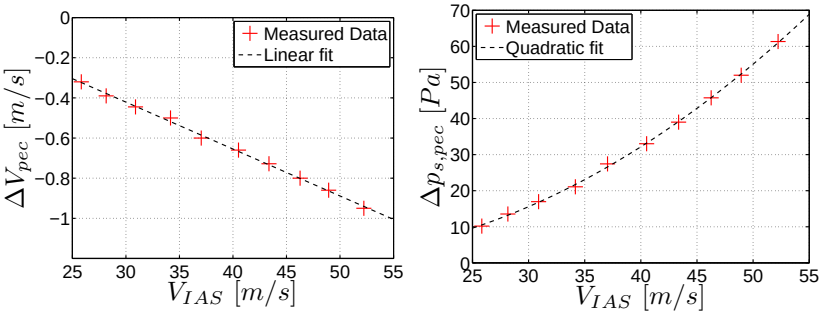

(a) Airspeed position error correction factor

(b) Static pressure correction factor

Figure 5.8.: Results for the pitot-static system calibration using GPS [89].

solutions. The standard deviation calculated from this three solutions shows the accuracy of the data point. The GPS-derived true airspeed V_{true} is then used to determine the pitot-static error by comparing it to the indicated speed V_i, corrected to true airspeed, using the following relationship:

$$V_i + \Delta V_{ic} + \Delta V_{pec} + \Delta V_c = V_{true}\sqrt{\sigma} \tag{5.25}$$

The indicated speed V_i can be taken from the ambient air data system, the instrument correction ΔV_{ic} is already incorporated in the sensor calibration. ΔV_{pec} is the unknown position error correction and ΔV_c is an altitude correction factor insignificant for the flow altitudes. The true airspeed V_{true} determined from the GPS legs is multiplied with the density ratio σ between the air density at altitude ρ and the standard air density $\rho_0 = 1.225\ kg/m^3$. The static pressure error $\Delta p_{s,pec}$ is calculated assuming all of the error in the dynamic pressure measurement $p_{dyn} = p_{tot} - p_s$ is in the static port.

Calibration Functions

The results of the in-flight, pitot-static calibration are shown in Figure 5.8. The plotted values are the correction factors, not the errors. At the lowest flight speeds the airspeed indication reads 0.3 m/s higher than correct. At the highest flight speeds the error increases to about 1

m/s. Assuming an error in the static pressure measurements this means that the measured static pressure is lower than ambient static pressure, which is plausible. Using additional sensors temporarily, position errors and correction factors are also obtained for the static pressure port at the boom of the wing glove which serves as source for reference pressure for the pressure distribution measurements. All calibration factors from the pitot-static calibration are incorporated into the measurement system calibration functions and used in the data post precessing.

5.4.2. Angle-of-Attack Measurement

Fast and accurate angle of attack measurements are an important element in this study. They are needed to validate the performance loss theories involving lift. The advantages of the chosen two-part system, where a wind vane (FlightLog) delivers a long-term stable reference for steady flight conditions and a hotwire probe measures fast variations, haven been described before. All measurement systems, which measure a flow angle in the disturbed flow field of the wing, are prone to systematic error, see Figure 5.9(a). The streamlines near the wing are already curved through the influence of the wing and not parallel to the streamlines of the undisturbed free flow. This error strongly depends on the position of the probe in the flow field, especially the streamwise distance between the probe location and the wing.

Different calibration methods to determine a correction function are possible. In horizontal flight, AoA is coupled with inclination of the aircraft longitudinal axis. Only the constant offset between wing incidence angle and the longitudinal axis has to be considered. For the calibration the inclination of the longitudinal axis is measured with an inclinometer and compared with the angle from the FlightLog. Measurement errors occur if horizontal flight condition is not kept exactly, which can be seen in some measurement points in Figure 5.9(b).

Good agreement with the numerical simulations in *CFX* using the grid for the entire wing can be seen. The AoA for the airplane is set in the simulations, than the velocity components at the place of the measurement are taken out of the flow field around the G109b. Figure 5.9(b) shows the results at the position of the FlightLog. A steeper gradient is found at the position of the hotwire, which is closer to the wing. This procedure includes the effects of the three-dimensional flow around the wing.

In this study, the influence on the airfoil characteristics is investigated.

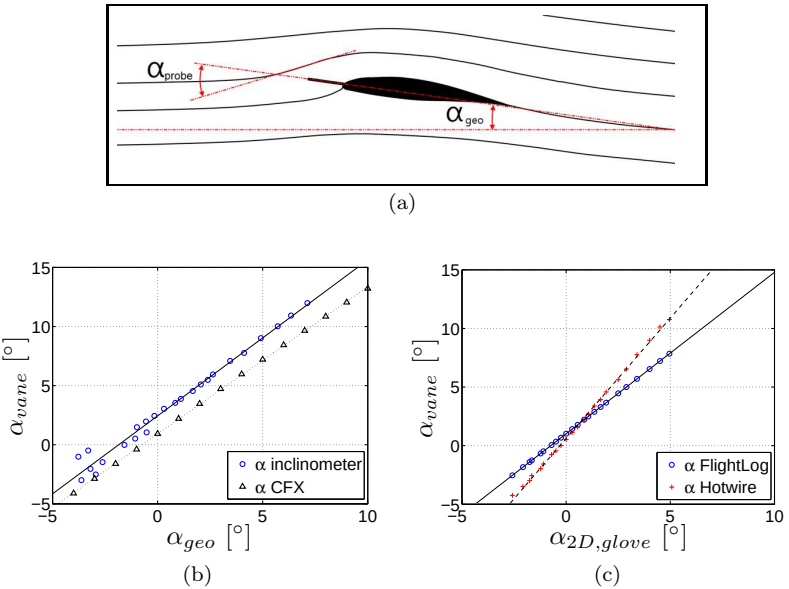

Figure 5.9.: Correction of angle of attack measurements: (a) Systematic error in AoA measurements in the flow field of the wing; (b) Flow field angle at FlightLog position versus geometric AoA; (c) Calibration functions for FlightLog and hotwire probe.

Therefore a different angle of attack definition is used in the following chapter. The pressure distributions measured on the glove are taken and fitted with calculated pressure distribution for the two-dimensional airfoil section. The two-dimensional airfoil pressure distributions are calculated using *xfoil*. The AoA value for two-dimensional flow from *xfoil* to match computed and measured pressure distribution is called $\alpha_{2D,glove}$. A more detailed overview on the AoA definitions used within this study are given in Appendix A. This reference angle is then compared with the measured angles from the FlightLog and the hotwire for this flight condition. The results of the calibration for the FlightLog as well as the hotwire are shown in Figure 5.9(c). These calibrations are used to correct for the time-independent systematic error of AoA measurements in the flow field of the wing, see also Appendix B.

The FlightLog is long-term stable and reliable and the systematic flow field error does not change with the time. Therefore the comparison between the corrected AoA value from the FlightLog with the corrected value from the hotwire is used as a health monitoring of the system each time non-turbulent flight conditions are encountered.

Furthermore the corrected AoA measurements from the FlightLog allow to check the calibration of other hotwire probes than the one used in the original in-flight calibration process.

5.5. Results for Stationary Flight Conditions

5.5.1. Flight Envelope

The flight envelope defines the operating range of the aircraft. For the horizontal flight condition lift must equal weight. Therefore the dynamic pressure is coupled with the lift coefficient and angle of attack respectively for a given wing loading. This relation can also be expressed using the calibrated airspeed instead of the dynamic pressure, see Equation 5.23.

In terms of flight velocity, the limits of the flight envelope are the stall speed V_{S0} on the one hand and the never exceed speed V_{NE} on the other hand. Flight at stall speed is not a stable reproducible flight condition. Furthermore, in turbulent atmospheric conditions the maximum allowed speed is lower than the never exceed speed. These limitations reduce the usable range of flight conditions for measurements compared to the flight envelope.

Figure 5.10 is the result of flight tests under non turbulent conditions

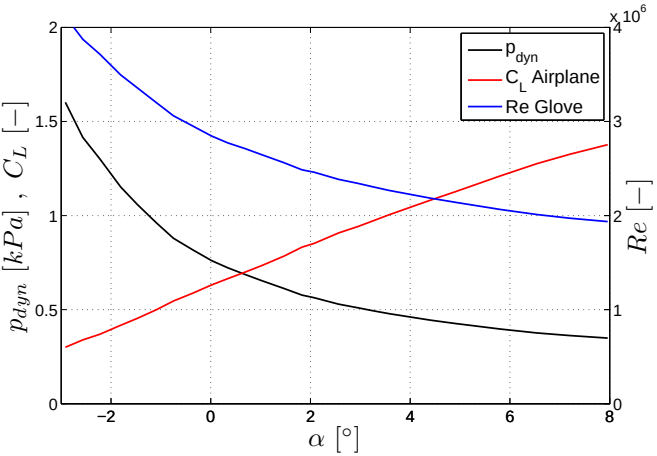

Figure 5.10.: Flight envelope of the G109b with measurement equipment. Dynamic pressure corresponds to a mass of 930kg. Glove Reynolds number measured at an altitude of 2700 meters and 5°C OAT.

and shows the flight envelope of the G109b with measurement equipment. The relation between AoA and dynamic pressure. It corresponds to an airplane mass of 930kg. The relation for other airplane masses can be easily obtained with an analytical correction using the horizontal flight condition. The usable AoA range for measurements is from about $-2°$, which corresponds to the maximum speed in turbulent conditions, to about $4-5°$, which is the maximum AoA where a steady flight without flow detachment on the wing is possible.

The horizontal flight condition is also used to calculate the lift coefficient C_L of the airplane. It should be noted that the lift coefficient of the wing is a bit higher than the the airplane lift coefficient because the wing has to not only carry the weight but also the negative lift of the horizontal tail.

The Reynolds number shown in Figure 5.10 is the result of a measurement at a pressure altitude of 2700 meters and an outside air temperature (OAT) of 5°C. The Reynolds number for a given AoA varies with altitude and ambient conditions. Therefore the altitude for a measurement must be adjusted if a constant Reynolds number is sought at

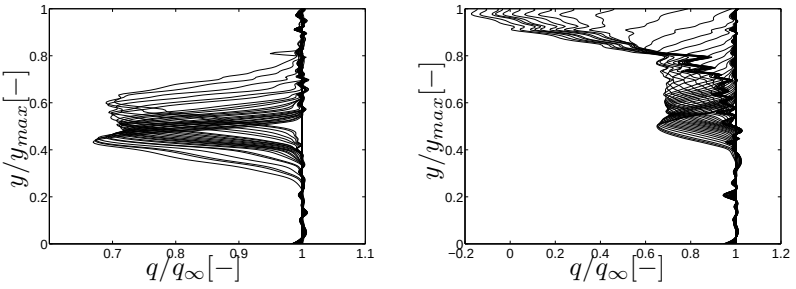

(a) In-flight (b) Wind tunnel

Figure 5.11.: Wake rake velocity distributions.

a given AoA for exactly reproducible reference flight conditions, see Erb [71]. This is important for transition or active flow control in-flight experiments. In this work it is not possible to keep the Reynolds number constant for each AoA since the altitude for the experiments depends on the meteorological conditions like condensing level (cloud base).

The knowledge of the flight envelope and the relation between dynamic pressure and AoA is important to conduct wind tunnel experiments which correspond to in-flight conditions.

5.5.2. Glove Airfoil Lift and Drag Polar

The knowledge of the glove's airfoil characteristics under steady conditions is an important prerequisite to determine the unsteady effects in the measurements under turbulent conditions. As described in Chapter 5.1.3, airfoil pressure distributions and the momentum deficit in the wake are measured and the coefficients calculated.

Figure 5.11 shows the dimensionless dynamic pressure distribution q/q_∞ over the dimensionless height of the wake rake y/y_{max} for different AoAs.

The AoA range for the in-flight measurements corresponds to the velocity range from maximum flight velocity down to minimum speed. The wake moves upwards with increasing increasing AoA and the wake gets wider. No massive separation is visible in the wake measurements. Flow detachment on the glove happens at a higher AoA compared to the wing. Therefore, the glove cannot be operated at AoAs, which are associated with flow detachment under steady flight conditions. This expresses it-

self also in the stall behavior of the airplane with equipment where a complete loss of lift is encountered on the side without the glove first.

In the wind tunnel the AoA is increased further and the behavior at high AoAs can be examined. The massive separation at high AoAs can be clearly seen in the results of the rake measurements. It also shows that the drag at very high AoAs cannot be measured since the wake grows larger than the rake.

The measured airfoil polars from the flight tests, wind tunnel tests and *xfoil* calculations are shown in Figure 5.12. The Reynolds numbers for the *xfoil* calculations are taken from the flight test results shown in Figure 5.10. For the wind tunnel results, the dynamic pressure is adjusted to in-flight conditions. The wind tunnel is also used to examine the airfoil behavior at high AoAs which cannot be achieved in steady flight but can be the result of an sudden AoA increase due to a gust. For AoA in excess of 8°, the dynamic pressure is kept constant because this is the best approximation for a gust encountered in slow flight.

The lift over AoA polar is shown in Figure 5.12(a). Measurements and calculations are in good agreement in the linear range of the lift curve. Also the biggest deficit of *xfoil*, the wrong prediction of lift in the non-linear lift range due to its simple boundary layer model, is clearly visible. It can be seen that maximum lift of the wing is reached just before flow detachment occurs on the glove. The maximum AoA of about $4 - 5°$ where the G109b flies stable, the AoA increase due to a gust must be at least $3 - 4°$ until the linear range of the lift curve is left.

This behavior can also be seen in the drag curve in Figure 5.12(b). The wind tunnel results show that the laminar drag bucket of the glove airfoil is left at an AoA of about 9°, which is beyond the G109b's flight range. At 11° the wake starts to exceed the rake, see also Figure 5.11, which results in an erroneous drag measurement (dotted extension of the drag curve).

Figure 5.12(c) shows the lift over drag curve for the glove airfoil. It is apparent that *xfoil* underestimates drag and overestimates lift. However, the principal airfoil behavior is predicted well. It must be noted that the drag is only measured at one spanwise position since the wake rake is fixed. Althaus [11] shows variations of the drag coefficient of about 10% if the rake is moved in spanwise direction. The less smooth polar in case of the in-flight tests compared to the wind tunnel test may be a result of slight slip angles and the measurement at a different spanwise position, as well as less constant flow conditions in flight.

The drag difference between wind tunnel has not been investigated

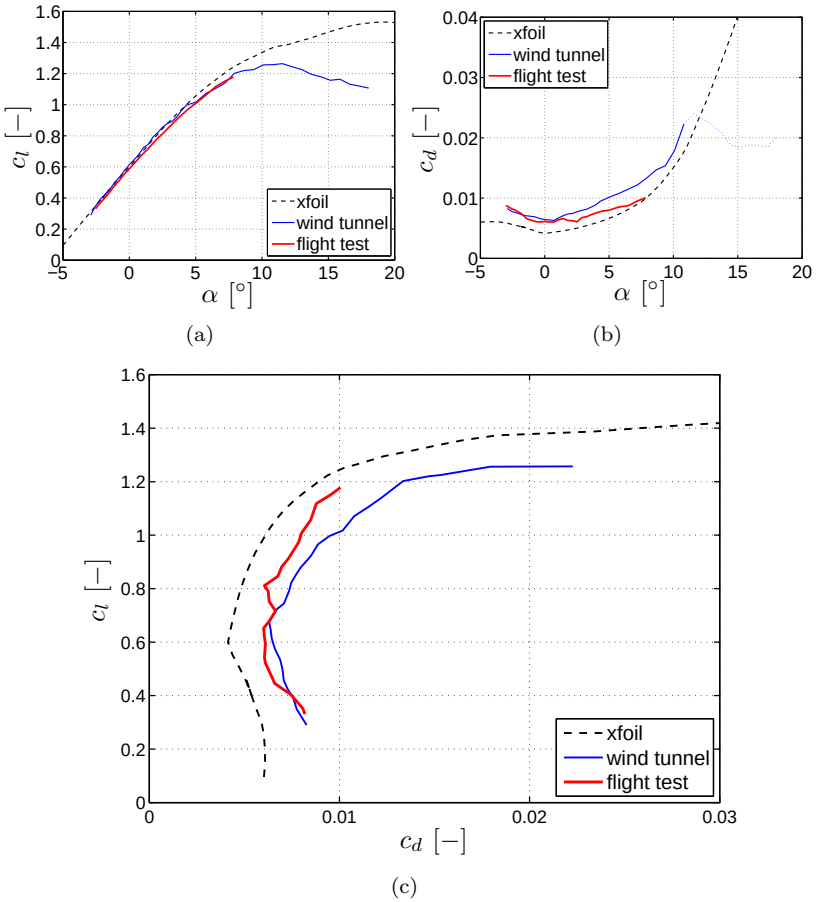

Figure 5.12.: Comparison of the polars of the wing glove airfoil from flight tests, wind tunnel test and calculations. (a) cl-alfa-polar; (b) cd-alfa-polar; (c) cl-cd-polar.

since the wind tunnel measurements are only for a reference and no wind tunnel corrections have been applied. A difference in the pressure distributions between wind tunnel and flight at higher AoAs has been noted. This is a result of the considerable blocking due to the large glove. Although no corrections have been used to improve the quality of the wind tunnel data, the results give a good indication of the behavior of the airfoil beyond steady flight conditions.

5.5.3. G109b Airspeed Polar and Drag Breakdown

This study is related to aircraft performance under turbulent atmospheric conditions. The main measure of aerodynamic performance of an aircraft is the aircraft's lift-to-drag polar. The lift-to-drag polars for the individual aircraft components add up to the overall polar. Lift contributions mainly come from the wing and the horizontal tailplane, the fuselage is a significant additional source of friction drag.

Because the entire flow field around the airplane cannot be measured, not all effects of atmospheric turbulence on the overall lift-to-drag polar and consequently aircraft performance can be measured. For example the spanwise lift distribution, which affects the induced drag, may differ from the undisturbed lift due to an irregular AoA distribution in spanwise direction. Hence the performance variations due to aerodynamic effects cannot be separated from meteorological influences on the flight path, e.g. up- or downdrafts. Therefore a different approach is taken here.

The influence of turbulence on certain aerodynamic quantities is measured during the in-flight experiments and can be quantified. The influence of turbulence on other quantities cannot be measured using the given equipment. In order to quantify the influence of turbulence on the aircraft performance a new lift-to-drag polar is calculated using a bottom-up approach. Therefore, the airfoil lift and drag polar is modified and the influence of a change in lift on induced drag is included. The influence of a possible spanwise variation of the lift distribution on induced drag is not known and therefore excluded. The influence of turbulence on the fuselage drag is considered as small and neglected consequently.

For the calculation of a reliable bottom-up polar a thorough knowledge of the lift- and drag contributions from all aircraft components as well as the interaction effects is essential. The manufacturers lift and drag assumptions for the individual aircraft components are not published.

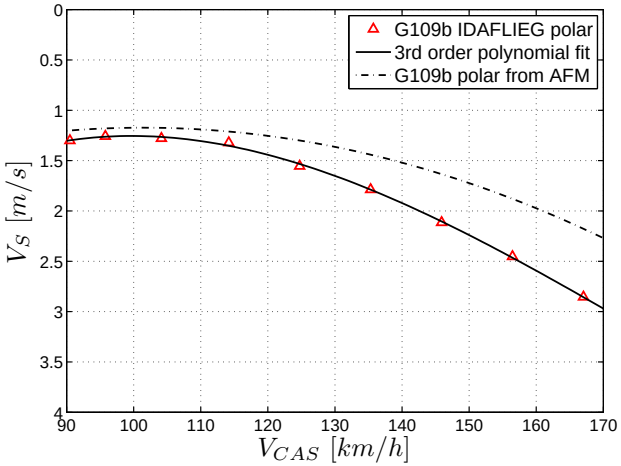

Figure 5.13.: G109b airspeed polars. All polars corrected to a mass of 950kg ($W/S = 490N/m^2$).

However, the comparison of the G109b's calculated (bottom-up) airspeed polar from the aircraft flight manual [82] with the measured airspeed polar of the clean G109b [98] shows significant discrepancies between both polars. The measured *IDAFLIEG* airspeed polar is considered to be accurate whereas the manufacturer's calculated airspeed polar taken from the AFM is way to optimistic. Both polars are mathematically corrected to the increased maximum take-off mass of the G109b with measurement equipment, which is 950kg and shown in Figure 5.13.

The conclusion from the comparison of the measured and the calculated airspeed polar is that the manufacturers assumptions for the individual lift and drag components are not correct. Therefore, no attempt was undertaken to obtain these values from the manufacturer for the assessment of the influences of atmospheric turbulence on performance.

An alternate procedure to obtain component lift-to-drag polars is the top-down lift and drag breakdown of the overall aircraft polar. This procedure is common practice either to correct theoretical component lift and drag data using flight test data or in performance calculations when lift and drag data of individual components are not available, e.g. in competition aircraft analysis.

For the estimate of the influence of atmospheric turbulence on aircraft performance, component lift and drag is obtained from a top-down lift

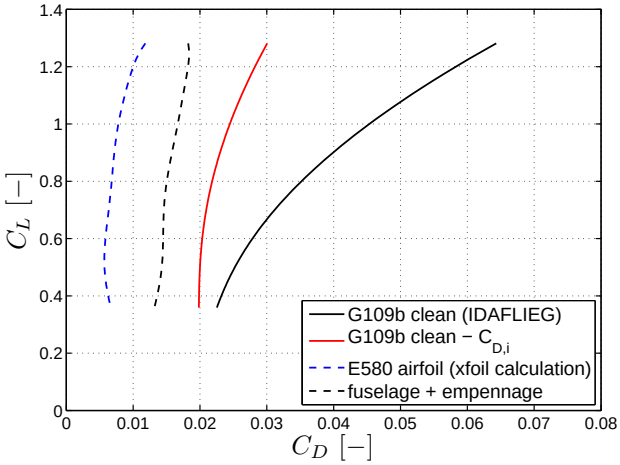

Figure 5.14.: G109b drag polar calculated from measured airspeed polar.

and drag breakdown. Then, component lift and drag is corrected individually using the measurement results. After that, the new polar is created using this data for a bottom-up calculation. Since the overall lift contribution of the horizontal tailplane and the fuselage is relatively small, all lift is accounted to the wing. All drag components not associated with the wing are accounted to the fuselage and assumed to be constant under the influence of atmospheric turbulence. A further breakdown into fuselage, empennage, landing gear and "unaccounted" components (antenna, fairings etc.) is not performed because it would only add complexity without providing any additional insights. Typically, drag components categorized as "unaccounted" are the main culprits for the difference between calculated bottom-up and measured polars. The *IDAFLIEG* airspeed polar is used for the lift and drag breakdown since the clean aircraft configuration without any measurement equipment is the typical aircraft configuration which should be evaluated.

Rearranging Equation 5.23 to solve for the lift coefficient, the airplane lift coefficient is calculated from the speed polar. The drag coefficient is calculated from Equation 5.24, rearranged to solve for C_D. Knowing C_L the induced drag is calculated using Equation 2.31. The lift distribution and Oswald factor e for the G109b wing is calculated using the Multhopp method described in [9]. Because the G109b wing is not twisted, the Oswald factor depends only on the wing's outline and is constant for all

AoAs. The value is $e = 0.9652$ for the G109b wing. The induced drag is a drag component which varies under the influence of atmospheric turbulence.

Subtracting the induced drag from the airplane drag, the drag of the fuselage with empennage and the airfoil drag remain. The airfoil drag is another drag component which is affected by atmospheric turbulence whereas the influence on the fuselage is neglected. Because no wind tunnel measurements of the E580 airfoil are known, the airfoil drag of the E580 is calculated using *xfoil* and increased by 10% due to the known underestimation of drag. It is then subtracted yielding the drag of the fuselage with empennage and "unaccounted" components. As described before, this drag is not broken down further for reason of simplification. The results of the top-down lift and drag breakdown are shown in Figure 5.14.

6. Performance Variations due to Turbulent Atmospheric Conditions

6.1. Effects of Atmospheric Turbulence

6.1.1. An Exemplary Flight into Turbulence

The influences of atmospheric turbulence on the aircraft and its performance are investigated in the following. Before special flight conditions, which were pointed out in the theoretical analysis, are investigated in detail, a gliding flight from slight turbulence into moderate turbulence is used to illustrate the processes in atmospheric turbulence.

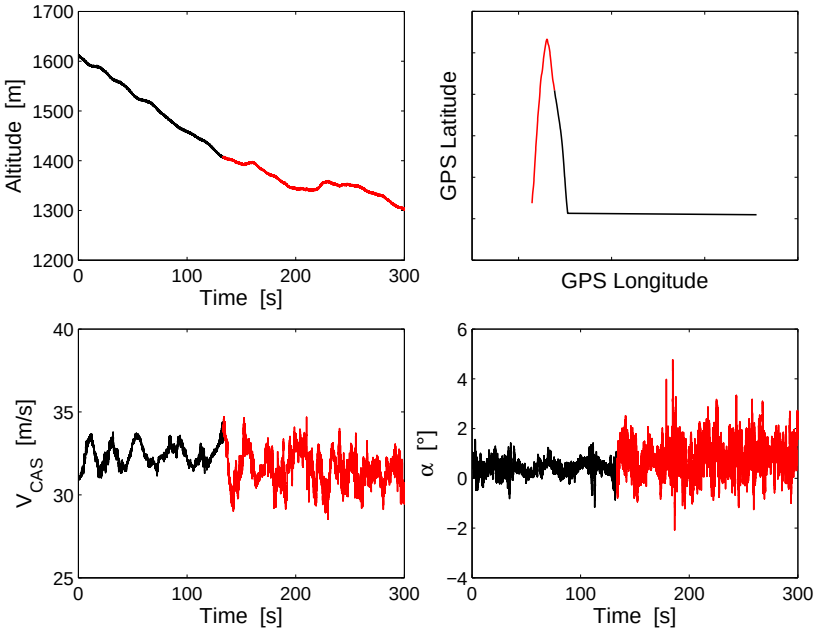

Figure 6.1.: Flight conditions for a flight from slight turbulence (black) into moderate turbulence (red).

Figure 6.1 shows the basic flight condition. The glide starts above the cloud base besides a cumulus cloud. In this area only slight turbulence is found. Although the slight turbulence is imperceptible for the pilot, the atmosphere is not stable in such meteorological conditions and therefore the turbulence level is higher compared to the stable atmosphere above a temperature inversion. The steady glide can be seen in the altitude diagram in Figure 6.1. Turns are only flown to navigate under the cloud into more turbulent conditions.

In order to provide a comparison to realistic flight conditions, no special attention is paid to keep the airspeed absolutely constant using the flight guidance system as in calibration flights. The variations in airspeed are still less than half of the allowed tolerances to pass a practical flight test. Upon entering turbulent air, the magnitude of the airspeed variations increases. This is becomes even more apparent for the AoA variations. It must be pointed out that the AoA measurement in Figure 6.1 is more "noisy" than the velocity measurement because it is taken from the hotwire measurements whereas the V_{CAS} is calculated from the measured dynamic pressure in this overview.

6.1.2. Inflow Conditions and Aircraft Response

Velocity

Realistic inflow conditions in flight are an important aspect which must be considered carefully. First, the inflow velocity is treated. For a high temporal resolution the velocity is taken from the hotwire measurements. For accurate results, the calibration function of the hotwire probe is corrected to match the velocity from the air data system under the actual ambient conditions, which differ from the calibration ambient conditions significantly. Because turbulence level and atmospheric turbulence spectra are calculated from the velocity data, the true airspeed V_{TAS} is used.

Figure 6.2 shows V_{TAS} over the time. Velocity is decomposed into a low-pass and a high-pass signal using two different filter frequencies. One filter frequency is 0.2 Hz, the other is 25 Hz. The first frequency is selected because 5 seconds is a typically time interval which allows the pilot to recognize a change in flight attitude and manipulate the controls as well as allows the airplane to respond to the pilot's control input. The second filter frequency is selected to investigate the influence of small scale turbulence. This filter frequency is chosen to represent the time that is required to travel the distance of one chord length of the glove. At a flight velocity of 27 m/s it takes 1/20 of a second to

travel this distance and at 40.5 m/s only 1/30 of a second is required. In order to have only one filter frequency for all measurements at variable airspeeds, 25 Hz is selected as mean value for typical speeds of the G109b. Additionally, 25 Hz is above the eigenfrequencies of the aircraft's basic flight dynamic modes (short period AoA oscillations are in the order of some Hz, the phugoid, which is the long period mode, has a duration in the order of 30 seconds) so that all velocity fluctuations with a frequency higher than 25 Hz definitely arise directly from small scale atmospheric turbulence.

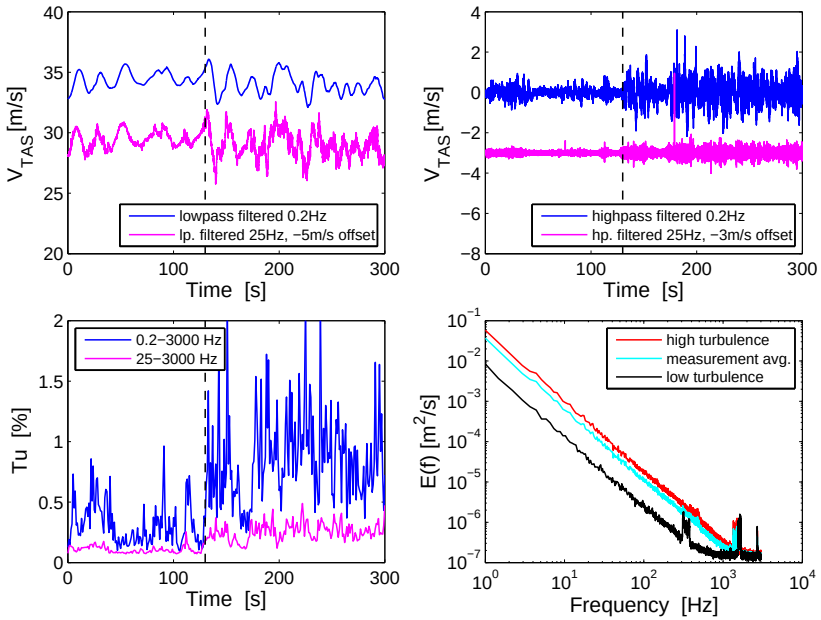

Figure 6.2.: Inflow conditions and atmospheric energy spectra for a flight from slight turbulence into moderate turbulence.

A filter frequency of 0.2 Hz is depicted by the blue lines in Figure 6.2. Consequently, the low-pass signal is a 5 seconds running average over the velocity. Upon entering more turbulent conditions (vertical black dashed line) the pilot is able to counteract the gusts and the magnitude of the velocity oscillations only increases slightly compared to less turbulent conditions. In contrast, the velocity fluctuations around the around the 5 second velocity mean value increase considerably.

Filtering at 25 Hz (magenta line, plotted with -3 m/s offset for clarity) shows the same low-pass behavior, only the signal is more noisy. The reason is the fast velocity fluctuations due to the turbulence, which cannot be counteracted by the pilot. The high-pass signal for this filter frequency shows much lower magnitudes compared to the lower filter frequency but the increasing magnitudes upon entering turbulent air are still clearly visible.

The turbulence level Tu is basically a measure of the standard deviation of the velocity fluctuations compared to the mean flow velocity. Therefore, the definition of the filter frequency determines the magnitude of Tu. The usage of the average airspeed over a complete measurement to calculate Tu is not reasonable for in-flight experiments because the airspeed cannot be kept exactly constant, which would result in very high values for the turbulence level. These turbulence level values would also not be comparable to wind tunnel experiments where the mean flow velocity can be kept much more constant. Therefore, a running average must be used to analyze in-flight data.

The numerical values of Tu for the in-flight measurement using different filter frequencies are shown in Table 6.1. For a 5 second running average filter the turbulence levels are high. This is visible in Figure 6.2 and also reflected in the mean values. These high turbulence levels are comparable to other results [61]. For comparison with turbulence levels in wind tunnel experiments a higher filter frequency is useful. The justification for the selection of a 25 Hz filter frequency has been given before. This leads to much lower values for Tu which are better comparable with other works on receptivity and the influence of small-scale turbulence on airfoils.

Measurement quantity	**Average low turb.**	**Average mod. turb.**	**Average flight**
Tu(0.2-3000Hz) [%]	0.3178	0.8775	0.6366
Tu(25-3000Hz) [%]	0.1078	0.2571	0.1928
ϵ $[m^2 s^{-3}]$	$3.367e^{-4}$	$63.018e^{-4}$	$37.343e^{-4}$
$\epsilon^{1/3}$ $[cm^{2/3} s^{-1}]$	1.499	3.979	3.342

Table 6.1.: Numerical values for Tu and ϵ for the measurement depicted in Figure 6.2.

The last plot in Figure 6.2 shows the average turbulence spectra for the two parts of the measurement as well as the entire measurement.

Turbulent kinetic energy is plotted as a function of the frequency. In the logarithmic plot the -5/3 slope is clearly visible. Because the slope is constant and known in the inertial subrange, the spectrum is defined solely by the energy dissipation rate ϵ. Three average energy dissipation rates are calculated from the three average spectra (low turbulence in black, higher turbulence in red and flight average in cyan). For a better comparison with the values given by MacCready [33], which are shown in Figure 2.10, also the value of $\epsilon^{1/3}$ in the units $[cm^{2/3}/s^{-1}$ is calculated and listed in Table 6.1. The $\epsilon^{1/3}$ values are in good agreement with the values given by MacCready for different meteorological conditions.

Angle of Attack

Analogous to the procedure with the velocity data, the measured angle of attack is decomposed into a low-frequency and a high-frequency part. Different filter frequencies compared to the ones for the velocity decomposition are used though. The first filter frequency of 0.5 Hz is chosen because 2 seconds is roughly the time which is required to travel the distance of 63 times the chord length at average airspeed. The second filter frequency of 2 Hz corresponds to 0.5 seconds, which is the time to travel 16 times the chord length. These distances are derived from the limits for quasi-stationary and highly unsteady aerodynamic behavior, see also Table 3.2.

In a low turbulence environment, the AoA variations are coupled to the velocity variations via the horizontal flight condition. The eigenfrequency of the phugoid is visible in Figure 6.3, the variation of the AoA is only minor in this basic flight dynamics mode. Entering a high turbulence environment, the variations in the AoA measurements grow considerably. This can be be seen in the low-pass filtered as well as the high-pass filtered AoA signal.

In contrast to wind tunnel experiments where an angle of attack is simply set, things are more complicated in flight because AoA is not constant, which means there is pitch. Also in the angle of attack measurement different effects are superimposed. If no atmospheric turbulence is present, the measured AoA in the consists of a steady angle of attack and a component due to the pitch rate. Therefore, the measurement is affected by the aircraft movement. This effect is only minor if pitch rate is low. Flying through turbulence, the AoA is changed because the direction of the inflow changes due to the additional vertical velocity of the gust. Furthermore, more pitch movement is found. These

effects cannot be broken up with the given measurement equipment. The coupling with the aircraft movement must be kept in mind.

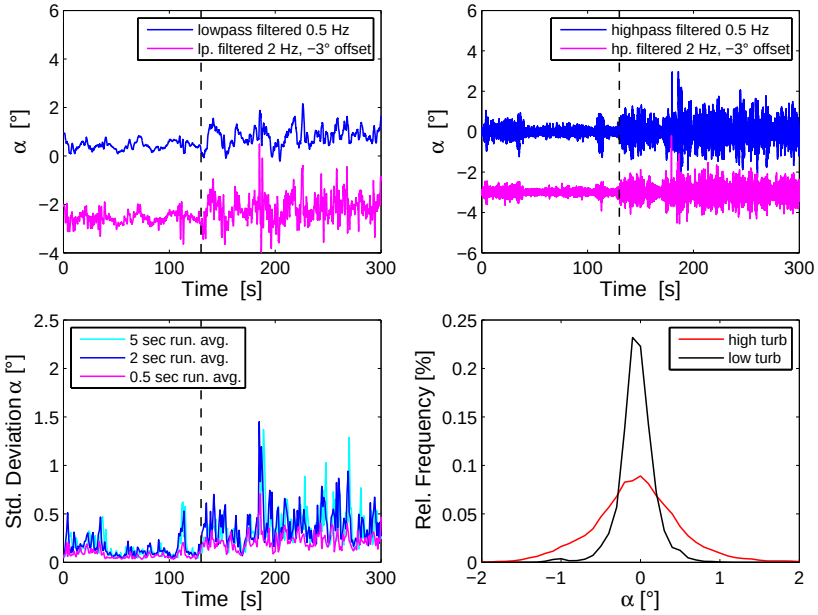

Figure 6.3.: Angle of attack variations for a flight into turbulence.

A statistical analysis shows the standard deviation of the AoA variations for 1 second intervals using different filtering frequencies. The AoA standard deviation increases abruptly and considerably upon entering more turbulent conditions. In this case the 5 seconds running average filter is used additionally. This time interval includes the quasi-stationary and unsteady AoA variations but excludes the phugoid movement.

A histogram plot shows the distribution of the AoA variations. Out of the reasons stated before, a 5 second running average is used to calculate the mean value and the variations. In the low turbulence environment (black line) the AoA distribution is narrow. More than 95% of the measurement points are within 0.5° of the mean values whereas in more turbulent condition the 95% threshold is at about ±1.2°.

Airfoil Pressure Distribution

The wider range of AoAs, which occurs under turbulent conditions, is also represented in the c_p measurements. Figure 6.4 shows the variations in the pressure distributions. Again, the flight is divided into the two flight segments with low turbulence (top) and the moderate turbulence (bottom). The range of the measured c_p values is increased in turbulent conditions. This can be seen especially in the front part of the airfoil where the local c_p variations with AoA in steady conditions are the largest.

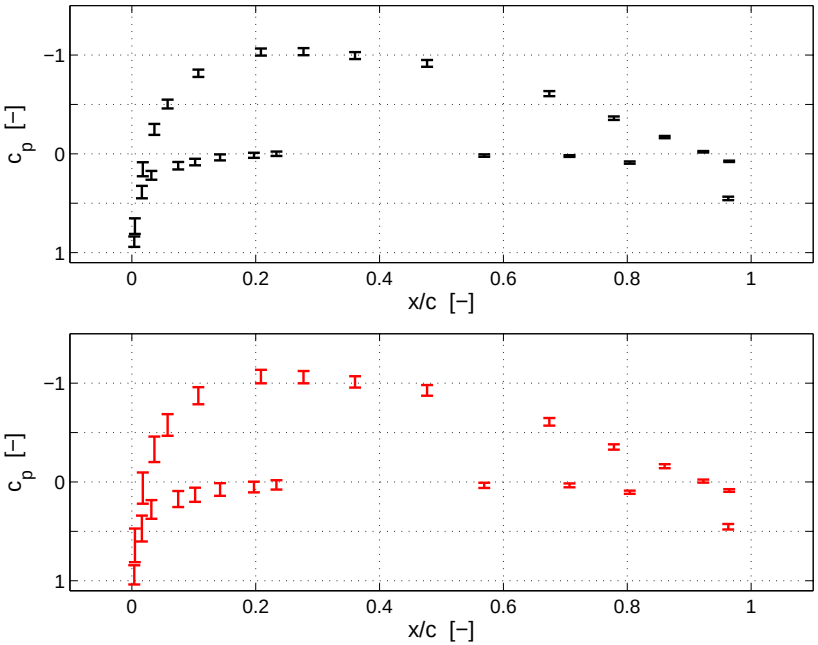

Figure 6.4.: Airfoil pressure distributions with maximum variations due to turbulence. The upper diagram shows the flight segment in low turbulence intensity.

Looking into the pressure distribution for the moderate turbulence case it is clearly visible that the AoA variations due to moderate gusts at the given mean AoA are not strong enough to cause stall effects. Not even a suction peak is found in the pressure distribution. On the

pressure side no pressure distribution with an adverse pressure gradient is found. A comparison between the extreme values of the measured pressure distributions on the pressure side and the calculated pressure distributions in Figure 4.3 shows that the laminar boundary-layer in the comparable steady conditions is stable. In the most stable case disturbance amplification starts at x/c=0.55, in the least stable case at x/c=0.2 with a N-factors of 5 at the tripping location of x/c=0.78, see Figure 4.4. Premature transition is not likely under these conditions.

Transition Location and Boundary-Layer Amplification

It can be assumed from the measured pressure distributions and turbulence levels in conjunction with the *xfoil* calculations that no premature transition occurs on the pressure side and also the changes in the transition location on the suction side are low in this flight condition. Unfortunately this assumption cannot be proved by measurements of the transition location. Although the microphone sensors delivered good results in preliminary experiments [80] and even TS-waves could be seen in the steady measurements by Reeh [90], numerous microphones did not deliver usable signals in the unsteady measurements with the new wing glove. The preliminary measurements, which led to selection of the microphones as a simple and cost-effective means of transition detection, were carried out just after the new microphones were assembled into the previous glove. After almost one year in the glove and various test and calibration flights, partially under extreme low temperatures and in rain, numerous microphones were no longer operational. Hence, the transition location was not detectable. Therefore, a more reliable means of transition detection is required in the future part of this research project beyond this study.

6.1.3. Relation between Aerodynamics and Meteorology

An important novelty presented in this study is to establish a connection between flight physics and meteorology. This has already been accomplished in the field of gust loads, e.g. see MacCready [33], but there is no connection between aircraft performance and atmospheric turbulence. The measurement parameter for turbulence intensity in meteorology, which is also utilized in this study, is the energy dissipation rate per unit volume ϵ measurement parameter. It is calculated once a second from spectral analysis of the measured velocities (hotwire measurements). For each 1 second time interval the turbulence level (25-3000Hz)

and the standard deviation of α is calculated. For the calculation of $\sigma(\alpha)$ the α signal is decomposed into a low-pass and a high-pass signal at a filter frequency of 0.2Hz.

The results are shown in Figure 6.5. The left diagram shows the relation between Tu and ϵ, the relation between $\sigma(\alpha)$ and ϵ is shown in the right diagram. Again, the black data points are the measurements from the low turbulence part of the flight whereas the red data points show the moderate turbulence part. Although the energy dissipation rate is low the for the first part of the flight, the turbulence level is still higher compared to the values for the stable atmosphere. There is also a certain standard deviation of the AoA at low turbulence intensities because the pilot is not able to hold AoA exactly constant.

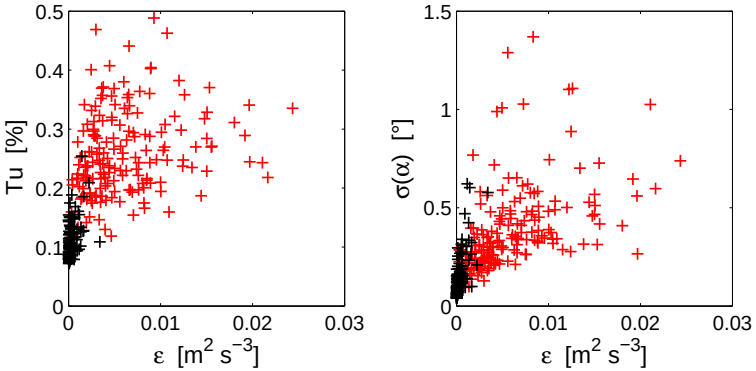

Figure 6.5.: Turbulence level and standard deviation of the angle of attack as function of energy dissipation rate ϵ.

Tu and $\sigma(\alpha)$ increase with ϵ. The specific events show a considerable scatter but the statistical trend is clear. The reason for that scatter is that the effects of the unsteady inflow conditions and the aircraft motion are superimposed. This scatter is important to be remembered when the flights are analyzed statistically in the following analysis. Especially for flights where the magnitude of atmospheric turbulence varies significantly, the statistical mean value underestimates the extreme values.

6.2. Slow Flight Performance

6.2.1. Statistical Analysis of Circling Flight in Thermals

After the influences of atmospheric turbulence and the differences between a low turbulence environment and higher turbulence haven been described, certain flight conditions are examined more detailed.

Circling flight within thermals is a very important flight condition in soaring applications. By definition this part of the flight must take place in thermal convection and hence elevated levels of atmospheric turbulence. Circling flight is characterized by high angles of attack and hence high lift and low airspeeds. Ideally, the lift coefficient is held constant at the upper end of the laminar drag bucket. This provides a minimum turn radius and minimum sink rate for each bank angle.

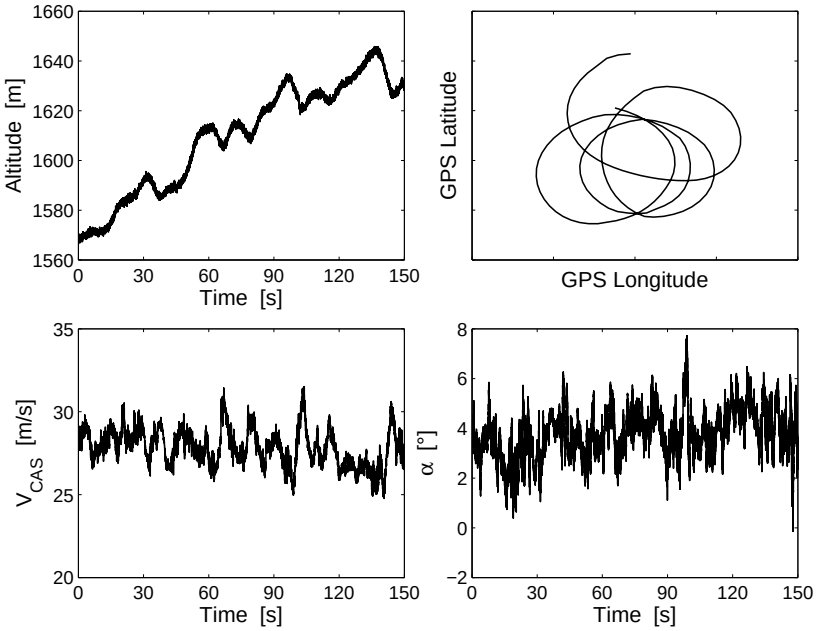

Figure 6.6.: Flight conditions for a flight within a themal.

Figure 6.6 shows the flight conditions for a typical flight. The climb rate of the G109b with the high wing loading and the additional drag due to the measurement equipment is not comparable to the climb rate

which can be achieved with a good glider. However, the much better performance of the glider compared to the G109b does not affect the aerodynamic processes. It must be noted again that the behavior of the G109b is dominated by the aerodynamic characteristics of the E580 airfoil and not by the glove airfoil. This is very important because the wing reaches its maximum lift at an AoA where the glove airfoil has not yet reached its maximum lift. Beyond an AoA of about 4° the linear lift range of the G109b wing is exceeded and drag increases. Therefore, an average AoA of about 4° can be found in the AoA plot for the circling flight.

Before this exemplary flight is analyzed in detail, the generality of this flight must be demonstrated. Therefore, 12 different circling flights, flown by three pilots during three days, are statistically analyzed. The results of the statistical analysis are shown in Figure 6.7. The exemplary flight is flight number 7.

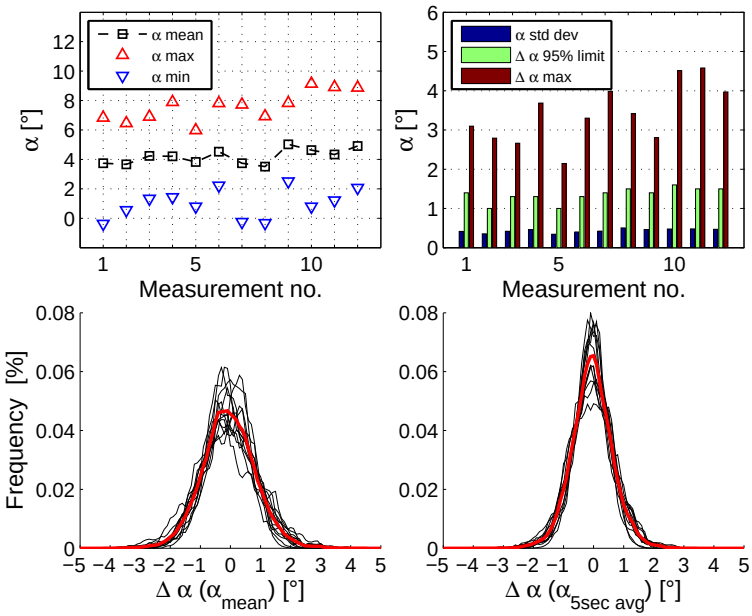

Figure 6.7.: Statistical analysis of 12 circling flight within thermals.

In the upper left diagram the mean AoA as well as the minimum and

maximum AoA values are plotted for all 12 flights. The mean values are in a narrow band around 4°. Also the minimum and maximum values are of the same order for all measurements. The reason is that all measurements are carried out under similar meteorological conditions although they are taken on three different days. Much stronger turbulence, e.g. in mountainous terrain, may lead to higher extreme values.

As it can be seen in the exemplary circling flight (Figure 6.6), maximum and minimum values are the result of a singular occurrence in the course of the measurement. The upper right plot in Figure 6.7 shows a bar chart comparing the angles of attack for the 12 flights. Compared with the maximum values (red bars), the standard deviation (blue bars) is significantly lower. To get a better impression which AoA variations must be considered, another value is computed. Therefore, a histogram is calculated showing the relative frequency of the AoA variations from the mean value. This is done for each measurement using all AoA values from this measurement. Then the lower and the upper α limit is calculated which contains 95% of the measured values. This limit is considerably higher than the standard deviation but still much lower than the maximum variations. Occurrences of very high AoA variations, which have little influence on the overall performance because they are rare, are excluded using this method.

The right histogram in Figure 6.7 shows the relative frequencies of α deviations from the 5-second running average of α. Therefore, deviations from the optimum AoA in circling flight are not shown in this histogram. This removes the "pilot factor" from the measurements as the pilot is not able to hold an AoA perfectly constant. The histograms for all flights are similar. In the left histogram the deviation from the average AoA of the whole measurement is shown. Hence, not only turbulence but also the "pilot factor" is included in this consideration. It is apparent that the histograms for the different flights are less similar compared with the histograms using the 5-second-average AoA as a reference. The spreading of the histogram and the flat top shows an AoA oscillation of about $\pm 0.5°$ around the optimum value. This must be accepted even in the case of experienced pilots and should be incorporated into any design considerations.

6.2.2. Airfoil Lift and Drag

The consideration of airfoil lift and drag is required to validate the existing theories on performance loss and develop an independent theory

which is backed by measurements under realistic conditions. As shown in the theoretical analysis, a separate valuation of different flight conditions is reasonable.

Because the lift coefficient is calculated from the pressure distribution (see Equations 5.17 to 5.19), the pressure distribution is examined first. Figure 6.8 shows the mean and extreme values of the pressure distribution in circling flight. No distinct suction peak or any stall indicators are visible in the pressure distribution. Because the lift slope of the glove airfoil is lower compared to the E580 airfoil of the G109b wing, the wing stalls first and no stall condition on the wing glove can be set in steady flight. Furthermore, the AoA variations due to moderate gusts are not sufficient to reach a stall on the wing glove.

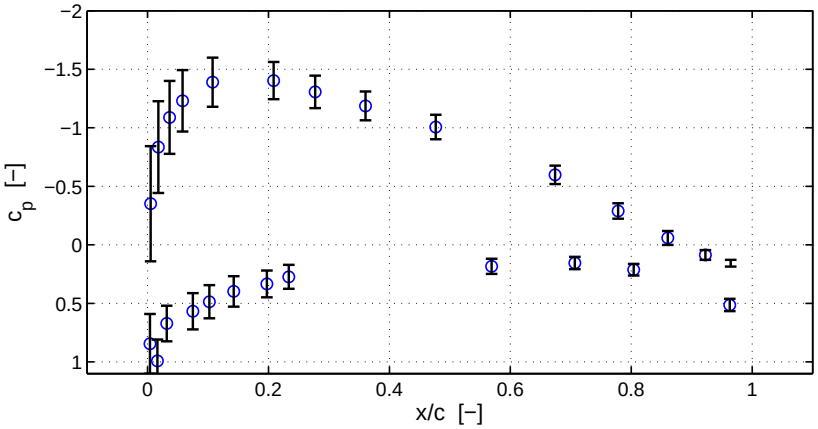

Figure 6.8.: Airfoil pressure distribution with maximum variations due to turbulence for a circling flight within a thermal.

The mean values of the pressure distribution show the typical shape of a steady pressure distribution for a high lift coefficient. The variations in the pressure distributions are higher compared to the exemplary horizontal flight in the first section. Because the mean pressure distribution has a strong favorable pressure gradient on the pressure side, even the least favorable pressure gradient due to the AoA variations generates a very stable boundary-layer. Although there is no direct proof through a measurement of the transition location, this pressure gradient is an indirect evidence that no premature transition occurs in circling flight

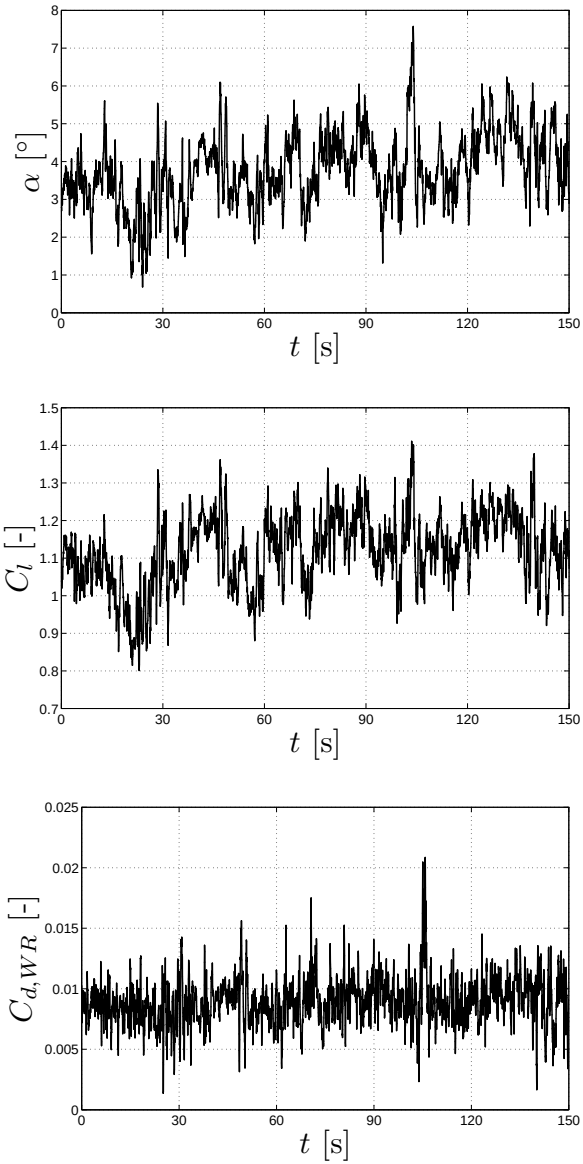

Figure 6.9.: Measured angles of attack, lift coefficients from unsteady pressure measurements and drag coefficients form the wake measurements in circling flight.

and the receptivity theory by Bertolotti is not applicable in this flight condition. A second indirect evidence that no premature transition with a considerable increase in viscous drag occurs can be found in Figure 6.9 which shows the time-dependent course of α,c_l and c_d from the wake rake measurements. The mean values for this measurement in the turbulent environment within a termal are $c_{l,mean} = 1.1$ and $c_{d,mean} = 0.009$. This pair of values is also found in the measured wing glove polar which was obtained in steady reference measurements in a low-turbulence environment, see Figure 5.12(c). Therefore, it can be stated that airfoil drag does not increase in elevated levels of atmospheric turbulence in the upper region of the laminar drag bucket. This is true as long as the laminar drag bucket is not left in case of an AoA increase as a result of a gust.

In order to investigate the effects of high AoAs on the glove, a wing stall was induced at t=102 sec in this measurement. The low flight velocity before the stall, followed by a sudden increase in velocity as result of the pitch down after the stall, can be seen Figure 6.6. The glove is still not stalled in this flight condition but the AoA is high enough that the laminar drag bucket is left and consequently the airfoil drag increases significantly. It can be concluded from the drag breakdown of the G109b shown in Figure 5.14 that a permanent doubling of airfoil drag in this flight condition would increase the total drag of the airplane about 15%.

This is a relevant finding for glider applications because many glider pilots tend to fly as slow as possible in a thermal in order to minimize the turn radius and use the stronger updraft in the center of the thermal. Flying at a very high AoA the laminar drag bucket is left frequently due to gusts which results in a considerably increased airfoil drag in average. It can be seen in Figure 6.9 that for an unsteady AoA below 5.5° no considerable increase in airfoil drag is found whereas the drag increases considerably if an AoA of 6° is exceeded.

A persistent airfoil drag increase is not found in the glove measurements due to fact that the wing reaches its lift limit before the glove does. However, there is a clear evidence that the airfoil drag increases frequently in circling flight on a glide wing using this airfoil or the original *DU84-158* airfoil because the airfoil is operated at a higher AoA. A mean c_d value of 0.015 instead of 0.009 for example, which is plausible if the average AoA is increased by 2°, would lead to total drag increase of about 9% in this flight condition. Since the drag coefficient is contained to the power of one in Equation 5.24, the sink rate linearly depends on

the total drag coefficient. Hence, a sink rate increase of 9% would result in this example.

It has been shown that neglecting the airfoil drag as proposed by Boermans in the quasi-stationary lift effects theory on the performance loss is not an appropriate simplification. The lift coefficients calculated from the measured pressure distributions are used to investigate whether a quasi-stationary lift treatment is appropriate or an unsteady treatment is required.

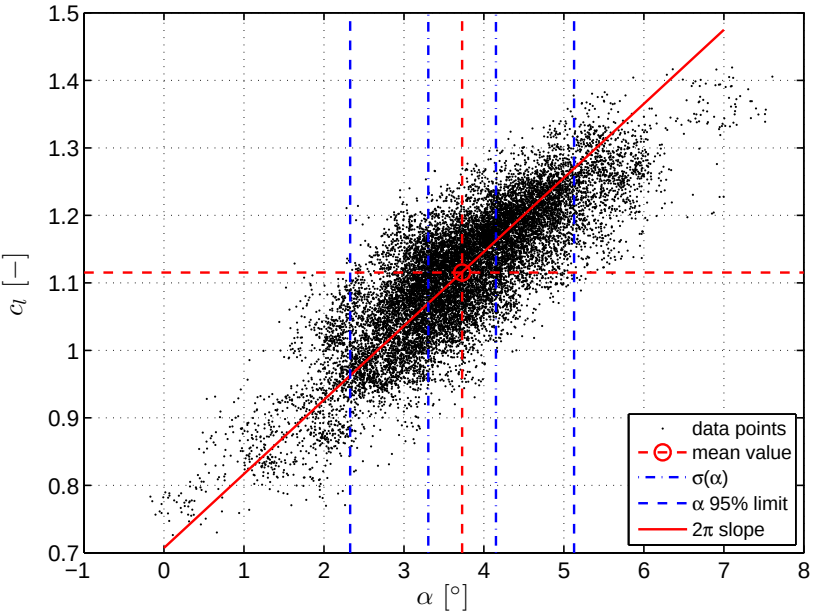

Figure 6.10.: Measured lift coefficients as function of the angle of attack.

The lift coefficient as a function of the AoA is depicted in Figure 6.10. Since the pressure measurements have a lower temporal resolution compared to the hotwire measurements, only 200 data points per second are calculated from the measurement data. Consequently, the time step is 5 milliseconds which is in the order of the propagation time of sound over the glove. It has been shown in Table 3.5 that the unsteady pressure measurement system has a temporal resolution roughly twice that. A time shift between AoA measurement and lift pressure measurement considers the convection time from the hotwire probe to the center of

the glove.

A considerable scatter of the data points can be seen in Figure 6.10. If a quasi-stationary lift treatment was applicable, the data scatter deviating from the stationary lift curve would have to be only minor in lift direction as result of measurement inaccuracies. This is a clear evidence that a quasi-stationary lift treatment does not describe the lift over the course of time correctly under turbulent conditions. Another evidence that not a quasi-stationary but an unsteady lift treatment is applicable is the fact that the data points are aligned with the theoretical lift slope of 2π in potential flow and not with the lift slope of the airfoil in steady conditions, which is in the order of 1.6π. At the upper and lower end of the AoA range the data points are tilted towards the lower slope of the steady lift curve because these extreme values correspond to long-wave disturbances. These disturbances have lower frequencies permitting a quasi-stationary treatment.

The standard deviation of α as well as the 95% limit of $\Delta\alpha$ is also depicted in Figure 6.10. From the view on the data points it is clear that the standard deviation has no practical significance whereas the 95% limit of $\Delta\alpha$ clearly limits the mean range of measured data.

Because an unsteady treatment of the lift effects seems to be appropriate, measured data is compared to different theoretical approaches using the thin-airfoil theory, namely the Wagner function (Equation 3.11) and the Küssner function (Equation 3.13). Küssner tackles the problem of finding the transient lift response on a thin airfoil entering a sharp-edged gust. Therefore, the AoA changes progressively as the airfoil penetrates into the gust whereas in Wagner's approach, the AoA changes instantaneously over the whole chord.

To compare the unsteady approaches, the lift coefficients are calculated using the two different approaches from the measured AoA time series and are compared to the measured lift coefficients. The results are shown in Figure 6.11. The time interval is selected to include the highest AoA in the measurement. Both approaches predict a similar lift coefficient compared to the measured lift coefficient. It is not possible to judge which approach delivers better results from this point of view.

Instead of plotting a time series, all data points from the lift measurements are compared to the calculated lift coefficients. The results are shown in Figure 6.12. In this depiction it is clearly visible that the Küssner function is a better approximation. It is assumed that the reason for the better approximation is the more realistic assumption of a progressive penetration of the gust.

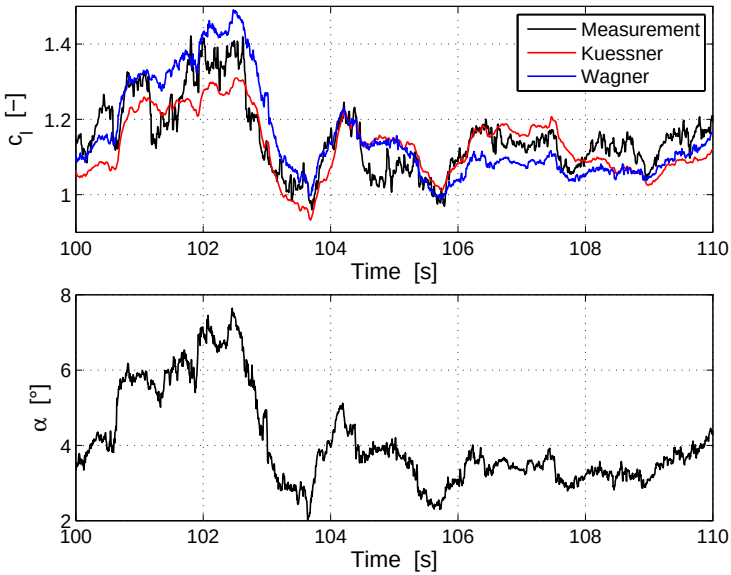

Figure 6.11.: Time series of angle of attack as well as measured and calculated unsteady lift coefficients.

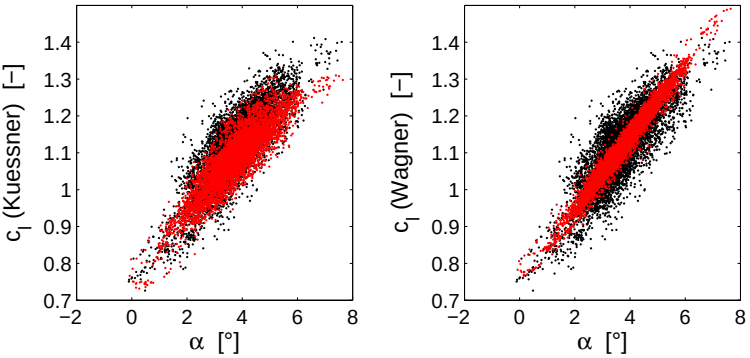

Figure 6.12.: Comparison of measured (black) and calculated (red) lift coefficients as function of the angle of attack.

In summary, it can be stated that the calculation of the unsteady lift coefficient using the Küssner function is a good approximation. The lift effects beyond the linear lift range could not be investigated. Therefore, stronger turbulence, which results in further increased AoA variations, is required using the current wing glove. Although an unsteady approach to lift is required, using the stationary lift polar gives a good indication when the laminar drag bucket is exceeded and airfoil lift increases. An increased airfoil drag indicating a premature transition has not been found in slow flight.

6.2.3. Recommendations

The recommendation for the pilot to overcome the performance problem is very simple. The mean AoA within a thermal must be decreased slightly so that a sufficient margin for AoA variations is kept before the laminar drag bucket is exceeded. For typical meteorological conditions in flat mountainous terrain a margin in the order of $2-3°$ seems sufficient. However, the pilot is not provided with a means of AoA measurement in standard aircraft instrumentation, hence the flight velocity is a preferred measure. Since velocity is contained to the power of two in the lift equation whereas the AoA is contained to the power of one, only a slight increase in velocity is required to decrease the AoA. This can also be seen in the flight envelope (Figure 5.10). Although the turn radius increases with the velocity to the power of two, in most cases this disadvantage does not outweigh the negative influence of an increased drag and the higher probability of a stall due to a strong gust with a considerable altitude lost.

A technical solution to this problem could be a device similar to a stall warning. Measuring either the standard deviation of the velocity or the standard deviation of the vertical acceleration, the actual turbulence intensity could be determined. Consequently, the warning limit could be adjusted to the actual turbulence level. A higher speed and a lower AoA must be targeted with increasing turbulence level so that the laminar drag bucket is not exceeded.

6.3. Cruise Flight under Turbulent Conditions

6.3.1. Glide

Interthermal glide is a flight segment in contrast to circling in soaring. The flight path and the inflow conditions of an exemplary flight are

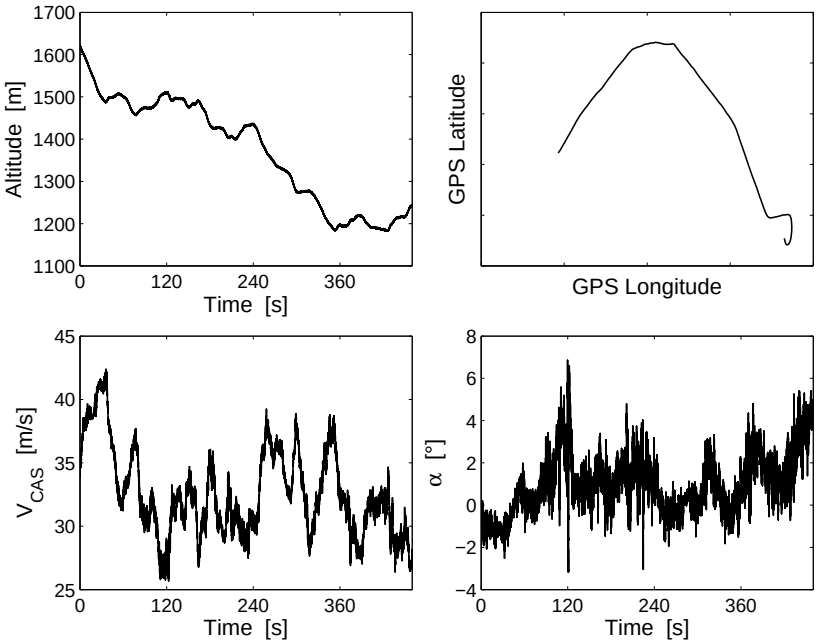

Figure 6.13.: Flight path and inflow conditions for an interthermal glide.

shown in Figure 6.13. It should be noted that the meteorological conditions are the same as in the exemplary circling flight because this glide is the subsequent flight segment to the circling flight shown before. Only the differences to circling flight will be outlined in the following.

The flight condition in glide varies over a wide speed range if the speed-to-fly theory is applied as in the exemplary flight. A detailed view of AoA as well as airfoil lift and drag coefficient is given in Figure 6.14. The first segment is glide at high speeds and low AoA before speed is decreased in an updraft due to the speed-to-fly theory. Intense AoA variations are found flying through the center of the thermal at low speeds.

The airfoil drag in cruise flight is considerably lower at low AoA compared to slow flight. The scatter in the measured drag values increases with increased variations in AoA and consequent lift. The mean value of the drag coefficient tends to follow the lift as predicted by the steady airfoil polar. The drag values for low AoA as well as high AoA are comparable to the values from the airfoil measurements in the low-turbulence

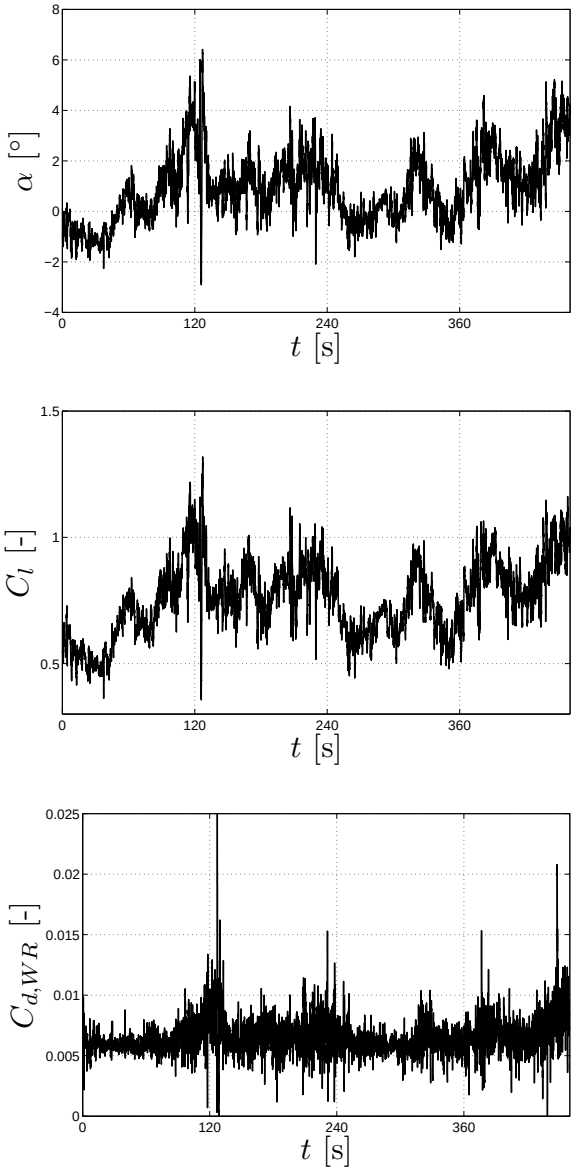

Figure 6.14.: Measured angles of attack, lift coefficients from unsteady pressure measurements and drag coefficients form the wake measurements in glide.

environment. As there is no exact time synchronization between lift and drag measurements, lift and drag are not plotted against each other because this does not yield reliable results. Nevertheless, there is no evidence in the drag measurements for a considerable drag increase due to premature transition although this is much more probable on the pressure side of the airfoil at low AoA. The pressure gradient for low AoA is adverse with an amplification of disturbances in the boundary-layer starting at 0.2x/c. The processes in the boundary-layer could not be examined due to the malfunction of numerous microphone sensors. A comprehensive investigation of the processes in the boundary-layer, especially on the pressure side of the airfoil, is an essential element in the ongoing research project beyond this study.

6.3.2. Powered Cruise Flight

The flights that were discussed before were soaring flights with the engine shut down. It will be shown in the following that atmospheric turbulence also influences powered cruise flight. Figure 6.15 gives an overview of the inflow conditions for three flights. These flights were carried out in an early phase of the flight measurements without the wake rake so that no drag data is available. Nevertheless, the inflow conditions give a good overview of the different meteorological conditions which can prevail in flight.

The flights are level flights in a straight line at the same day in the same local area with a duration of five minutes in each case. Three constant altitudes are flown in different atmospheric conditions. In the left case the flight altitude is chosen above the temperature inversion. This condition is called "slight turbulence" because the turbulence level is higher compared to measurements in a stable high pressure weather condition at high altitudes in the early morning. The second flight is in the altitude of the temperature inversion and called "light turbulence". The third flight is at the lowest altitude within the convective boundary-layer with increased turbulence level.

Whereas the slight turbulence case shows typical conditions which are required for steady in-flight measurements, intermittent turbulence and a slightly increased turbulence intensity is found in the altitude of the temperature inversion. Below the inversion turbulence intensity with all its consequences increases considerably. Generally, the lower limit of the laminar drag bucket can be exceeded in cruise flight. Typically, the highest cruise speeds are related to AoAs close to the lower limit.

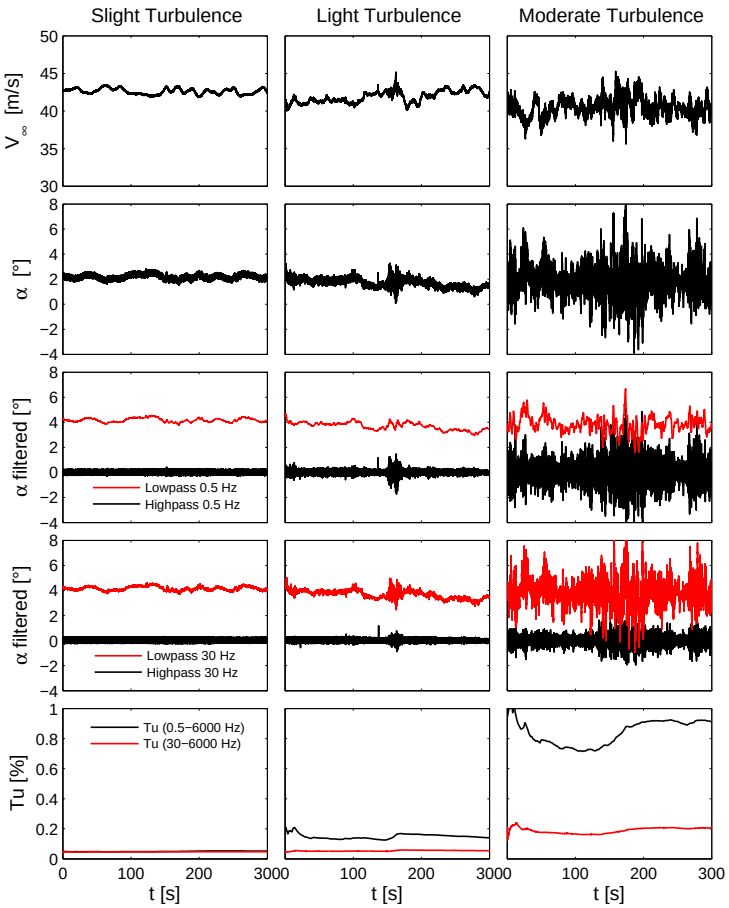

Figure 6.15.: Straight line horizontal flights at different altitudes. In-flight measurements of atmospheric turbulence under, in and above an inversion.

Therefore, the same effects as in slow flight are expected.

The inflow conditions shown in Figure 6.15 demonstrate the applicability of a flight procedure that is proposed for the in-deep investigation of the atmospheric turbulence on the boundary-layer in the ongoing research project beyond this study. Prescribing the pressure gradient and consequently the stability of the boundary-layer on the pressure side of the airfoils is possible through the selection of an appropriate steady AoA. Much attention has been paid to this aerodynamic feature in the design of the wing glove. Slight altitude variations in powered flight close to a temperature inversion can be used to increase the turbulence intensity gradually. This procedure for which thermal convection without cumulus clouds is required allows good control of the flow conditions on the glove as well as the atmospheric turbulence intensity. It must be noted that for this flight procedure a measurement system for the boundary-layer state is required which is usable in powered flight, e.g. hotfilm arrays.

6.4. Evaluation Criterion for Aerodynamic Research, Design and Flow Control Strategies

The flight test results show that the assumption of steady inflow conditions is incorrect for flight in atmospheric turbulence. The correlation between energy dissipation rate ϵ and turbulence level Tu as well as the standard deviation of the angle of attack $\sigma(\alpha)$ is shown in Figure 6.16. Every data point shows the mean values for one measurement under turbulent conditions.

Typical ϵ values for the convective boundary-layer during summer in the low mountain range are in the order of 0.005 to 0.015 $m^2 s^{-3}$ because stronger thermals can be found compared to those in the measurement flights. These values correspond to $\epsilon^{1/3}$ values of 1.7 and 2.45 $cm^{2/3} s^{-1}$ for a better comparison with the values shown in Figure 2.10. Tu as well as $\sigma(\alpha)$ increase with an increasing energy dissipation rate. This is a clear statistical correlation between aerodynamics and meteorology. Only the magnitude of the values depends on the flight velocity.

Tu and $\sigma(\alpha)$ both increase with energy dissipation rate. Therefore, $\sigma(\alpha)$ is plotted as function of Tu which is shown in Figure 6.17. The data points of 12 measurements show an obvious correlation and the linear fit through the data points is also plausible because a certain variation in AoA is always present, even in non-turbulent conditions. This is an important finding to evaluate experiments in aerodynamic research with

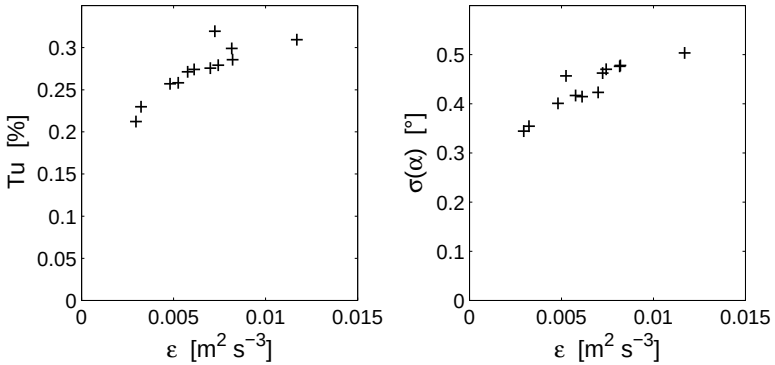

Figure 6.16.: Turbulence level, angle of attack standard deviation as function of dissipation rate. Each data point shows the mean values of one measurement under turbulent conditions.

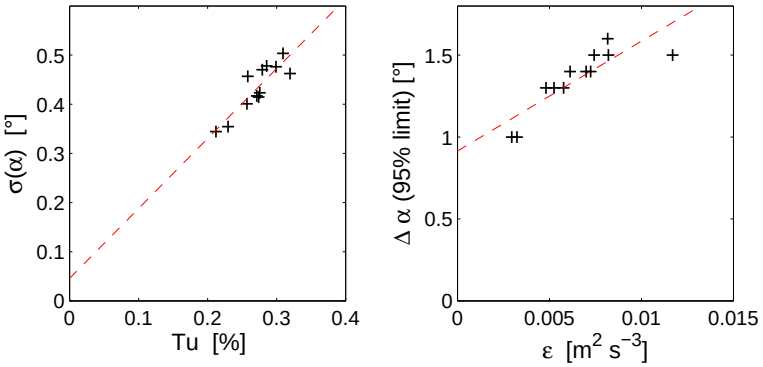

Figure 6.17.: Turbulence level as function of angle of attack standard deviation and angle of attack variations as function of dissipation rate. Each data point shows the mean values of one measurement under turbulent conditions.

regard to their relevance to practical aircraft applications under realistic atmospheric conditions.

An elevated level of micro-scale turbulence, which is expressed through

the turbulence level Tu, is always related to an increased $\sigma(\alpha)$ in free flight in the atmosphere. This is a clear contradiction to the assumption of an invariable pressure distribution which is used in most receptivity experiments. Turbulence levels of 0.5% and more, which change transition scenarios according to the results from flat plate experiments in transition research, do not occur in light atmospheric turbulence. Negligible or light turbulence is the prerequisite for a pressure distribution which is at least almost invariable. Any theory that contains the basic assumptions of a steady pressure distribution and an elevated level of turbulence simultaneously cannot be transferred to the flight case without a validation in unsteady pressure distributions.

Another important correlation is shown in the right plot of Figure 6.17. Not only the standard deviation of the AoA is correlated with energy dissipation rate but also the more practice-oriented 95% limit of the AoA variations is correlated with ϵ. Using a linear fit shows that there are still AoA variations in non-turbulent conditions. This is consistent with the histogram plot of the AoA variations for a low-turbulence environment shown in Figure 6.3.

In most cases, aircraft are developed with some typical steady operating points in mind and the design is optimized regarding to this operating points. If the project performance is only achieved in a very narrow range around the design operating point, e.g. close to the limits of the laminar drag bucket, the project's performance is not achieved under the influence of turbulence. This is also an important aspect in the transferability of flow control experiments to realistic flight conditions. Many flow control experiments are conducted under well-controlled and constant flow conditions in the wind tunnel. As a result of the unsteady measurements in atmospheric turbulence, a simple evaluation criterion for the applicability of an aerodynamic design or flow control strategy under realistic atmospheric conditions can be derived.

Typical AoA variations are related to aircraft characteristics and atmospheric turbulence intensity, see Figure 6.17. The aircraft design or any means of flow control must not only work at the design AoA and the respective flow condition but also at every AoA within the variation range. A simple approach to take this requirement into account is to define the design operation point and use the 95% limit of the AoA variations as the operating range. The flow conditions related to these AoAs must be considered in the design. This way the AoA variations relevant to performance are included whereas the extreme values due to singular occurrences are excluded.

In addition, a means of active flow control must be able to deal with fast changes of the flow conditions within the entire AoA range. It can be seen in the highpass filtered AoA signal that AoA oscillations with magnitudes in the order of the 95% $\Delta\alpha$ have time constants in the order of tens of seconds. Therefore, any means of active flow control must be able to adjust to a fast changing base flow.

If these two requirements are not fulfilled, a design or means of flow control may work in flight in a non-turbulent environment but it will not perform properly under realistic atmospheric conditions.

7. Conclusions and Future Work

In the present study the influence of atmospheric turbulence on aircraft performance has been investigated and a relation between flight physics and meteorology has been established. Special attention was paid on aircraft with natural laminar flow airfoils because they exhibit an additional possibility of performance loss due to increased drag caused by a premature laminar-turbulent transition.

A theoretical analysis was performed and the aerodynamic problem was extracted from the performance problem. A new wing glove for the G109b measurement aircraft as well as measurement equipment capable of detecting unsteady aerodynamic effects were developed. In-flight measurements for the validation of performance loss theories were carried out resulting in a new approach to aircraft performance under turbulent atmospheric conditions.

Theoretical Analysis

The theoretical analysis showed that atmospheric turbulence in the atmosphere's convective boundary-layer is described through the inertial subrange from Kolmogorov's theory for turbulent flows. Transferred to the aerodynamic problem, this means that angle of attack variations and small-scale turbulence inevitably coexist in atmospheric turbulence.

Generally, a loss of flight performance can be the result of decreased lift, increased drag or a combination of both. The aerodynamic state and therefore the possible influencing mechanisms of atmospheric turbulence vary with the flight condition. Based on aircraft performance considerations, three principal flight conditions were determined for an in-depth study of the aerodynamic state related to these flight conditions. The flight conditions are slow flight, best glide and cruise flight.

Research Aircraft and Measurement Equipment

A new wing glove with favorable characteristics for aerodynamic in-flight experiments, retaining the flying qualities of the aircraft besides the asymmetric configuration, has been designed. A survey of the base flow on the glove in non-turbulent conditions by means of flight tests,

wind tunnel tests and numerical simulations was conducted prior to the investigations under turbulent conditions. The results were essential as baseline data and showed that the numerous design requirements for the new wing glove were fulfilled.

A cost-effective measurement system capable of measuring unsteady aerodynamic was designed. The ambient air data system for the steady inflow conditions, the hotwire probes for the unsteady inflow conditions, the steady and unsteady pressure sensors as well as the wake rake proved to be reliable in flight. Despite promising results in preliminary tests, the transition detection system by means of wall-mounted microphones proved to be unreliable in flight and data could not be evaluated.

Flight Test Results

The flight test results show that the assumption of steady inflow conditions is incorrect for flight in atmospheric turbulence. An elevated level of micro-scale turbulence in the atmosphere is related to increased angle of attack variations and vice versa. Therefore, unsteady changes in the airfoil pressure distribution are prevalent when an elevated turbulence level is encountered. Turbulence levels of 0.5% and more, which lead to different transition scenarios according to the results from flat plate experiments in transition research, do not occur in light atmospheric turbulence, which is in turn the prerequisite for almost steady pressure distributions.

The unsteady lift variations related to the angle of attack variations due to gusts are well predicted by unsteady thin-airfoil theory. A quasi-stationary approach does not cover the entire unsteady lift effects but in the case of laminar airfoils it predicts when the laminar drag bucket is left and airfoil drag increases. Especially in slow flight very close to the upper limit of the laminar drag bucket, angle of attack variations lead to increased airfoil drag.

From the pilot point of view, flying at a lower angle of attack simply solves this problem. Only a slight increase in velocity is required to lower that angle of attack sufficiently. The conclusion for the aircraft designer is that a sufficient distance between the design point to the limit of the laminar drag bucket must be taken into account to allow for the influences of gusts and also for the impossibility to fly at a perfectly constant angle of attack.

Evaluation Criterion for Aircraft Design and Flow Control Strategies

An important question in aircraft design and flow control is, if the performance goals are met not only under ideal conditions but also under realistic flight conditions. A simple evaluation criterion was found. Typical angle of attack variations are related to aircraft characteristics and atmospheric turbulence level. The aircraft design or any means of flow control must not only work at the design angle of attack and the respective flow condition but also at every angle of attack within the variation range. In addition, a means of flow control must be able to deal with fast changes within the entire angle of attack range. If these two requirements are not fulfilled, a design will not work properly under realistic atmospheric conditions.

Future Work

As a result of the unreliability of the wall microphones for transition detection a more reliable means of transition detection must be developed and integrated in the future.

Additional flights are required to investigate the behavior in the lower part of the lift range at the lower limit of the laminar drag bucket. Another important aspect is the angle of attack distribution in spanwise direction in atmospheric turbulence. An increased induced drag seems possible due to a lift distribution deviating from the normal lift distribution.

Bibliography

[1] L. L. M. Boermans. Improvement of sailplane climb performance by airfoil design. In *XXIX OSTIV Congress, Lüsse, Germany*. Technical Soaring, 2008.

[2] F. P. Bertolotti. Effect of atmospheric turbulence on a laminar boundary-layer. In *XXVI OSTIV Congress, Bayreuth, Germany, 6-13 August 1999*, 1999.

[3] S. Bernardy. Investigation into the effects of turbulence in thermals on sailplane airfoil performance. Master's thesis, Delft University of Technology, 2002.

[4] M. Eshelby. *Aircraft Performance, Theory and Practice*. Arnold Pubishers, 2000.

[5] F. Thomas. *Fundamentals of Sailplane Design*. College Park Press, 1999.

[6] *Standard Atmosphere*. International Organization for Standardization, ISO 2533:1975, 1975.

[7] R. D. Kimberlin. *Flight Testing of fixed-wing Aircraft*. AIAA Education Series. American Institute of Aeronautics and Astronautics, 2003.

[8] J. D. Anderson. *Fundamentals of Aerodynamics*. McGraw-Hill, 2001.

[9] H. Schlichting and E. Truckenbrodt. *Aerodynamik des Flugzeuges*. Springer, 2001.

[10] H. Schlichting and K. Gersten. *Grenzschicht-Theorie*. Springer, 10th edition, 2005.

[11] D. Althaus. *Stuttgarter Profilkatalog 2: Niedriggeschwindigkeitsprofile*. Viehweg, 1996.

[12] M. Drela. XFOIL: An analysis and design system for low reynolds number airfoils,. In *Proceedings of Conference on Low Reynolds Number Airfoil Aerodynamics, University of Notre Dame*, June 1989.

[13] R. Eppler. *Airfoil Design and Data*. Springer, 1990.

[14] D. Althaus and F. X. Wortmann. *Stuttgarter Profilkatalog 1*. Viehweg, 1981.

[15] L. M. M. Boermans and H .J. W. Selen. On the design of some airfoils for sailplane application. Technical Report LR-326, Delft University of Technology, Department of Aerospace Engineering, 1981.

[16] B. J. Holmes, C. J. Obara, and L. P. Yip. Natural laminar flow experiments on modern airplane surfaces. Technical Paper 2256, NASA, 1984.

[17] C. J. Obara and B. J. Holmes. Roughness and waviness requirements for laminar flow surfaces. *Langley Symposium on Aerodynamics*, 1:519–537, 1986.

[18] B. J. Holmes, C. J. Obara, G. L. Martin, and C. S. Domack. Manufacturing requirements. In *Laminar Flow Aircraft Certification*, NASA CP-2413, pages 171–183, 1986.

[19] S. S. Dodbele, C. P. Vandam, and P. M. H. W. Vijgen. Design of fuselage shapes for natural laminar flow. Contractor Report 3970, NASA, 1986.

[20] B. J. Holmes, C. C. Croom, E. C. Hastings, C. J. Obara, and C. P. Vandam. Flight research on natural laminar flow. *Langley Symposium on Aerodynamics*, 1:461–474, 1986.

[21] H. Reichmann. *Streckensegelflug*. Motorbuch Verlag, 8th edition, 1993.

[22] T. R. Yechout, W. F. Hallgren, D. E. Bossert, and S. L. Morris. *Introduction to Aircraft Flight Mechanics: Performance, Static Stability, Dynamic Stability, and Classical Feedback Control*. AIAA Education Series. American Institute of Aeronautics and Astronautics, 2003.

[23] G.V. Lachmann. Aspects of insect contamination in relation to laminar flow aircraft. A.R.C. Technical Report C.P. No. 484, Aeronautical Research Council, 1960.

[24] C. C. Croom and B. J. Holmes. Insect contamination protection for laminar flow surfaces. *Langley Symposium on Aerodynamics*, 1:539–556, 1986.

[25] R. H. Johnson. A flight test evaluation of the LS-3. *Soaring Magazine*, 43:26–33, November 1978.

[26] J. P. Walter. Debris removal system and method for wind turbine blades. US Patent 2009/0297352 A1, December 2009.

[27] J. J. Chung and H. E. Addy. A numerical evaluation of icing effects on a natural laminar flow airfoil. AIAA Paper 2000-0096, 2000.

[28] *Advisory Cicular 23-8B - Flight Test Guide for Certification of Part 23 Airplanes*. Federal Aviation Authority, August 2003.

[29] J.G. Leishman. *Principles of Helicopter Aerodynamics*. Cambridge University Press, 2 edition, 2006.

[30] *Certification Specifications for Sailplanes and Powered Sailplanes (CS-22)*. European Aviation Safety Agency, March 2009.

[31] *Certification Specifications for Normal, Utility, Aerobatic, and Commuter Category Aeroplanes (CS-23)*. European Aviation Safety Agency, September 2010.

[32] *14 CFR - Part 23 - AIRWORTHINESS STANDARDS: NORMAL, UTILITY, ACROBATIC, AND COMMUTER CATEGORY AIRPLANES*. Federal Aviation Administration, December 2008.

[33] P. B. MacCready. Standardization of gustiness values from aircraft. *Journal of Applied Meteorology*, 3(4):439–449, 1964.

[34] R. L. Bowles and B. K. Buck. A methodology for determining statistical performance compliance for airborne doppler radar with forward-looking turbulence detection capability. Contractor Report CR-2009-215769, NASA, June 2009.

[35] J.B. Prince, B. K. Buck, P. A. Robinson, and T. Ryan. In-service evaluation of the turbulence auto-pirep system and enhanced turbulence radar technologies. Contractor Report CR-2007-214887, NASA, July 2007.

[36] *Aeronautical Information Manual*. Federal Aviation Administration, 2010 edition.

[37] M. Fujino. Development of the HondaJet. In *Proceeding of the 24th Congress of the International Council of the Aeronautical Sciences, August 29-September 3, Yokomhama, Japan*, 2004.

[38] M. Fujino, Y. Yoshizaki, and Y. Kawamura. Natural-laminar-flow airfoil development for a lightweight business jet. *Journal of Aircraft*, 40(4):609–605, 2003.

[39] J. K. Viken, S. A. Watson-Viken, W. Pfenninger, H. L. Morgan, and R. L. Campbell. Design of the low-speed NLF(1)-0414f and the high-speed HSNLF(1)-0213 airfoils with high-lift systems. In *Research in Natural Laminar Flow and Laminar-Flow Control, Part 3*, NASA CP-2487, pages 637–671, 1987.

[40] G. Sachs. Minimum shear wind strength required for dynamic soaring of albatrosses. *Ibis*, 147(1):1–10, January 2005.

[41] G. Sachs, J. Traugott, and F. Holzapfel. In-flight measurement of dynamic soaring in albatrosses. In *AIAA Guidance, Navigation, and Control Conference, Toronto, Ontario Canada, 2 - 5 August*, number AIAA 2010-8035, 2010.

[42] J. Wharington and I. Herszberg. Control of high endurance unmanned air vehicle. In *Procedings of the 21st Congress of International Council of the Aeronautical Sciences, Melbourne, Australia, 13-18 September*, 1998.

[43] M. J. Allen. Guidance and control of an autonomous soaring UAV. Technical Report TM-2007-214611, NASA Dryden Flight Research Center, 2007.

[44] M. J. Allen. Guidance and control for an autonomous soaring UAV. US Patent 7,431,243 B1, October 2008.

[45] K. Andersson, I. Kaminer, and K. D. Jones. Autonomous soaring; flight test results of a thermal centering controller. In *AIAA Guidance, Navigation, and Control Conference, Toronto, Ontario Canada, 2 - 5 August*, number AIAA 2010-8034, 2010.

[46] Z. Akos, M. Nagy, S. Leven, and T. Vicsek. Thermal soaring flight of birds and unmanned aerial vehicles. *Bioinspiration & Biomimetics*, 5(4):045003, 2010.

[47] C. K. Patel, H.-T. Lee, and I. M. Kroo. Extracting energy from atmospheric turbulence. In *XXIX OSTIV Congress, Lüsse-Berlin, Germany, 6 August - 13 August 2008*, 2008.

[48] C. K. Patel and I. M. Kroo. Theoretical and experimental investigation of energy extraction from atmospheric turbulence. In *Proceeding of the 26th Congress of the International Council of the Aeronautical Sciences, 14 19 September, Anchorage, Alaska, USA*, 2008.

[49] A. Chakrabarty and J. W. Langelaan. Flight path planning for UAV atmospheric energy harvesting using heuristic search. In *AIAA Guidance, Navigation, and Control Conference, Toronto, Ontario Canada, 2 - 5 August*, number AIAA 2010-8033, 2010.

[50] Y. J. Zhao. Optimal patterns of glider dynamic soaring. *Optimal Control Applications and Methods*, 25(2):67–89, March/April 2004.

[51] P. P. Sukumar and M. S. Selig. Dynamic soaring of sailplanes over open fields. In *28th AIAA Applied Aerodynamics Conference, Chicago, Illinois USA, 28 June - 1 July*, number AIAA 2010-4953, 2010.

[52] Y. J. Zhao and Y. C. Qi. Minimum fuel powered dynamic soaring of unmanned aerial vehicles utilizing wind gradients. *Optimal Control Applications and Methods*, 25(5):211–233, September/October 2004.

[53] E. Hau. *Windkraftanlagen. Grundlagen, Technik, Einsatz, Wirtschaftlichkeit.* Spring, 3 edition, 2008.

[54] D. Etling. *Theoretische Meteorologie. Eine Einfhrung.* Springer, 3rd edition, 2008.

[55] R. D. Stull. *An Introduction to Boundary Layer Meteorology.* Kluwer, 1988.

[56] J. C. Wyngaard. Atmospheric turbulence. *Annual Review of Fluid Mechanics*, 24:205–233, 1992.

[57] S. B. Pope. *Turbulent Flows.* Cambridge University Press, 2000.

[58] G. K. Batchelor. The application of the similarity theory of turbulence to atmospheric diffusion. *Quarterly Journal of the Royal Meteorological Society*, 76:133–146, April 1950.

[59] P. B. MacCready. Turbulence measurements by sailplane. *Journal of Geophysical Research*, 67(3):1041–1050, 1962.

[60] P. B. MacCready. The inertial subrange of atmospheric turbulence. *Journal of Geophysical Research*, 67(3):1051–1059, 1962.

[61] H. Riedel and M. Sitzmann. In-flight investigations of atmospheric turbulence. *Aerospace Science and Technology*, 2(5):301–319, 1998.

[62] B. Y. Zanin. Transition at natural conditions and comparison with the results of wind tunnel studies. In V. V. Kozlov, editor, *Laminar-Turbulent Transition*, pages 541–546. Springer, 1984. IUTAM Symposium Novosibirsk 1984.

[63] L. M. Mack. Transition and laminar instability. CP 153203, NASA, 1977.

[64] Y. S. Kachanov. Physical mechanisms of laminar-boundary-layer transition. *Annual Review of Fluid Mechanics*, 26:411–482, 1994.

[65] W. S. Saric, H. L. Reed, and E. J. Kerschen. Boundary-layer receptivity to freestream disturbances. *Annual Review of Fluid Mechanics*, 34:291–319, 2002.

[66] P. W. Hammerton and E. J. Kerschen. Leading-edge receptivity for bodies with mean aerdynamic loading. *Journal of Fluid Mechanics*, 535:1–32, 2005.

[67] A. Seitz. Freiflug-Experimente zum Übergang laminar-turbulent in einer Tragflügelgrenzschicht. Forschungsbericht 2007-01, Deutsches Zentrum für Luft- und Raumfahrt, Institut für Aerodynamik und Strömungstechnik, 2007.

[68] H. F. Fasel. Numerical investigation of the interaction of theKlebanoff-mode with a Tollmien-Schlichting wave. *Journal of Fluid Mechanics*, 450:1–33, 2002.

[69] W. J. McCroskey. Unsteady airfoils. *Annual Review of Fluid Mechanics*, 14:285–311, 1982.

[70] W. Nitsche and A. Brunn. *Strömungsmesstechnik*. Springer, 2 edition, 2005.

[71] P. Erb. *Untersuchung der Grenzschichttransition im Flugversuch*. PhD thesis, Technische Universität Darmstadt, 2002.

[72] F. Hardt. Entwurf einer Sonde zur Bestimmung des Anstellwinkels für das Forschungsflugzeug G-109b. Studienarbeit, Technische Hochschule Darmstadt, 1996.

[73] V. Arnold. Calibration and testing of a hot wire probe for atmospheric turbulence measurements in a wind tunnel. Studienarbeit, Technische Universität Darmstadt, 2008.

[74] J. Schnell. Konstruktive Auslegung von Druckmessleitungen für das Forschungsflugzeug G-109b. Studienarbeit, Technische Hochschule Darmstadt, 1996.

[75] A. R. Sinclair and A. W. Robins. A method for the determination of the time lag in pressure measuring systems incorporating capillaries. Technical Note 2793, National Advisory Commitee for Aeronautics, September 1952.

[76] W. Nitsche, J. Suttan, S. Becker, P. Erb, M. Kloker, and C. Stemmer. Untersuchung des laminar-turbulenten Strömungsumschlags im Freiflug. Abschlussbericht zum DFG-Hochschulverbundvorhaben. Technical report, RWTH Aachen, TU Berlin, TU Darmstadt, Uni Erlangen, Uni Stuttgart, 1999.

[77] W. Nitsche, J. Suttan, S. Becker, P. Erb, M. Kloker, and C. Stemmer. Experimental and numerical investigations of controlled transition in low-speed free flight. *Aerospace Science and Technology*, 5:245–255, 2001.

[78] I. Peltzer. *Flug- und Windkanalexperimente zur räumlichen Entwicklung von Tollmien-Schlichting-Instabilitäten in einer Flügelgrenzschicht*. PhD thesis, Technische Universität Berlin, 2004.

[79] M. Roth. *Kalibration und Einsatz von Heissfilmarrays im Flugversuch*. PhD thesis, Technische Universität Darmstadt, 2003.

[80] K. Barckmann. Design, construction and testing of an in-flight measurement system for the detection of boundary-layer transition. Master's thesis, Technische Universität Darmstadt, 2008.

[81] *Gerätekennblatt Nr. 817, Muster: Grob G109*. Luftfahrtbundesamt, 11th edition, August 1995.

[82] *Flughandbuch Grob G109b, Triebwerk: Limbach L2400DT1*. Korff + Co. KG, 1st edition, March 2002.

[83] *Joint Aviation Requirements, JAR-22: Sailplanes and Powered Sailplanes.* Joint Aviation Authorities, April 1982.

[84] A. Winterfeld. Auslegung und Konstruktion einer schwingungsisolierten Instrumentierungs-Plattform für das Forschungsflugzeug G-109b. Studienarbeit, Technische Hochschule Darmstadt, 1988.

[85] *Anhang zum Flughandbuch G109b, K-KDLA, Messflugzeug, 850 kg Höchstabfluggewicht.* Technische Universität Darmstadt, 1st edition, July 1997.

[86] *Grob G109b D-KDLA, Messflugzeug mit erhöhtem Abfluggewicht von 950 kg.* Technische Universität Darmstadt.

[87] V. Sommer. Nachrechnung der Betriebsbereichsgrenzen des Forschungsflugzeugs G-109b. Diploma thesis, Technische Hochschule Darmstadt, 1995.

[88] W. Friedrichs. Research on models for fast angle of attack variations on an airfoil under turbulent atmospheric conditions. Master's thesis, Technische Universität Darmstadt, 2009.

[89] O. Böpple. Measuring system calibration on the G109b research aircraft and characterization of reference flight attitudes. Bachelor's thesis, Technische Universität Darmstadt, 2010.

[90] A. Reeh. In-flight investigation of tollmien-schlichting waves generated through natural boundary layer receptivity mechanisms. Master's thesis, Technische Universität Darmstadt, 2009.

[91] H. H. Bruun. *Hot-wire Anemometry, Principles and signal analysis.* Oxford University Press, 1995.

[92] H. J. Goett. Experimental investigation of the momentum method for determining profile drag. Report 660, NACA, 1939.

[93] J.B. Barlow, W. H. Rae, and A. Pope. *Low-Speed Wind Tunnel Testing.* John Wiley & Sons, 3 edition, 1999.

[94] J. Schulze. Numerical simulation of various flow conditions on the G-109b research aircraft. Bachelor's thesis, Technische Universität Darmstadt, 2010.

[95] F. Loosmann. Software development for automated processing and graphical representation of in-flight measurement data. Bachelor's thesis, Technische Universität Darmstadt, 2010.

[96] D. Gray. Using gps to accurately establish true airspeed (tas). Technical report, National Test Pilot School, 1998.

[97] G. Lewis. Using gps to determine pitot-static errors. Technical report, National Test Pilot School, 2003.

[98] Flugleistungsvermessung der G109b. IDAFLIEG Berichtsheft, 1985.

[99] *Operation Instructions and Specifications NI 6259.* National Instruments Corporation, August 2009.

[100] *Operation Instructions and Specifications NI 9205.* National Instruments Corporation, February 2008.

[101] *Operating Instructions Automated Pressure Calibrator CPC 6000.* Mensor Corporation, August 2009.

[102] *Barometric, Gauge or Absolute Pressure, Model 270 Specification.* Setra Systems, May 2002.

[103] *High Accuracy/Low Range Pressure, Model 239/C239 Specifications.* Setra Systems, May 2002.

[104] *Operating Instructions and Specifications CompactRIO cRIO-9072/3/4.* National Instruments Corporation, July 2008.

[105] *Strömungsmessgeräte für den Flugversuch.* Dornier GmbH, 1985.

A. Angle of Attack Definitions

A.1. General Definitions

Generally, the angle of attack is defined as the vertical angle between the direction of the undisturbed flow field and the angle of attack reference axis. Several AoA reference axis definitions for the global aircraft as well as for the local airfoil sections are used. Furthermore in the case of three-dimensional flow is has to be distinguished between the geometric AoA α_{geo}, the effective AoA α_{eff} and the induced AoA α_{ind}

$$\alpha_{eff} = \alpha_{geo} - \alpha_{ind}. \tag{A.1}$$

Herein, all angles of attack are local values. The theoretical background of this equation can be found in text books and is not described in the following.

The local geometric AoA has not to be constant along the wing span, in many cases the wing is twisted. Furthermore, a real aircraft is not rigid and its shape changes with the load situation. Aircraft shapes are for example:

- Ground shape
- Jig shape
- 1g flight shape
- Maximum load factor flight shape

For the G109b only the wing twist for the jig shape is known. As the aeroelastic behavior is not known, the jig shape as shown in the G109b drawings is taken for all considerations and numerical calculations. It was not attempted to measure the ground shape or the flight shape. The elastic aileron deflection (due to the finite stiffness of the control system) and deformation (due to the elasticity of the aileron itself) in flight are unknown.

A.2. Global Angle of Attack

The global angle of attack is typically referenced to the aircraft longitudinal axis. This is the most comprehensive definition and it is independent of wing setting angle, wing twist along the span and aeroelastic deformations. This global angle of attack is referred to as geometric angle of attack α_{geo} within this study. All numerical simulations shown in Chapter 5.3 are referenced to the global geometric angle of attack.

A.3. Local Angle of Attack

The local angle of attack at the wing glove is of great importance as the influence of turbulence on the airfoil section is investigated. The local, effective AoA is a function of the global AoA, the induced AoA at the glove position and the geometric incidence of the glove compared to the global reference axis.

Basic Assumptions for the Local, Effective AoA at the Glove

- The flow in the center of the wing glove is considered as two-dimensional. The validity of the two-dimensional flow assumption was shown in Chapter 5.3.
- The measured pressure distribution represents the two-dimensional airfoil pressure distribution within the center section of the glove.
- The pressure distribution for the glove airfoil section is correlated with a local, effective angle of attack.
- This local, effective the angle of attack representing the two-dimensional flow around the glove airfoil is labeled $\alpha_{2D,glove}$.

Mixed Experimental-Numeric Procedure

Because the real geometric incidence angle in flight shape due to aeroelastic deformation is not known exactly and the induced angle of attack is only known from calculations, a different mixed experimental-numeric procedure is used to determine the local, effective angle of attack acting on the glove $\alpha_{2D,glove}$. This procedure involves the following steps:

1. Within the entire flight envelope (from minimum to maximum flight speed) constant flow angles at the *FlightLog* are maintained

for approximately 30 second for each measurement point and the corresponding pressure distribution at the wing glove is measured.

2. Average pressure distributions and ambient flow conditions are calculated for each measurement point. The ambient flow conditions include the Reynolds number.

3. For each measurement point pressure distributions for a range of different AoA are calculated using *xfoil*. The Reynolds numbers are set to the corresponding Reynolds numbers from the Flight measurements.

4. The best fit between measured and calculated pressure distributions is determined for each measurement point.

5. The angle of attack (*xfoil* input) which gives the best fit represents the angle of attack for the two-dimensional flow around the glove airfoil. This angle of attack is labeled $\alpha_{2D,glove}$.

6. The measured flow field angles at the *FlightLog* and hotwire are correlated to $\alpha_{2D,glove}$ and the calibration functions determined, see also Chapter 5.4.2 and B.2.3.

Figure A.1 shows an exemplary best fit between measured and calculated pressure distributions. Where not otherwise denoted in Chapters 5.5 and 6, the angle of attack α is the abbreviation for $\alpha_{2D,glove}$.

Not only in flight but also in the wind tunnel measurement three-dimensional effects and additional wall effects are present. Therefore, the same fitting procedure for the angle of attack representing the two-dimensional flow at the wing glove is used. In this case a calibration function between $\alpha_{2D,glove}$ and the incidence angle of the wind tunnel scale, to which the glove is mounted, is determined.

This procedure explains the good agreement in c_l over α between the in-flight, wind tunnel and calculated results shown in Figure 5.12.

A.4. Flow Field Angle

The systematic error in angle of attack measurements in the disturbed flow field of the wing is explained in Chapter 5.4.2 and schematically depicted in Figure 5.9(a). The local flow field angle at the point of the AoA measurement is referred to as α_{vane} because a wind vane would adjust to this direction of the flow field. For the specific location of

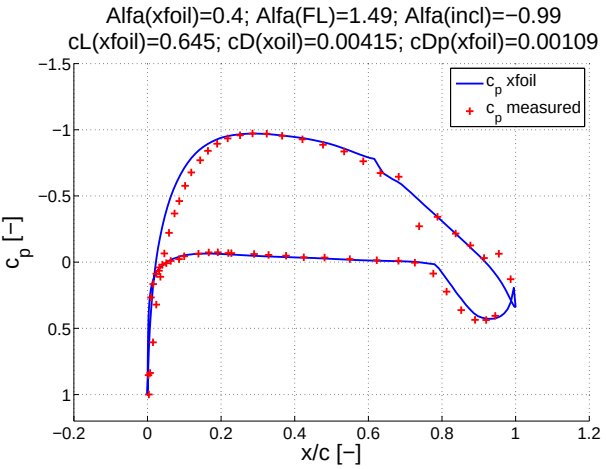

Figure A.1.: Best fit for measured glove pressure distribution with calculated 2D airfoil pressure distribution.

the *FlightLog* in front of the left wing the measured flow field angle is denoted α_{FL}, for the location of the hotwire in front of the wing glove on the right wing it is denoted α_{HW}.

B. Experimental Uncertainty Analysis

An overview on the measurement parameters used in this study has been given in Chapter 5. Measurement parameters are obtained either directly from the measurement instruments or indirectly by calculations using these basic parameters.

Generally, errors are present in all measurements. These measurement errors can be divided into two types: random errors and systematic errors. Systematic errors, which are corrected using calibration functions obtained from in-flight calibration, are shown in Chapter 5.4. A more detailed experimental uncertainty analysis including instrument errors, systematic errors and the propagation of uncertainty is given in the following.

B.1. Identification of Instrument Errors

B.1.1. Calibration Function and Errors

Generally, instrument calibration is used to give a functional relation between the measurement quantity and the physical values of sensor output. For example, a calibration curve can be made for a particular pressure transducer to determine applied pressure from transducer output, which is typically a voltage. Polynomial functions are used to approximate the calibration function. The smallest possible polynomial degree, which gives the required calibration accuracy, should be used for the calibration function in order to minimize the computational effort in post-processing.

Typically calibration data gives a set of equations with more equations than unknowns. The method of least squares is a standard approach to the approximate a solution of such an overdetermined systems. "Least squares" means that the overall solution minimizes the sum of the squares of the errors made in solving every single equation.

Data fitting is used to find the calibration function $g(x)$ for a point cloud with N points (x_ν, y_ν) of calibration data. The best fit in the least-squares sense minimizes the sum of squared residuals χ^2, a residual being the difference between an observed value y_ν and the fitted value $g(x_\nu)$ provided by a model. With the coefficients of the polynomial of

degree m given in vectorial notation $\vec{a} = (a_0, a_1, ..., a_m)^T$, the minimum criterion for the sum of squared residuals is

$$\chi^2 = \sum_{\nu=1}^{N} [y_\nu - f(x_\nu, \vec{a})]^2 \stackrel{!}{=} \min . \tag{B.1}$$

The most simple calibration function is a linear function, which is a polynomial with a degree of one.

$$g = a_1 x + a_0 \tag{B.2}$$

This yields

$$\min_{a_0, a_1} \left\| \begin{pmatrix} 1 & x_1 \\ \vdots & \vdots \\ 1 & x_N \end{pmatrix} \begin{pmatrix} a_0 \\ a_1 \end{pmatrix} - \begin{pmatrix} y_1 \\ \vdots \\ y_N \end{pmatrix} \right\|_2 = \min_{\vec{a}} \|M\vec{a} - \vec{g}\|_2 \tag{B.3}$$

With the arithmetic mean of the calibration data points $\overline{x} = \frac{1}{N} \sum_{\nu=1}^{N} x_\nu$ and $\overline{y} = \frac{1}{N} \sum_{\nu=1}^{N} y_\nu$ the least squared problem can be solved and the polynomial coefficients a_0 and a_1 of the model function can be calculated:

$$a_1 = \frac{\sum_{\nu=1}^{N} (x_\nu - \overline{x})(y_\nu - \overline{y})}{\sum_{\nu=1}^{N} (x_\nu - \overline{x})^2}, \qquad a_0 = \overline{y} - a_1 \overline{x} \tag{B.4}$$

This approach is used to determine the calibration functions of the pressure sensors in the measurement system. All pressure transducers used in the G109b measurement system are designed with a linear dependency between pressure and output voltage. It has been shown that linearity of the pressure sensors is very good and calibration functions with higher degree polynomials don't lead to significantly lower sums of squared residuals and calibration errors [89]. Therefore, linear calibration functions are used for all pressure sensors and almost all other sensors.

After a calibration function has been determined using the procedure shown before, the quality of the calibration function must be examined. The difference between the model curve $g(x_\nu)$ and each data point y_ν is the absolute error F_ν for each calibration point

$$F_\nu = y_\nu - g(x_\nu). \tag{B.5}$$

The dimensionless relative error f_ν is the absolute error divided by the sensor range $y_{max} - y_{min}$

$$f_\nu = \frac{y_\nu - g(x_\nu)}{y_{max} - y_{min}}. \tag{B.6}$$

Hence, the maximum relative and absolute errors using the calibration function are:

$$f_{max} = \max |f_\nu| \qquad F_{max} = \max |F_\nu| \tag{B.7}$$

A better measure for the quality of the calibration function is the arithmetic average of the relative and absolute error.

$$\overline{f} = \frac{1}{N} \sum_{\nu=1}^{N} |f_\nu| \qquad \overline{F} = \frac{1}{N} \sum_{\nu=1}^{N} |F_\nu| \tag{B.8}$$

The average error is a good measure which error can be expected in reality whereas the maximum error is used to determine the maximum possible error, which is not very likely in practice.

B.1.2. Analog-to-Digital Converter Errors

Analog-to-Digital converters (ADC) are used to convert the analog sensor output signals into digital data, which is then processed and stored. Besides the number of input channels and the range of analog inputs, the resolution is a very important criterion for the choice of the AD converter. It indicates the number of discrete values the AD converter can produce over the range of analog values. The resolution is usually expressed in bits.

Resolution can also be defined electrically and expressed in volts. The minimum change in voltage required to guarantee a change in the output code level is called the least significant bit (LSB) voltage. The resolution Q of the AD converter is equal to the LSB voltage. The voltage resolution of an AD converter is equal to its overall voltage measurement range divided by the number of discrete voltage intervals:

$$Q = \frac{E_{FSR}}{N} \tag{B.9}$$

where N is the number intervals and E_{FSR} is the full scale voltage. The

Resolution bits	**Intervals** N	**Resolution** % FS
12	4096	$24.4 \cdot 10^{-3}$
14	16384	$6.1 \cdot 10^{-3}$
16	65536	$1.5 \cdot 10^{-3}$
18	262144	$0.4 \cdot 10^{-3}$

Table B.1.: Resolution of commercially available AD converters.

number of voltage intervals is usually given by

$$N = 2^M \tag{B.10}$$

where M is the AD converter's resolution in bits.

An ADC has several sources of errors. Quantization error and non-linearity are unavoidable in any AD converter.

The quantization error is the difference between the original signal and the digitized signal. Quantization error is due to the finite resolution of the digital representation of the signal. Consequently, the magnitude of the quantization error is linked to the resolution and its magnitude is between zero and half of one LSB.

Typical resolutions of commercially available AD converters are shown in Table B.1. Due to their low resolution 12 bit AD converters are outdated by the time of the definition of the measurement equipment used within this study. 14 bit can be considered as the low-cost end, 16 bit is typical and a few multi-channel AD converters are available with 18 bit at high cost. Higher resolutions are only available for a low number of measurement channels and therefore not feasible for this study. It is shown later that a resolution of 16 bits gives a good match with the resolution of the sensors. Additionally, it is the most common resolution by the time of this study which is a good compromise between performance and cost and therefore chosen.

An assessment of the performance of the AD converters is beyond the technical possibilities available for this study. Therefore the highest possible error given in the manufacturers specifications is assumed. Table B.2 shows the specifications for the *NI USB-6259* AD converter, which is used to digitize the ambient air data system's analog sensor output signals. The total accuracy is lower than the resolution and also includes the non-linearity error and noise. The resolution is more a theoretical value and not given in the specifications.

ADC Specifications		
Manufacturer	National Instruments, Inc.	
Model	NI USB-6259 Screw Term	
Number of analog inputs	32SE/16DI	
Input-Ranges	±10V,±5V,±2V,±1V,±0.5V,±0.2V,±0.1V	
ADC Resolution	16 bits	
ADC Performance		
Accuracy		
Nominal range	Random noise $\sigma(\mu Vrms)$	Sensitivity (μV)
±10V	280	112.0
±5V	140	56.0
±2V	57	22.8
±1V	32	12.8
±0.5V	21	8.4
±0.2V	16	6.4
±0.1V	15	6.0
Timing Resolution	50ns	
Sampling Rate		
Single channel	1.25MS/s	
Multi-channel	1.00MS/s aggregate	

Table B.2.: NI USB-6259 AD converter specifications from factory data sheet [99].

The specifications of the *NI 9205* AD converter is shown in Table B.3. Four of these AD converters are used, one for the hotwire signals, one for the unsteady pressure sensors and the remaining converters for the microphone sensors.

In order to calculate the absolute noise uncertainty (in microvolts) $\Delta\mu V$ the standard deviation σ of the random noise is taken from the manufacturer's specifications. According to the specifications the expected bounded interval for random noise is 3σ. Hence, the AD converters noise uncertainty is

$$\Delta\mu V_{noise} = \frac{3\sigma(\mu Vrms)}{\sqrt{n}} \tag{B.11}$$

where n is the number of samples. It is clearly visible that a higher

ADC Specifications		
Manufacturer	National Instruments, Inc.	
Model	NI 9205 for CRIO	
Number of analog inputs	32SE/16DI	
Input-Ranges	±10V,±5V,±1V,±0.2V	
ADC Resolution	16 bits	
ADC Performance		
Accuracy (combined errors)		
Nominal range	Random noise $\sigma(\mu Vrms)$	Sensitivity (μV)
±10V	240	96.0
±5V	116	46.4
±1V	26	10.4
±0.2V	10	4.0
Timing Resolution	50ns	
Sampling Rate	250kS/s aggregate	

Table B.3.: NI 9205 AD converter specifications from factory data sheet [100].

number of samples minimizes the noise uncertainty in the calibration. This is an important factor for the overall accuracy because the random noise level is higher than the sensitivity. For measurements a higher sampling rate than required is chosen in order to minimize noise by averaging measurement results.

B.1.3. Uncertainty in Calibration Standard

Another source of error is the observational error in the calibration instrument. It is the difference between a true physical value of the quantity used for the calibration and the value measured by the calibration device, which is used in the analysis. A high accuracy of the calibration standard is a requirement for accurate calibration functions.

For the calibration of pressure sensors, the *CPC 6000 Automated Pressure Calibrator* manufactured by *Mensor* is used to supply the pressures used as calibration standard. The supply of either absolute or relative pressure is possible. The absolute accuracy depends on the ranges of the internal pressure transducers. The uncertainty in the calibration standard for each sensor calibration therefore depends on the pressure

range used in the calibration process. A detailed description of the calibrator's performance can be found in the manufacturer's specifications [101]. The applicable uncertainty in the calibration standard is shown and included in the error analysis for each calibration.

For measurement parameters other than pressures, e.g. temperature and humidity, the calibration data from the manufacturers are used, which are delivered with the instrument.

B.1.4. Systematic Errors

Systematic errors can be found either in the sensor itself, e.g. thermal effects, or elsewhere in the measurement chain, e.g. pitot-static errors. Furthermore, it is important to distinguish temporal stable effects from time dependent effects like long term drift.

Systematic errors related to the sensor itself are covered together with the other sensor errors in Chapter B.2 whereas systematic errors from sources elsewhere in the measurement chain are shown in Chapter B.3.

B.2. Quantification of Sensor Errors

B.2.1. Ambient Air Data System

All measurement parameters from the ambient air data systems are calculated from four basic measurands, the static pressure p_{stat}, the dynamic pressure q, the temperature T and the humidity φ.

Static Pressure Sensor

The static pressure is measured with a *Setra Model 270* absolute pressure sensor. The measurement principle is that the applied pressure bends a membrane, whose movement changes the capacitance of a capacitor. The capacitance is converted by internal electronics into an output voltage which linearly changes with the applied pressure. An abstract of the sensor's specifications from the factory data sheet [102] is shown in Table B.4.

The pressure range from 600 to 1100 hPa covers pressure altitudes up to approximately 4000 meters. According to the manufacturers specifications the sensor's overall accuracy is in the order of $\pm 0.05\%\ FS$ excluding thermal effects. Errors due to thermal effects reduce the accuracy significantly, especially if the high temperature changes in the flight environment are considered. In order to avoid thermal errors, the

Sensor Specifications	
Manufacturer	Setra Systems, Inc.
Model	270 (with high precision option)
Type	Absolute pressure
Input-Range	600 to 1100 hPa
Principle	Variable capacitance sensor
Sensor Performance	
Accuracy (RSS)	±0.03% FS
Non-Linearity	±0.027% FS
Non-Repeatability	0.01% FS
Hysteresis	0.01% FS
Thermal Effects	
Zero shift	< ±0.18 %FS/50°
Span shift	< ±0.18 %FS/50°
Warm-up shift	< ±0.04 %FS
Resolution	infinite, limited by output noise level
Settling Time	<10 milliseconds
Electrical Data	
Output-Range	0 to 5 V
Output Noise	<200 microvolts RMS

Table B.4.: Static pressure sensor specifications from factory data sheet [102].

sensor is stored in the aircraft at constant temperature in a thermostatically controlled box. The power supply of the pressure sensors and the heating are separated from the rest of the measurement equipment to allow early warm-up (at least 30 minutes before any measurement) and enduring temperature control. This procedure to avoid systematic temperature errors is much simpler than calibration at different temperatures and also eliminates the warm-up shift error.

In the sensor calibration process the *CPC 6000 Automated Pressure Calibrator* is used to supply different absolute pressures, which are used as calibration standard. For the *CPC 6000's* pressure range used in this calibration the uncertainty in the calibration standard is $\pm 1.8 Pa$.

To uncover hysteresis errors in the sensor, calibration points are obtained in two calibration runs, one with ascending pressure, the other run with descending pressure. Each subsequent calibration point is obtained in the different calibration run. A hysteresis error would be visible in an

alternately changing sign for the calibration errors. Figure B.1 shows the calibration results, a hysteresis error cannot be seen in the calibration data. This was foreseeable from the specifications because the hysteresis error is smaller than the non-linearity and noise and therefore overlayed by these errors.

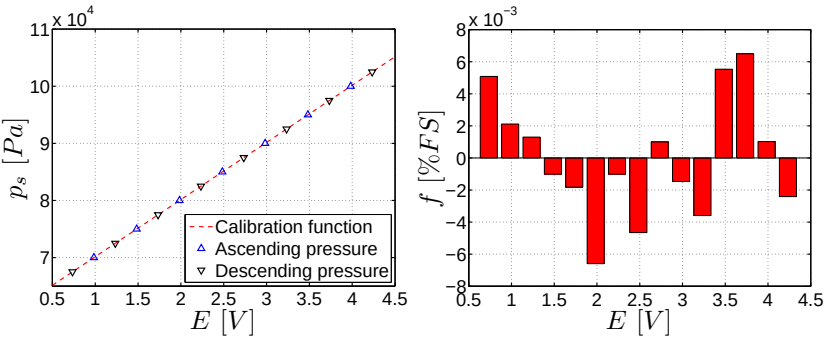

(a) Calibration data (b) Relative error

Figure B.1.: Calibration data of static pressure sensor and relative error compared to calibration function.

Calibration function			
$p_s[Pa] = 10005.22 \cdot E[V] + 60149.37$			
Calibration errors			
$\overline{F}$ $[Pa]$	$\overline{f}$ $[\%\ FS]$	F_{max} $[Pa]$	f_{max} $[\%\ FS]$
1.50	0.0030	3.25	0.0065

Table B.5.: Results of the static pressure sensor calibration.

The calibration function and errors are shown in Table B.5. It is clearly visible that the performance data in the manufacturer's specifications is very conservative and the real linearity is much better.

In the calibration process the output voltages from the pressure sensor are measured with the same AD converter, which is used in flight. Therefore, the AD converter errors like non-linearity and offset are covered within the calibration. 12000 data points are used to average each calibration point. Inserting the random noise for the AD converter's $\pm 5V$ range from Table B.2 into Equation B.11 the AD converter's abso-

lute noise uncertainty during the calibration process can be calculated:

$$\Delta\mu V_{noise} = \frac{3 \cdot 140\mu V}{\sqrt{12000}} = 3.8\mu V$$

The total AD converter uncertainty during calibration is the sum of noise uncertainty and sensitivity (from Table B.2):

$$\Delta\mu V_{ADC(cal)} = \Delta\mu V_{noise} + \Delta\mu V_{sensitivity} = 3.8\mu V + 56.0\mu V = 59.8\mu V$$

Inserting the AD converter's absolute uncertainty during calibration into the voltage dependent part of the calibration function from Table B.5, the absolute pressure uncertainty due to the AD converter is:

$$\Delta p_{ADC(cal)} = 10005.22\ [Pa/V]\ \cdot\ 59.8 \cdot 10^{-6}\ [V] = 0.6\ [Pa]$$

During the measurements the uncertainty due to the analog to digital conversion is present again. In this case the noise uncertainty is higher because only 10 samples can be used to average one data point. Using the same procedure as before, the pressure uncertainty due to the AD converter's uncertainty during measurements can be calculated:

$$\Delta p_{ADC(meas)} = 10005.22\ [Pa/V]\ \cdot\ 188.8 \cdot 10^{-6}\ [V] = 1.9\ [Pa]$$

For the calculation of the maximum error it is assumed that the contributions from all individual errors are to the same direction with their maximum value. Hence, all absolute error values are added to the total error:

$$\Delta F_{total} = |\Delta F_1| + |\Delta F_2| + ... + |\Delta F_n|\,. \tag{B.12}$$

This assumption is not very realistic since the individual errors cancel each other out partially. According to *Gauss* the expected error can be estimated as follows:

$$\Delta F_{total} = \sqrt{(\Delta F_1)^2 + (\Delta F_2)^2 + ... + (\Delta F_n)^2}. \tag{B.13}$$

The results of the error estimation for the static pressure sensor are shown in Table B.6:

If the average error of the calibration function is taken into account instead of the maximum error, the expected absolute error calculated using Eq. B.13 reduces from 4.22 Pa to 3.08 Pa.

Error	Value
Calibration function	± 3.25 $[Pa]$
Calibration standard	± 1.8 $[Pa]$
ADC uncertainty (calibration)	± 0.6 $[Pa]$
ADC uncertainty (measurement)	± 1.9 $[Pa]$
Expected absolute error (Eq. B.13)	4.22 $[Pa]$
Maximum absolute error (Eq. B.12)	7.55 $[Pa]$
Expected relative error (Eq. B.13)	0.00844 % FS
Maximum relative error (Eq. B.12)	0.0151 % FS

Table B.6.: Error estimation for the static pressure sensor.

Dynamic Pressure Sensor

The dynamic pressure is measured with a *Setra Model 239* differential pressure sensor. The basic measurement principle is the same as for the *Setra Model 270* absolute pressure sensor. The difference is that pressure to be measured is applied to one side of the membrane whereas the reference pressure is applied to the opposite side. An abstract of the sensor's specifications from the factory data sheet [103] is shown in Table B.7.

The input pressure range of 0 to 3800 Pa corresponds to a maximum indicated airspeed of 78.8 m/s (280 km/h) which is well beyond the airplane's never exceed speed. Model 239 pressure sensors with smaller input ranges do not cover the whole flight envelope and cannot be used.

The same calibration procedure as described before is used for the calibration of the dynamic pressure sensor. The sensor is stored in the same insulated and thermostatically controlled box as the static pressure sensor to avoid temperature errors.

The results of the dynamic pressure sensor calibration are shown in Figure B.2 and Table B.8. In contrast to the calibration results for the static pressure sensor a hysteresis effect is visible in the calibration data (alternate sign of the errors with ascending and descending pressure). This hysteresis error is included in the calibration function error.

A different pressure range can be used in the calibration process using the *CPC 6000 Automated Pressure Calibrator*. The uncertainty in the calibration standard is reduced to $\pm 0.18 Pa$.

The output voltage is the same as for the static pressure sensor and the same AD converter is used. Hence, the uncertainty value calculated

Sensor Specifications	
Manufacturer	Setra Systems, Inc.
Model	239 (with high precision option)
Type	Differential pressure
Input-Range	0 to 3800 Pa
Principle	Variable capacitance sensor
Sensor Performance	
Accuracy (RSS)	±0.073% FS
Non-Linearity	±0.05% FS
Non-Repeatability	0.02% FS
Hysteresis	0.05% FS
Thermal Effects	
Zero shift	< ±0.45 %FS/50°
Span shift	< ±0.45 %FS/50°
Warm-up shift	< ±0.1 %FS
Resolution	infinite, limited by output noise level
Settling Time	<100 milliseconds
Electrical Data	
Output-Range	0 to 5 V
Output Noise	<200 microvolts RMS

Table B.7.: Dynamic pressure sensor specifications from factory data sheet [103].

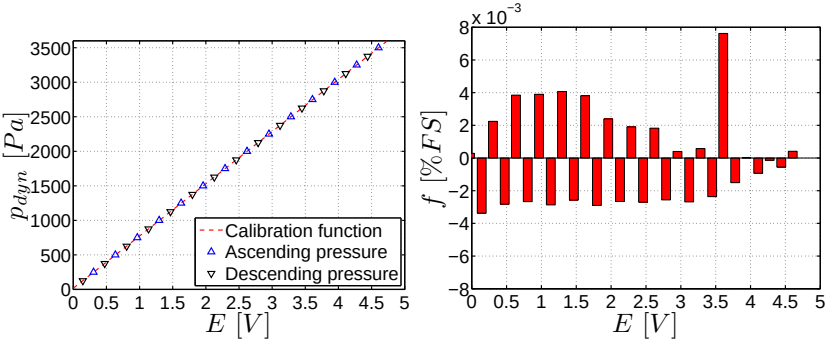

(a) Calibration data

(b) Relative error

Figure B.2.: Calibration data of dynamic pressure sensor and relative error compared to calibration function.

Calibration function			
$q[Pa] = 756.0657 \cdot E[V] + 17.9623$			
Calibration errors			
$\overline{F}$ $[Pa]$	$\overline{f}$ $[\%\ FS]$	F_{max} $[Pa]$	f_{max} $[\%\ FS]$
1.15	0.0303	3.81	0.1003

Table B.8.: Results of the dynamic pressure sensor calibration.

before can be used.

The results of the error estimation for the dynamic pressure sensor are shown in Table B.9:

Error	**Value**
Calibration function	± 3.81 $[Pa]$
Calibration standard	± 0.18 $[Pa]$
ADC uncertainty (calibration)	± 0.6 $[Pa]$
ADC uncertainty (measurement)	± 1.9 $[Pa]$
Expected absolute error (Eq. B.13)	4.30 $[Pa]$
Maximum absolute error (Eq. B.12)	6.49 $[Pa]$
Expected relative error (Eq. B.13)	0.113 % FS
Maximum relative error (Eq. B.12)	0.171 % FS

Table B.9.: Error estimation for the dynamic pressure sensor.

If the average error of the calibration function is taken into account instead of the maximum error, the expected absolute error calculated using Eq. B.13 reduces from 4.30 to 2.31 Pa.

Temperature Sensor

For temperature measurements a *PT 1000* resistance thermometer is used. The measurement principle of this temperature sensor is the predictable change in electrical resistance of platinum (Pt) with the temperature. A digital measuring transducer is used to transform the electrical resistance input into a voltage output (0 to 10 V). The digital measuring transducer is factory calibrated using the *PT 1000* resistance characteristics according to DIN/IEC 60751. The measurement range is from $-30°C$ to $70°C$. The accuracy of the whole system is given with

$\pm 0.15\%FS$. The calibration function is:

$$T\ [K] = 10 \cdot E\ [V] + 243.15$$

Together with the AD converters uncertainties (including AD converter non-linearity) in the order of $\pm 0.05\%FS$, the temperature uncertainty is in the order of $\pm 0.2°C$.

In order to avoid measurement errors due to heating from solar radiation, the temperature sensor is positioned within a duct on the ambient air data boom on the left wing, see Figure 4.12.

Humidity Sensor

The humidity sensor is a capacitive humidity sensors manufactured by *Hygrosens*. It measures relative humidity and meets high accuracy requirements in a wide temperature range. The sensor elements are robust, long term stable and dew resistant. The accuracy is given by the manufacturer with $\pm 3\%rH$. The calibration functions is:

$$\varphi\ [-] = 0.2 \cdot E\ [V]$$

B.2.2. Multi-channel Pressure Measurements

ESP 64 Channel Miniature Pressure Transducer

The *ESP-64HD DTC* is a 64 channel miniature pressure transducer for wind tunnel pressure measurements from *Pressure Systems*. It is used in conjunction with the *CANdaq* pressure scanner acquisition system from *Chell Instruments* which supplies the pressure scanner with a constant operation voltage, converts and corrects the scanner's analog output data into digital data and delivers the digital data via a Local Aera Network connection. The system is used either for the steady airfoil pressure distribution measurements or for the wake rake measurements. The specifications are shown in Table B.10.

The scanner has the "DTC" option, which means Digital Temperature Correction. This option is valuable for in-flight measurements because it greatly reduces thermal errors. The total relative accuracy given in the manufacturer's data sheet including thermal errors is $\pm 0.06\%\ FS$. For the given pressure range this translates into an absolute accuracy of ± 10.2 Pa.

Sensor calibrations from various wind tunnel campaigns show a higher accuracy than specified with a very good long-term stability in the order

Sensor Specifications	
Manufacturer	Pressure Systems, Inc.
Model	ESP-64HD DTC
Type	Differential pressure
Input-Range	±2.5 PSI (±17 kPa)
Principle	Silicone piezoresitive sensors
Sensor Performance	
Accuracy (RSS)	±0.03% FS
Thermal Effects	
Zero shift	N/A
Span shift	N/A
Total thermal stability	$< \pm 0.002$ %FS
Pressure Scanner Acquisition System	
Manufacturer	Chell Instruments Ltd
Model	CANdaq
Accuracy (DAQ+Scanner)	±0.06% FS
Resolution	14 bit
Sampling rate	312 Hz per channel (@64 ch.)

Table B.10.: Dynamic pressure sensor specifications from factory data sheet.

Sensor Specifications		
Manufacturer	Sensortechnics GmbH	
Model	HCL12X5P	
Type	Differential pressure	
Input-Range	±1250 Pa	
Principle	Piezoresistive sensor	
Sensor Performance		
	Nom.	**Max.**
Zero pressure offset		±0.5mV
Zero pressure offset	20.0mV	21.0mV
Non-Linearity and hysteresis	±0.05% FS	±0.25% FS
Thermal Effects (0 to 50°C)		
Zero shift		< ±0.15mV
Span shift		< ±0.20mV
Warm-up shift		< ±0.05mV
Settling Time	<1 millisecond	
Electrical Data		
Output-Range	0 to 20 mV	

Table B.11.: Dynamic pressure sensor specifications from factory data sheet.

of $\pm 8Pa$ for the least accurate sensor. Due to complicated calibration procedure and time constraints, the sensor has not been re-calibrated in the context of the present study. Therefore, the $\pm 8Pa$ accuracy discovered in other calibrations is considered as the sensor's real accuracy and used to calculate expected errors whereas the specified accuracy is used to calculate the maximum errors.

HCL12X5 "Low-cost" Miniature Pressure Transducers

For the unsteady measurements of the airfoil pressure distribution 32 *HCL12X5P* pressure transducers from *Sensortechnics* are used. An abstract of the sensor's specifications from the manufacturer's data sheet is shown in Table B.11. The nominal accuracy of this "low cost" sensor is not much worse compared to the high-end wind tunnel pressure transducer but the tolerances in the specifications are much wider. Hence, the accuracy can be much lower if no custom calibration is performed. The real accuracy was investigated for all sensors by doing a custom

Calibration function				
Sensor 05	$\Delta p[Pa] = 254.6833 \cdot E[V] - 0.2285$			
Sensor 32	$\Delta p[Pa] = 256.3987 \cdot E[V] + 27.2265$			
Calibration errors				
	$\overline{F}$ $[Pa]$	$\overline{f}$ $[\%\ FS]$	F_{max} $[Pa]$	f_{max} $[\%\ FS]$
Sensor 05	1.28	0.0513	2.36	0.0943
Sensor 32	1.15	0.0303	2.94	0.1175

Table B.12.: Exemplary results of the unsteady pressure sensor calibration.

calibration for each sensor.

The sensor's maximum full-scale output voltage of 0.02 V is amplified to 10 V using custom built amplifiers. The amplification of each amplifier is slightly different. To avoid errors in the calibration process it was made use of the same measurement chain (sensor, amplifier and AD converter) used in flight.

The AD converter is a *NI 9205*, the specifications are shown in Table B.3. The AC converter is operated in a *NI cRIO 9074* chassis [104]. Again, 12000 samples for each data point are used for averaging in the calibration process and 10 samples for averaging during pressure measurements. For the *NI 9205* AD converter and the range of $\pm 10\ V$ the AD converter accuracy for calibration and measurements are:

$$\Delta\mu V_{ADC(cal)} = \Delta\mu V_{noise} + \Delta\mu V_{sensitivity} = 6.6\mu V + 96.0\mu V = 102.2\mu V$$

$$\Delta\mu V_{ADC(meas)} = 227.7\mu V + 96.0\mu V = 323.7\mu V$$

The calibration procedure and uncertainty in the calibration standard using the *CPC 6000 Automated Pressure Calibrator* is same as for the dynamic pressure sensor. All sensors are calibrated, exemplary results for Sensors 5 and 32 are shown in Table B.12.

Table B.13 shows the exemplary error estimation for the unsteady pressure sensors. AC converter uncertainties are calculated using the specifications of the *NI 9205* ADC. Additionally, errors due to thermal effects have to be included because the sensors are not stored in a constant temperature environment.

Although the relative errors are higher compared to the *ESP-64HD DTC* multi-channel measurement system, the absolute error of the low-cost pressure transducers is only in the order of one third. This is a result

Error	Sensor 5	Sensor 32
Calibration standard	± 0.18 $[Pa]$	
Calibration function	± 2.36 $[Pa]$	± 2.94 $[Pa]$
ADC uncertainty (calibration)	± 0.03 $[Pa]$	± 0.03 $[Pa]$
ADC uncertainty (measurement)	± 0.08 $[Pa]$	± 0.08 $[Pa]$
Thermal effects (zero shift)	± 0.04 $[Pa]$	± 0.04 $[Pa]$
Thermal effects (span shift)	± 0.05 $[Pa]$	± 0.05 $[Pa]$
Expected absolute error (Eq. B.13)	2.37 $[Pa]$	2.95 $[Pa]$
Maximum absolute error (Eq. B.12)	2.74 $[Pa]$	3.32 $[Pa]$
Expected relative error (Eq. B.13)	0.095 % FS	0.118 % FS
Maximum relative error (Eq. B.12)	0.110 % FS	0.133 % FS

Table B.13.: Error estimation for the unsteady pressure sensors.

of the more suitable pressure range of the *HCL12X5P* transducers.

Assuming the average instead of the maximum calibration error for the calculation of the expected absolute error, the absolute error reduces in the exemplary cases to 1.30 respectively 1.17 Pa.

B.2.3. Angle of Attack Measurements

Flightlog

The fast and accurate measurement of the angle of attack is critical for this project. AoA measurements are needed to validate the performance loss theories involving lift. A brief description of the chosen two-part system has been given in Chapter 5.4.

A *Dornier FlightLog*, which is a two-directional wind vane, delivers a long-term stable AoA and sideslip reference for steady flight conditions. It is mounted to a boom on the left wing, see Figure 4.12. The accuracy of the *FlightLog* has been thoroughly investigated by means of wind-tunnel tests in previous projects. Whereas the manufacturer's specifications [105] indicate an accuracy of $\pm 0.2°$, Hardt [72] proved an accuracy of below $\pm 0.1°$ including the subsequent errors in the measurement chain (AD converter). The resulting calibration functions are:

$$\alpha\ [°] = 13.404 \cdot E\ [V] - 32.864$$

$$\beta\ [°] = 13.167 \cdot E\ [V] - 32.857$$

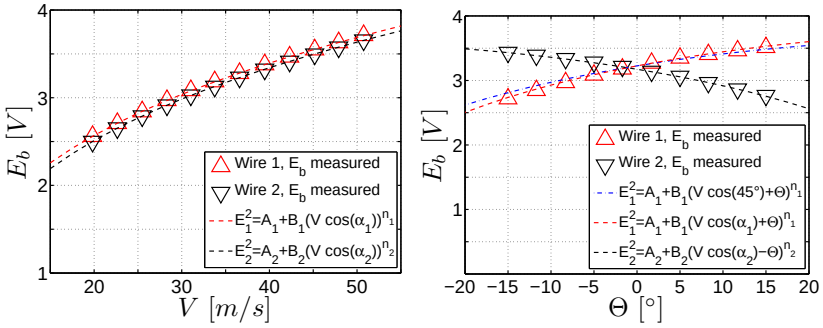

(a) Velocity calibration at $\Theta = 0°$ (b) Angle calibration at V=35m/s

Figure B.3.: Hotwire calibration using the effective velocity concept, results for "Probe 1".

The accuracy is limited by the resolution of the potentiometers sensing the movements of the vane and not by the aerodynamics of the vane [105]. The AD converter uncertainty of $\pm 0.0025°$ can be neglected.

An AoA measurement based on the measurement of the pressure difference between two discrete points on the wing (one point on the upper side, one point on the lower side) has been investigated by Hardt [72] and was used in the measurements by Erb [71]. Although the system has a reported accuracy about ten times higher compered to the *FlightLog* [71], it was not implemented in the actual measurement system due to time constraints.

Hotwires - Ground Calibration

X-shaped *Dantec 55P61* hotwires probes mounted on booms at the glove are used to measure AoA and velocity with a high temporal resolution (6000 Hz sampling frequency). The basic equations and calibration concepts for hotwire probes operated in constant temperature mode (CTA) have been shown in Chapter 5.1.2.

All hotwire probes were calibrated using the TU Darmstadt *Eiffel* type low-speed calibration wind tunnel or a custom built calibration device, see also [73].

The velocity and angle calibration results for an exemplary probe ("Probe 1") are shown in Figure B.3. The resulting calibration coefficients for "Probe 1" are given in Table B.14.

Calibration constant	Wire 1	Wire 2
A	-2.8171	-3.3994
B	1.9905	2.0543
n	0.6062	0.5861
α_i	49.5 [°]	-45 [°]

Table B.14.: Calibration factors for *Dantec 55P61* hotwires probe "Probe 1".

The calibration errors for "Probe 1" are shown in Figure B.4. Due to manufacturing inaccuracies the orientation of wire 1 is not exactly 45° relative to the probe axis. A significant decrease in angle calibration error is achieved if this deviation from the ideal shape of $\alpha = 45°$ is taken into account.

Again, the same measurement chain is used for calibration as well as for the in-flight measurements. Therefore, the gain and offset error of the AD converter is avoided. 60000 samples for each data point are used for averaging in the calibration process. No averaging is used for the measurements due to the high sampling frequency requirements. For the *NI 9205* AD converter and the range of $\pm 5\ V$ the AD converter accuracy for calibration and measurements are:

$$\Delta\mu V_{ADC(cal)} = \Delta\mu V_{noise} + \Delta\mu V_{sensitivity} = 1.4\mu V + 46.4\mu V = 47.8\mu V$$

$$\Delta\mu V_{ADC(meas)} = 348.0\mu V + 46.4\mu V = 394.4\mu V$$

These noise values are inserted into the calibration function. The results are shown in Table B.15. It is clearly visible that the AD converter uncertainty during calibration has a negligible effect on the absolute error. Also the ADC uncertainty during the measurement is one order below the uncertainty in the calibration function which dominates the absolute error.

Hotwires - In-flight Velocity Correction

King's law relates the voltage at the measuring bridge E_b to the flow velocity U and has been shown as Equation 5.9. It is repeated as Equation B.14.

$$E_b^2 = A + B\ U^n \tag{B.14}$$

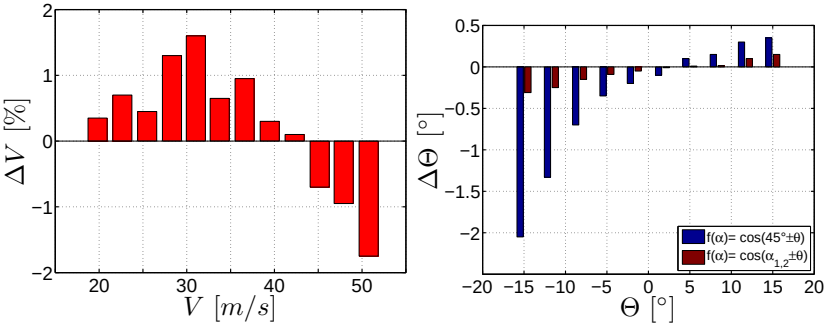

(a) Velocity calibration error at $\Theta = 0°$ (b) Angle calibration error at V=35m/s

Figure B.4.: Calibration function errors at constant ambient conditions.

Error	**Velocity**	**Angle**
Calibration standard	$\pm 0.05\ [m/s]$	$\pm 0.01\ [°]$
Calibration function	$\pm 0.85\ [m/s]$	$\pm 0.3\ [°]$
ADC uncertainty (calibration)	$\pm 0.001\ [m/s]$	$\pm 0.002\ [°]$
ADC uncertainty (measurement)	$\pm 0.01\ [m/s]$	$\pm 0.018\ [°]$

Table B.15.: Error estimation for the hotwire probe under constant ambient conditions.

A different representation of *King's law* is

$$Nu = A_0 + B_0\ Re_{\mathrm{w}}^{n} \tag{B.15}$$

with the Nusselt number Nu and the local Reynolds number at the hotwire Re_d based on the wire diameter d.

$$Re_d = \frac{dU\rho}{\eta} \tag{B.16}$$

Using the definitions of some thermodynamic base numbers, the voltage at the measurement bridge can be expressed as follows:

$$E_b^2 = \left[A_0 + B_0 \left(\frac{dU\rho}{\eta}\right)^n\right] \pi l_w R_w \lambda_{fl} \left(T_w - T_{fl}\right). \tag{B.17}$$

As stated before, the relation between bridge voltage and flow velocity also depends on the ambient flow conditions like temperature, density and viscosity. Hence, the dimensional calibration coefficients from Equation B.14 also have a dependance on the ambient flow conditions. They are

$$A = A_0 \cdot \pi l_w R_w \lambda_{fl} \left(T_w - T_{fl}\right) \tag{B.18}$$

and

$$B = B_0 \cdot \pi l_w R_w \lambda_{fl} \left(T_w - T_{fl}\right) \cdot \left(\frac{d\varrho}{\eta}\right)^n . \tag{B.19}$$

It has been shown by Bruun [91] that a mathematical correction for different ambient flow conditions is only valid if the flow conditions during the measurement (temperature, density, viscosity) do not differ significantly from the calibration flow conditions. This condition is not true for in-flight measurements. A calibration on the ground at typical ambient flight conditions is not possible using the equipment available for this study. Therefore, a different approach has been taken.

A linear correction factor K_V has been proposed by Bruun [91] and was investigated by Arnold [73], see Equation 5.16.

$$\tilde{V}_{\text{cor}} = \tilde{V}_m \cdot K_V \tag{B.20}$$

Using the linear correction factor K_V is not mathematically correct since the calibration coefficient B (Equation B.19) in *King's law* has an additional term compared to the calibration coefficient A (Equation B.18). However, inserting the air density and viscosity values from the Standard Atmosphere for the flight regime during the measurements and using typical calibration coefficients n (in the order of 0.3 to 0.4), the last term in Equation B.19 (density and viscosity dependency) is a factor in the order of one. Therefore, the simplification of using a linear correction factor is justified. Since the correction factor K_V is temperature and altitude dependent, this factor can only be assumed to be constant for a short measurement interval.

The effective velocity calibration concept, see Bruun [91], is used for the in-flight measurements. The measured bridge voltages from the perpendicular oriented wires are converted into effective velocities using the calibration factors from the ground calibration and than decomposed into the flow velocity and the mean flow angle. Both hotwires are operated at the same wire temperature in the same ambient flow conditions, therefore the linear correction factor K_V is equal for both wires. There-

fore, only the flow velocity has to be corrected for the ambient conditions, the angle measurement is not affected. Linear correction factors of up to 20% were required for high-altitude measurements.

The following re-calibration procedure is applied to all hotwire measurements:

1. Calculation of the average flow velocity from the ambient air data system for the measurement interval.

2. Calculation of the average flow velocity from the hotwire measurement system with the ground calibration factors for the measurement interval.

3. Calculation of the linear correction factor K_V to match both average velocities.

4. Re-calibration of the hotwire velocity data.

5. Correction of the measured hotwire AoA for the systematic flow field error.

6. Health monitoring of the hotwire AoA measurements through comparison with the FlightLog AoA measurement.

Consequently, the measurement uncertainties in the in-flight hotwire velocity measurements are the sum of the the uncertainties in the ground calibration and the uncertainty in the true airspeed calculated from the ambient air data system. The uncertainty in the angle of attack measurement is the sum of ground calibration uncertainty and the calibration error in the correction of the systematic flow field error.

B.3. Quantification of Systematic Instrument Errors

B.3.1. Pitot-Static Errors

Besides the random and systematic sensor errors, which were investigated previously, the static pressure measurement is subject to another systematic error. The probe influences the flow field which leads to an erroneous pressure measurement, see also Nitsche and Brunn [70]. Hence, this systematic error influences the static pressure measurement itself and the measurement of the dynamic pressure since the static pressure

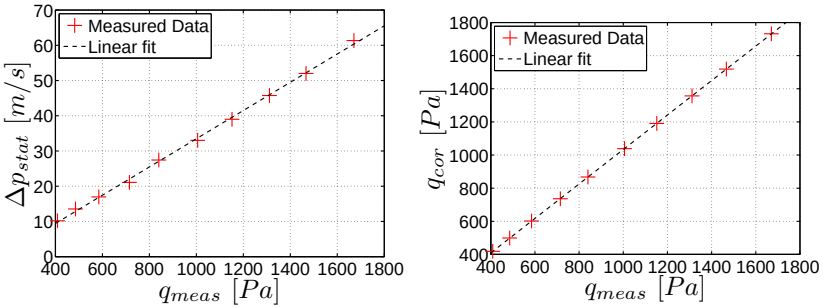

(a) Static pressure correction

(b) Dynamic pressure correction

Figure B.5.: Calibration functions for static and dynamic pressure measurements.

is the reference pressure. The in-flight calibration procedure to determine a correction function for this error has been described in Chapter 5.4.1.

Figure B.5 shows the results of the in-flight calibration. The measured static pressure is higher than the real static pressure, which means that the measured dynamic pressure is to low. The correction functions are:

$$p_{stat,cor}\ [Pa] = p_{stat,meas}\ [Pa] - 0.0401 \cdot q_{meas}\ [Pa] + 6.5907\ [Pa]$$

$$q_{cor}\ [Pa] = 1.0401 \cdot q_{meas}\ [Pa] - 6.5907\ [Pa]$$

Herein $p_{stat,meas}$ and q_{meas} are the measurement values after applying the sensor calibration procedure as described in Chapter B.2 with the calibration functions given in there.

B.3.2. AoA Errors in Flow Field

An in-flight calibration procedure as described in Chapter 5.4.2 is used to eliminate the systematical flow field error in the angle of attack measurement. The measured angle of attack α_{vane} can either be corrected to the geometrical angle of attack α_{geo} (global aircraft reference) or the AoA representing the local, two-dimensional flow case for the glove airfoil $\alpha_{2D,glove}$. The different AoA definitions are described in Appendix A.

Figure 5.9(b) shows the correlation between α_{vane} and α_{geo} for the

FlightLog whereas Figure 5.9(c) shows the correlation between α_{vane} and $\alpha_{2D,glove}$ for the *FlightLog* and the hotwire.

The correlation between α_{vane} and α_{geo} is only used for the comparison with the results of the numerical flow field simulations. In this case, the calibration function for the *FlightLog* is:

$$\alpha_{geo}\ [^\circ] = 0.7455 \cdot \alpha_{FL}\ [^\circ] - 1.809\ [^\circ]$$

For all Chapters 5.5 and 6, the angle of attack α is the abbreviation for $\alpha_{2D,glove}$.

$$\alpha_{2D,glove}\ [^\circ] = 0.7263 \cdot \alpha_{FL}\ [^\circ] - 0.7401\ [^\circ]$$
$$\alpha_{2D,glove}\ [^\circ] = 0.4883 \cdot \alpha_{HW}\ [^\circ] - 0.3116\ [^\circ]$$

B.4. Propagation of Uncertainty

Many required measurement quantities cannot be measured directly. They have to be calculated indirectly from measurement quantities which can be measured directly. This can be expressed mathematically

$$G = f(x_1, x_2, x_3, ...) \tag{B.21}$$

where G is the calculated measurement quantitiy and x_i are the directly measured quantities. The measurement uncertainties from all measurements Δx_i propagate into the calculated quantity, which has a resulting uncertainty ΔG.

The influence of each measurement uncertainty on the overall uncertainty depends on the sensitivity of calculated quantity to the individual quantity $\frac{\partial G}{\partial x_i}$ and the uncertainty Δx_i.

For independent measurement quantities it is improbable that all measurement errors are present at the same time to their maximum extent and influencing the error in the same direction. According to *Gauss* it is more probable that the errors cancel each other out to a certain extent and the total uncertainty G can be calculated as follows:

$$\Delta G_{Gauss} = \sqrt{\left(\frac{\partial G}{\partial x_1} \cdot \Delta x_1\right)^2 + \left(\frac{\partial G}{\partial x_2} \cdot \Delta x_2\right)^2 + \left(\frac{\partial G}{\partial x_3} \cdot \Delta x_3\right)^2 + ...} \tag{B.22}$$

However, the maximum uncertainty ΔG_{max} is the sum of all individual uncertainties for the improbable case that all errors add up in the same direction and to their maximum extent:

$$\Delta G_{max} = \left|\frac{\partial G}{\partial x_1}\right| \cdot \Delta x_1 + \left|\frac{\partial G}{\partial x_2}\right| \cdot \Delta x_2 + \left|\frac{\partial G}{\partial x_3}\right| \cdot \Delta x_3 + ... \tag{B.23}$$

This distinction into a typical (gaussian) uncertainty and a maximum uncertainty is comparable to the calculation of the instrument errors, where also a typical error (Eq. B.13) and a maximum error (Eq. B.12) was calculated. Therefore, the typical instrument errors are used to calculate the gaussian uncertainty whereas the maximum instrument errors are used to calculate the maximum uncertainty of the calculated measurement parameters in the following.

Many uncertainties change with the ambient conditions. Consequently, the uncertainties are calculated for exemplary altitudes assuming ISA conditions and the minimum and maximum airspeed of the G109b where applicable. If the measurement uncertainty for an individual measurement parameter is not altitude dependant, only one column is used for all exemplary altitudes.

Density

The air density is an important parameter, which is required for the calculation of several other quantities. The density ($\rho = m/V$) is calculated using the ideal gas law

$$\rho = \frac{p}{RT} \tag{B.24}$$

with the ambient pressure p, the gas constant R and the temperature T. The sensitivities of ρ are:

$$\frac{\partial \rho}{\partial p} = \frac{1}{RT} \tag{B.25}$$

$$\frac{\partial \rho}{\partial R} = \frac{-p}{R^2 T} \tag{B.26}$$

$$\frac{\partial \rho}{\partial R} = \frac{-p}{RT^2} \tag{B.27}$$

The gas constant R of humid air (as found in the atmosphere) changes with the relative humidity because humid air is a mixture of dry air and

R (dry air)	278.05 $[J/kgK]$		
R (water vapor)	461.6 $[J/kgK]$		
	R_{hum} $[J/kgK]$		
Relative Humidity $[-]$	H=0m	H=1500m	H=3000m
0.3	287.60	287.70	287.83
0.3	288.15	288.35	288.62
0.9	288.71	289.00	289.41
	ΔR $[J/kgK]$		
ΔRH $[-]$	H=0m	H=1500m	H=3000m
3%	0.055	0.065	0.078

Table B.16.: Gas constant for humid air and error due to relative humidity uncertainty.

water vapor. The influence of a changing gas constant on the density is shown in Equation B.26.

The gas constants for dry air and water vapor as well as the gas constants for humid air at certain relative humidities and altitudes (assuming ISA temperature) are shown in Table B.16. This table also includes the uncertainty in the calculation of the gas constant ΔR due to the measurement uncertainty of the relative humidity sensor.

Including the uncertainty in the gas constant, the gaussian and maximum uncertainty the calculated air density are calculated as follows:

$$\Delta\rho_{Gauss} = \sqrt{\left(\frac{1}{RT}\cdot\Delta p\right)^2 + \left(\frac{-p}{R^2T}\cdot\Delta R\right)^2 + \left(\frac{-p}{RT^2}\cdot\Delta T\right)^2} \quad \text{(B.28)}$$

$$\Delta\rho_{max} = \left|\frac{1}{RT}\right|\cdot\Delta p + \left|\frac{-p}{R^2T}\right|\cdot\Delta R + \left|\frac{-p}{RT^2}\right|\cdot\Delta T \quad \text{(B.29)}$$

The results for the density uncertainty are shown in Table B.17. The uncertainty in density is altitude dependent because the uncertainty in the gas constant R is altitude dependent.

Velocity

The dynamic pressure q is the product of the air density times 0.5 and the velocity squared. The velocity is calculated from the measured dynamic

Individual Sensor/Measurement Uncertainties			
Altitude	H=0m	H=1500m	H=3000m
$\Delta p_{Gauss}\ [Pa]$	4.22		
$\Delta p_{max}\ [Pa]$	7.55		
$\Delta R\ [J/kgK]$	0.055	0.065	0.078
$\Delta T\ [K]$	0.2		
Total Density Uncertainty			
Altitude	H=0m	H=1500m	H=3000m
$\Delta\rho_{Gauss}\ [kg/m^3]$	$8.83 \cdot 10^{-4}$	$8.14 \cdot 10^{-4}$	$7.37 \cdot 10^{-4}$
$\Delta\rho_{max}\ [kg/m^3]$	$11.76 \cdot 10^{-4}$	$11.14 \cdot 10^{-4}$	$10.40 \cdot 10^{-4}$
$\left(\frac{\Delta\rho}{\rho}\right)_{Gauss}$ [%]	0.0721	0.0769	0.0810
$\left(\frac{\Delta\rho}{\rho}\right)_{max}$ [%]	0.0960	0.1052	0.1143

Table B.17.: Absolute and relative uncertainty in calculated density.

pressure and the air density.

$$V = \sqrt{\frac{2q}{\rho}} \tag{B.30}$$

The velocity measurement (with the pitot tube) is sensitive to errors in the dynamic pressure measurement and the calculated air density.

$$\frac{\partial V}{\partial q} = \frac{1}{\sqrt{2q\rho}} \tag{B.31}$$

$$\frac{\partial V}{\partial \rho} = -\sqrt{\frac{q}{2\rho^3}} \tag{B.32}$$

The true airspeed V_{TAS} is calculated using the actual air density and prone to an error in the density calculation.

$$\Delta V_{TAS,Gauss} = \sqrt{\left(\frac{1}{\sqrt{2q\rho}} \cdot \Delta q\right)^2 + \left(-\sqrt{\frac{q}{2\rho^3}} \cdot \Delta\rho\right)^2} \tag{B.33}$$

$$\Delta V_{TAS,max} = \left|\frac{1}{\sqrt{2q\rho}}\right| \cdot \Delta q + \left|-\sqrt{\frac{q}{2\rho^3}}\right| \cdot \Delta\rho \tag{B.34}$$

The calibrated airspeed V_{CAS} is calculated using the standard density

$\rho_0 = 1.225 kg/m^3$. Consequently, the error in the in dynamic pressure measurement is the only source of error.

$$\Delta V_{CAS} = \left| \frac{1}{\sqrt{2q\rho_0}} \right| \cdot \Delta q \tag{B.35}$$

The uncertainty in the velocity measurement is velocity dependent. The uncertainty is calculated for speeds of 25 m/s and 50 m/s. These velocities are theoretical values since a true airspeed of 25 m/s is below stall speed with the high wing loadings at high altitudes. The results are shown in Table B.18.

Altitude

Altitudes are always measured relative to a reference altitude H_{ref} with a reference pressure p_{ref} and assuming a constant temperature lapse rate in the tropopause β_{Trop}. All altitudes dH are *"pressure altitudes"* and referenced to ISA conditions at sea level. The use of pressure altitudes eliminates the influence of temperature, temperature lapse rate and ground pressure. However, the pressure altitude is not identical to the geopotential altitude in non ISA conditions.

Pressure altitude calculations are sensible to the correct measurement of the static pressure and the gas constant.

$$dH = H - H_{ref} = \frac{T_{ref}}{\beta_{Trop}} \left(\left(\frac{p}{p_{ref}} \right)^{-\left(\frac{\beta_{Trop} R}{g}\right)} - 1 \right) \tag{B.36}$$

$$\Delta dH_{Gauss} = \sqrt{\left(\frac{\partial dH}{\partial p} \cdot \Delta p \right)^2 + \left(\frac{\partial dH}{\partial R} \cdot \Delta R \right)^2} \tag{B.37}$$

$$\Delta dH_{max} = \left| \frac{\partial dH}{\partial p} \right| \cdot \Delta p + \left| \frac{\partial dH}{\partial R} \right| \cdot \Delta R \tag{B.38}$$

with

$$\frac{\partial dH}{\partial p} = -\frac{T_{ref} R}{g \; p_{ref} \left(\frac{p}{p_{ref}} \right)^{\frac{\beta_{Trop} R}{g}+1}} \tag{B.39}$$

Individual Sensor/Measurement Uncertainties			
Altitude	H=0m	H=1500m	H=3000m
$\Delta q_{Gauss}\ [Pa]$	4.3		
$\Delta q_{max}\ [Pa]$	6.49		
$\Delta \rho_{Gauss}\ [kg/m^3]$	$8.83 \cdot 10^{-4}$	$8.14 \cdot 10^{-4}$	$7.37 \cdot 10^{-4}$
$\Delta \rho_{max}\ [kg/m^3]$	$11.76 \cdot 10^{-4}$	$11.14 \cdot 10^{-4}$	$10.40 \cdot 10^{-4}$
Total V_{CAS} Uncertainty at V_{CAS} = 25 m/s			
Altitude	H=0m	H=1500m	H=3000m
$\Delta V_{Gauss}\ [m/s]$	0.1404		
$\Delta V_{max}\ [m/s]$	0.2119		
$\left(\frac{\Delta V}{V}\right)_{Gauss}\ [\%]$	0.5616		
$\left(\frac{\Delta V}{V}\right)_{max}\ [\%]$	0.8477		
Total V_{TAS} Uncertainty at V_{TAS} = 25 m/s			
Altitude	H=0m	H=1500m	H=3000m
$\Delta V_{Gauss}\ [m/s]$	0.1406	0.1628	0.1894
$\Delta V_{max}\ [m/s]$	0.2238	0.2584	0.2997
$\left(\frac{\Delta V}{V}\right)_{Gauss}\ [\%]$	0.5626	0.6512	0.7576
$\left(\frac{\Delta V}{V}\right)_{max}\ [\%]$	0.8953	1.0337	1.1990
Total V_{CAS} Uncertainty at V_{CAS} = 50 m/s			
Altitude	H=0m	H=1500m	H=3000m
$\Delta V_{Gauss}\ [m/s]$	0.0702		
$\Delta V_{max}\ [m/s]$	0.1060		
$\left(\frac{\Delta V}{V}\right)_{Gauss}\ [\%]$	0.1404		
$\left(\frac{\Delta V}{V}\right)_{max}\ [\%]$	0.2119		
Total V_{TAS} Uncertainty at V_{TAS} = 50 m/s			
Altitude	H=0m	H=1500m	H=3000m
$\Delta V_{Gauss}\ [m/s]$	0.0725	0.0835	0.0967
$\Delta V_{max}\ [m/s]$	0.1299	0.1489	0.1713
$\left(\frac{\Delta V}{V}\right)_{Gauss}\ [\%]$	0.1449	0.1670	0.1934
$\left(\frac{\Delta V}{V}\right)_{max}\ [\%]$	0.2598	0.2979	0.3426

Table B.18.: Uncertainty in velocity measurements at different altitudes and flight velocities.

$$\frac{\partial dH}{\partial R} = -\frac{T_{ref}\ log\left(\frac{p}{p_{ref}}\right)}{g\left(\frac{p}{p_{ref}}\right)^{\frac{\beta_{Trop}R}{g}}} \tag{B.40}$$

The total altitude uncertainty (pressure altitude) is shown in Table B.19. These uncertainties include only the sensor errors and assume that the systematic static measurement error is removed by the pitot-static calibration.

Individual Sensor/Measurement Uncertainties			
Altitude	H=0m	H=1500m	H=3000m
$\Delta p_{Gauss}\ [Pa]$	4.22		
$\Delta p_{max}\ [Pa]$	7.55		
$\Delta R\ [J/kgK]$	0.055	0.065	0.078
Total Altitude Uncertainty			
Altitude	H=0m	H=1500m	H=3000m
$\Delta dH_{Gauss}\ [m]$	0.35	0.51	0.94
$\Delta dH_{max}\ [m]$	0.63	1.04	1.68

Table B.19.: Uncertainty in the measurement of the pressure altitude varying with the altitude.

Unsteady Airfoil Lift Coefficient

The measurement of the unsteady airfoil lift coefficient is a fundamental part of this study. The lift coefficient is calculated from the pressure distribution measured with the unsteady differential pressure sensors neglecting the influence of viscous forces. Inserting Equation 5.18 into Equation 5.19 yields

$$c_l \approx \left(-\int_{LE}^{TE} (p_u \cos\theta)\, \mathrm{d}s_u + \int_{LE}^{TE} (p_l \cos\theta)\, \mathrm{d}s_l \right) \frac{1}{qc} \cos\alpha. \tag{B.41}$$

Sources of error are the measurement of the pressure distribution and the measurement of the dynamic pressure used to normalize the lift force.

The errors of the differential pressure sensors are in the order of $3Pa$, see Table B.13. It is expected that the sensor errors cancel each other out in reality because the lift coefficient is the integrated pressure distri-

Assumed Static Pressure Errors (HCL12X5P Sensor)			
Δp $[Pa]$ (all sensors pressure side)	+1	+2	+3
Δp $[Pa]$ (all sensors suction side)	-1	-2	-3
Lift Coefficient Error due to Static Pressure Error			
V_{CAS} $[m/s]$	Δc_l $[-]$		
25	$5.2 \cdot 10^{-3}$	$10.4 \cdot 10^{-3}$	$15.7 \cdot 10^{-3}$
35	$2.7 \cdot 10^{-3}$	$5.3 \cdot 10^{-3}$	$8.0 \cdot 10^{-3}$
50	$1.3 \cdot 10^{-3}$	$2.6 \cdot 10^{-3}$	$3.9 \cdot 10^{-3}$

Table B.20.: Estimation of the maximum lift coefficient error due to pressure distribution measurement errors using different worst case scenarios.

Dynamic Pressure Uncertainty			
V_{CAS} $[m/s]$	25	35	50
Δq_{Gauss} $[Pa]$	4.3		
Δq_{max} $[Pa]$	6.49		
Lift Coefficient Uncertainty			
V_{CAS} $[m/s]$	25	35	50
Δcl_{Gauss} $[-]$	$12.9 \cdot 10^{-3}$	$3.4 \cdot 10^{-3}$	$1.0 \cdot 10^{-3}$
Δcl_{max} $[-]$	$19.5 \cdot 10^{-3}$	$5.2 \cdot 10^{-3}$	$1.5 \cdot 10^{-3}$

Table B.21.: Uncertainty in lift coefficient calculations due to dynamic pressure uncertainty at different flight velocities.

bution around the airfoil. The maximum possible lift error occurs in the following worst case scenario. The maximum pressure error is added to all sensors on the pressure side and subtracted from all sensors on the suction side. The results for different assumed pressure sensor errors are shown in Table B.20. In slow flight, the maximum possible lift error due to static pressure errors is in the order of 1% of the lift coefficient.

Another error in the calculation of the lift coefficient is due to the error in dynamic pressure measurement, which is used to calculate the lift coefficient. Taking the dynamic pressure error and the lift coefficients for different velocities into account, the lift coefficient error due to dynamic pressure can be calculated. The results are shown in Table B.21. In slow flight, the maximum combined lift error due to static and dynamic pressure errors is in the order of 2% of the lift coefficient. Because the assumption for the lift error due to static pressure error is very

unrealistic, the real lift error is expected to be below 1% of the lift coefficient.

Drag Coefficient from Wake Rake Measurements

The drag coefficient is calculated from the momentum deficit in the wake of the airfoil, see Equations 5.20 and 5.21. Out of practical constraints the wake is measured close to the airfoil where the static pressure at the wake position is still influenced by the wing pressure field and not p_∞. Equation 5.22 is repeated here.

$$c_d = \frac{2}{c} \int_W \sqrt{\frac{p_t - p}{q_\infty}} \left(1 - \sqrt{\frac{p_t - p_\infty}{q_\infty}} \right) \mathrm{d}y. \tag{B.42}$$

The static pressure at the wake rake position cannot be measured with the given equipment. The *ESP-64HD DTC* differential pressure transducer is used in the wake rake measurements. The reference pressure is p_∞, hence the dynamic pressure $q = p_t - p_\infty$ is measured. The unknown difference between p and p_∞ leads to a measurement error, which cannot be quantified. However, through the measurement of the drag coefficient under non-turbulent and turbulent conditions, the influences of atmospheric turbulence can be investigated although there may be an offset in the absolute drag values.

In order to investigate the influence of the uncertainty of the pressure measurements with the *ESP-64HD DTC* pressure transducer, the following worst case scenario is calculated. In-flight wake rake measurements for different flight velocities are taken. The pressure corresponding to the maximum sensor error is added to all measurement values within the wake whereas it is subtracted from all measurement values outside the wake. Then, the drag coefficient is calculated again and compared to the original values. The mean value of all dynamic pressure measurements outside the wake is used as q_∞. The results are shown in Table B.22.

Significant drag coefficient errors can be seen in slow flight, where the dynamic pressure is low and the wake is wider compared to the higher flight velocities. It must be stated again that the worst case scenario with a pressure error moving with the wake is highly unlikely in practice. The averaging of the measurements outside the wake minimizes an error in q_∞. The spline through the dynamic pressure measurements within the wake used in the drag calculation in post processing minimizes the drag coefficient error additionally.

Assumed Dynamic Pressure Errors (ESP-64, 2.5 PSI)		
Δp (all sensors in wake)	+8 Pa	
Δp (all sensors outside wake)	-8 Pa	
Drag Coefficient Error due to Dynamic Pressure Error		
V_{CAS} $[m/s]$	$c_d \cdot 10^4$ $[-]$	$\Delta c_d \cdot 10^4$ $[-]$
25	100.6	-30.1
35	61.1	-9.6
50	87.8	-3.1

Table B.22.: Estimation of the maximum drag coefficient error due to pressure measurement errors in the wake using a worst case scenario.

Nevertheless, it must be concluded that the drag coefficient measurement is less accurate compared to the lift coefficient measurement and the absolute drag coefficient uncertainty cannot be calculated.

Curriculum vitae

Personal

Michael Weismüller

Born on June 23, 1977 in Limburg
German

Education

06/2005 - 11/2010	Ph.D. in Mechanical Engineering, Technische Universität Darmstadt, Germany
10/1997 - 03/2005	Studies in Mechanical Engineering, Technische Universität Darmstadt, Germany Degree: Dip.-Ing. Maschinenbau
1993 - 1996	Pestalozzischule in Idstein Degree: Allgemeine Hochschulreife
1987 - 1993	Taunusschule in Bad Camberg

Employment

06/2005 - 11/2010	Research Assistant Institute of Fluid Mechanics and Aerodynamics Technische Universität Darmstadt, Germany
03/2003 - 07/2003	Internship at Lancair Certified Aircraft, Bend, OR, USA
07/2000 - 01/2003	Student Research Assistant Institute of Fluid Mechanics and Aerodynamics Technische Universität Darmstadt, Germany
02/1999 - 04/1999	Internship at Eichelsdörfer Flugzeugbau, Bamberg, Germany

Darmstadt, 26. April 2011